Eerik Sikanen

# DYNAMIC ANALYSIS OF ROTATING SYSTEMS INCLUDING CONTACT AND THERMAL-INDUCED EFFECTS

Eerik Sikanen

# DYNAMIC ANALYSIS OF ROTATING SYSTEMS INCLUDING CONTACT AND THERMAL-INDUCED EFFECTS

Supervisors    Professor Jussi Sopanen
               LUT School of Energy Systems
               Lappeenranta University of Technology
               Finland

               D.Sc. (Tech.) Janne E. Heikkinen
               LUT School of Energy Systems
               Lappeenranta University of Technology
               Finland

Reviewers      Professor Reijo Kouhia
               Department of Civil Engineering
               Tampere University of Technology
               Finland

               Associate Professor Jani Romanoff
               Department of Mechanical Engineering
               Aalto University
               Finland

Opponents      Professor Reijo Kouhia
               Department of Civil Engineering
               Tampere University of Technology
               Finland

               D.Sc. (Tech.) Erkki Lantto
               Sulzer Pumps Finland Oy
               Finland

## Abstract

Rotor dynamics is a special field of structural dynamics focusing on the study and analysis of rotating structures. Practical applications for rotor dynamics are found in typical industrial rotating electrical machine design. High-speed technology introduced new challenges for mechanical design of rotating machines. In addition to structural strength analysis, vibration issues due to critical speeds (CSs) typically occur in rotating machinery, which is one of the main research topics in the field of rotor dynamics. Alongside vibrations, thermal loads as heat losses from electrical machines or from process cycle can contribute to the stress state of the rotating structure in a form of thermal stress.

In this doctoral dissertation, the use of three-dimensional (3D) solid finite element (FE) theory for modeling rotating structures in the field of rotor dynamics is studied. A brief history of the use of finite element method (FEM) in the field of rotor dynamics is provided. In comparison to the traditional beam element approach, the new phenomena that can be studied by the use of the solid finite element method are introduced and studied. Capability of modeling of complex rotors of high-speed motors with complex geometric properties accurately arises when using the 3D solid element modeling approach. Additional features such as body force; for example, centrifugal force, stress stiffening and thermal effects, can be included in the model of the rotating system. Custom contact modeling for the structural analysis of rotating structures is utilized, along with custom coupled field solution routines.

Keywords: rotor dynamics, finite element method, solid element, three-dimensional, contact modeling, thermal stress

## Tiivistelmä

Roottoridynamiikka on dynamiikan erikoisala, jossa tutkitaan ja analysoidaan
pyöriviä rakenteita. Roottoridynamiikan käytännön sovelluskohteena voidaan
mainita teollisuuden pyörivät sähkökoneet. Suurnopeustekniikka tuo uusia haas-
teita pyörivien koneiden mekaniikkasuunnittelulle. Rakenteiden jännitysanalyysin
lisäksi kriittisistä nopeuksista aiheutuvia värähtelyilmiöitä esiintyy tyypillisesti
pyörivissä rakenteissa. Värähtelyilmiöt muodostavatkin roottoridynamiikassa
yhden päätutkimuskohteen. Värähtelyn lisäksi lämpökuormat, johtuen joko
sähkökoneen tai prosessin lämpöhäviöistä, tuovat oman osuutensa rakenteen
jännityslaskentaan lämpöjännitysten muodossa.

Tässä väitöstyössä tutkitaan kolmiulotteisten tilavuuselementtien käyttöä roottori-
dynamiikassa osana elementtimenetelmällä tehtävää mallinnusta. Elementtimene-
telmän historia osana roottoridynamiikkaa on esitelty. Tilavuuselementtien käyttö
osana elementtimenetelmää tuo mukanaan uusia mallinnettavia ilmiöitä verrattuna
perinteiseen palkkielementtimenetelmään, joita esitellään ja tutkitaan tässä työssä.
Monimutkaisten geometristen muotojen tarkka mallintaminen suurnopeussäh-
kökoneiden roottoreissa tulee mahdolliseksi käyttämällä tilavuuselementtimene-
telmää. Muita ilmiöitä, joita tilavuuselementeillä voidaan parhaiten mallintaa,
on rakenteen sisäiset voimat, kuten keskipakoisvoima, jännitysjäykistyminen
sekä termiset ilmiöt, kuten lämpölaajeneminen. Tässä väitöstyössä käytetään
kustomoidun kontaktin mallintamisen lisäksi kustomoituja ratkaisurutiineja osana
rakenneanalyysiä.

Hakusanat: roottoridynamiikka, elementtimenetelmä, tilavuuselementti, kolmiu-
lotteinen, kontaktimallintaminen, lämpöjännitys

## Acknowledgements

*Eerik Sikanen*

SYMBOLS

| | |
|---|---|
| $\mathbf{0}$ | Zero matrix |
| $a$ | Lower integration limit |
| $\mathbf{A}$ | State space matrix |
| $\mathbf{A}_b$ | Bordered stiffness matrix |
| $b$ | Upper integration limit |
| $\boldsymbol{b}$ | Vector of non-homogeneous coefficients in Lagrangian multiplier method |
| $b_e$ | Basquin exponent or fatigue strength exponent |
| $\mathbf{B}$ | Strain matrix |
| $\mathbf{B}_d$ | Matrix of shape function derivatives |
| $\mathbf{B}_i$ | Strain matrix of $i$th node |
| $\mathbf{B}_\epsilon$ | Matrix containing the spatial derivatives of the element shape functions |
| $c$ | Specific heat capacity |
| $\mathbf{C}$ | Heat capacity matrix |
| $\mathbf{C}^e$ | Element heat capacity matrix |
| $\mathbf{C}_b$ | Bearing damping matrix |
| $\mathbf{C}_e$ | Elastic damping matrix |
| $\mathbf{C}_{\text{tot}}$ | Total damping matrix |
| $\dot{\boldsymbol{d}}_e$ | First time derivative of element displacement vector |
| $\dot{\boldsymbol{d}}_{e,i}$ | First time derivative of element displacement vector of node $i$ |
| $\boldsymbol{d}_e$ | Element displacement vector |
| $\boldsymbol{d}_i$ | Nodal displacement vector of node $i$ |
| $\mathbf{D}$ | Matrix of material constants |
| $\mathbf{D}_c$ | Conductivity matrix |
| $e_g$ | Constraint error |
| $E$ | Elastic modulus |
| $f_x$ | Force components in global $X$-direction |
| $f_y$ | Force components in global $Y$-direction |
| $f_z$ | Force components in global $Z$-direction |
| $\boldsymbol{f}_b^e$ | Element nodal body force vector |
| $\boldsymbol{f}_s^e$ | Element nodal surface force vector |
| $\boldsymbol{F}$ | Force vector |
| $\hat{\boldsymbol{F}}$ | Modified force vector |
| $\boldsymbol{F}_c'$ | Contact force vector in the cylindrical coordinate system |
| $\boldsymbol{F}_{c,\text{trial}}'$ | Trial contact force vector in the cylindrical coordinate system |
| $\boldsymbol{F}_b^e$ | Element body force vector |
| $\boldsymbol{F}_g^e$ | Element translational acceleration force vector |
| $\boldsymbol{F}_{\text{ext}}^e$ | Element total external force vector |
| $\boldsymbol{F}_p^e$ | Element pressure force vector |
| $\boldsymbol{F}_s^e$ | Element surface force vector |

| | |
|---|---|
| $\boldsymbol{F}^e_{\Delta T}$ | Element thermal expansion force vector |
| $\boldsymbol{F}^e_{\epsilon}$ | Element strain force vector |
| $\boldsymbol{F}^e_{\Omega}$ | Element centrifugal force vector |
| $\boldsymbol{F}_{\mathrm{brg}}$ | Bearing force vector |
| $\boldsymbol{F}_c$ | Contact force vector the Cartesian coordinate system |
| $\boldsymbol{F}_{c,\mathrm{trial}}$ | Trial contact force vector in the Cartesian coordinate system |
| $\boldsymbol{F}_{\mathrm{ext}}$ | External force vector |
| $\boldsymbol{F}_{\mathrm{tot}}$ | Total force vector |
| $\boldsymbol{F}_{\mathrm{tot,shaft}}$ | Total force vector of shaft body |
| $\boldsymbol{F}_{\mathrm{tot,sleeve}}$ | Total force vector of sleeve body |
| $\boldsymbol{F}_{\mathrm{UB}}$ | Unbalance force vector at constant rotational speed |
| $\boldsymbol{F}_{\alpha,\mathrm{UB}}$ | Unbalance force vector due to angular |
| $\boldsymbol{F}_{\Omega}$ | Centrifugal force vector |
| $g$ | Gap |
| $\boldsymbol{g}$ | Vector of non-homogeneous coefficients |
| $\boldsymbol{g}_a$ | Acceleration coefficient vector |
| $g_x$ | Acceleration coefficient in global $X$-direction |
| $g_y$ | Acceleration coefficient in global $Y$-direction |
| $g_z$ | Acceleration coefficient in global $Z$-direction |
| $\mathbf{G}$ | Gyroscopic damping matrix |
| $\mathbf{G}^e$ | Element gyroscopic damping matrix |
| $h$ | Convection coefficient |
| $i$ | $i$th |
| $i_u$ | Imaginary unit |
| $I$ | Integral |
| $\mathbf{I}_3$ | $3 \times 3$ identity matrix |
| $j$ | $j$th |
| $J$ | Jacobian |
| $\mathbf{J}$ | Jacobian matrix |
| $k$ | $k$th |
| $k_0$ | Initial contact stiffness |
| $\boldsymbol{k}_f$ | Vector of multipliers for initial contact stiffness |
| $k_{\mathrm{max}}$ | Magnitude of greatest coefficient in stiffness matrix |
| $k_x$ | Thermal conductivity coefficient in global $X$-direction |
| $k_y$ | Thermal conductivity coefficient in global $Y$-direction |
| $k_z$ | Thermal conductivity coefficient in global $Z$-direction |
| $\mathbf{K}$ | Stiffness matrix |
| $\hat{\mathbf{K}}$ | Modified stiffness matrix |
| $\mathbf{K}^e_C$ | Element heat conduction matrix |
| $\mathbf{K}^e_e$ | Element elastic stiffness matrix |
| $\mathbf{K}^e_G$ | Element stress-stiffening matrix |
| $\mathbf{K}^e_h$ | Element heat convection matrix |
| $\mathbf{K}_{\mathrm{assembly}}$ | Stiffness matrix of assembly |
| $\mathbf{K}_b$ | Bearing stiffness matrix |
| $\mathbf{K}_c$ | Contact stiffness matrix |
| $\mathbf{K}_C$ | Heat conduction matrix |

| | |
|---|---|
| $\mathbf{K}_e$ | Elastic stiffness matrix |
| $\mathbf{K}_{e,\mathrm{CYL}}$ | Elastic stiffness matrix applied with cylindrical constraints |
| $\mathbf{K}_G$ | Stress stiffening matrix |
| $\mathbf{K}_h$ | Surface convection matrix |
| $\mathbf{K}_{\mathrm{shaft}}$ | Stiffness matrix of shaft body |
| $\mathbf{K}_{\mathrm{sleeve}}$ | Stiffness matrix of sleeve body |
| $\mathbf{K}_{\mathrm{tot}}$ | Total stiffness matrix |
| $l$ | Number of |
| $L$ | Length |
| $\mathbf{L}$ | Matrix of partial differential operations |
| $m$ | Number of |
| $\mathbf{M}$ | Mass matrix |
| $\mathbf{M}^e$ | Element mass matrix |
| $n$ | Number of |
| $\boldsymbol{n}$ | Outer normal to the surface of the body |
| $n_{\mathrm{rpm}}$ | Rotational speed |
| $n_x$ | Outer normal to the surface of the body in global $X$-direction |
| $n_y$ | Outer normal to the surface of the body in global $Y$-direction |
| $n_z$ | Outer normal to the surface of the body in global $Z$-direction |
| $N$ | Number of stress cycle repetitions in total |
| $\mathbf{N}$ | Shape function matrix |
| $\boldsymbol{N}$ | Vector of shape functions |
| $\mathbf{N}_1$ | Shape function matrix of node 1 |
| $\mathbf{N}_2$ | Shape function matrix of node 2 |
| $N_f$ | Number of equivalent applied stress cycles |
| $N_i$ | Shape function of node $i$ |
| $\mathbf{N}_i$ | Shape function matrix of $i$th node |
| $\mathbf{N}_j$ | Shape function matrix of $j$th node |
| $\mathbf{N}_n$ | Shape function matrix of node $n$ |
| $p$ | $p$th |
| $\boldsymbol{p}$ | Vector of monomials |
| $\boldsymbol{p}_p$ | Pressure vector |
| $p_w$ | Working precision |
| $p_x$ | Pressure normal component in global $X$-direction |
| $p_y$ | Pressure normal component in global $Y$-direction |
| $p_z$ | Pressure normal component in global $Z$-direction |
| $P$ | Power loss |
| $\mathbf{P}$ | Moment matrix |
| $\boldsymbol{q}$ | Heat flow vector |
| $q_s$ | Boundary heat flow component coefficient |
| $q_x$ | Heat flow component through the unit area in global $X$-direction |
| $q_y$ | Heat flow component through the unit area in global $Y$-direction |
| $q_z$ | Heat flow component through the unit area in global $Z$-direction |
| $Q$ | Internal heat generation rate per unit volume |
| $\boldsymbol{R}_h^e$ | Element surface convection vector |
| $\boldsymbol{R}_q^e$ | Element boundary heat flow vector |

| | |
|---|---|
| $\boldsymbol{R}_Q^e$ | Element internal heat generation vector |
| $\boldsymbol{R}_T^e$ | Element specified boundary temperature vector |
| $\boldsymbol{R}_h$ | Heat convection vector |
| $\boldsymbol{R}_q$ | Boundary heat flow vector |
| $\boldsymbol{R}_Q$ | Internal heat generation vector |
| $\boldsymbol{R}_T$ | Specified boundary temperature vector |
| $S$ | Surface area |
| $\mathbf{S}_0$ | Initial stress matrix |
| $S_e$ | Element surface area |
| $t$ | Time |
| $t_i$ | Time of step $i$ |
| $T$ | Temperature |
| $T_i$ | Temperature of node $i$ |
| $\mathbf{T}$ | Transformation matrix |
| $\dot{\boldsymbol{T}}_N$ | First time derivative of nodal temperature vector |
| $\mathbf{T}_d$ | Transformation matrix containing diagonal terms |
| $T_e$ | Reference temperature for convective heat transfer |
| $T_g$ | Kinetic energy due to gyroscopic effect |
| $T_k$ | Kinetic energy |
| $T_m$ | Kinetic energy of translational motion |
| $\boldsymbol{T}_N$ | Nodal temperature vector |
| $T_s$ | Surface temperature |
| $T_{\mathrm{ref}}$ | Reference temperature |
| $u$ | Nodal displacement in global $X$-direction |
| $\boldsymbol{u}$ | Element displacement vector |
| $\hat{\boldsymbol{u}}$ | Modified displacement vector |
| $\dot{\boldsymbol{u}}$ | First time derivative of displacement vector |
| $\dot{u}_i$ | First time derivative of nodal displacement of node $i$ in global $X$-direction |
| $\boldsymbol{u}'_{0,s}$ | Initial displacement vector of source nodes in cylindrical coordinates |
| $\boldsymbol{u}'_{0,t}$ | Initial displacement vector of target nodes in cylindrical coordinates |
| $\boldsymbol{u}'_{s,i}$ | Displacement of source node $i$ in cylindrical coordinate system |
| $\boldsymbol{u}'_{t,i}$ | Displacement of target node $i$ in cylindrical coordinate system |
| $\boldsymbol{u}_{\mathrm{trial}}$ | Trial displacement vector in global Cartesian coordinate system |
| $\boldsymbol{u}'_{\mathrm{trial}}$ | Trial displacement vector in cylindrical coordinate system |
| $\boldsymbol{u}_0$ | Initial displacement vector |
| $u_i$ | Nodal displacement of node $i$ in global $X$-direction |
| $u_j$ | Nodal displacement of node $j$ in global $X$-direction |
| $u_r$ | Radial displacement in cylindrical coordinate system |
| $\boldsymbol{u}_{\mathrm{shaft}}$ | Displacement vector shaft body |
| $\boldsymbol{u}_{\mathrm{sleeve}}$ | Displacement vector sleeve body |
| $\boldsymbol{u}_{\mathrm{tot}}$ | Total displacement vector |
| $u_w$ | Axial displacement in cylindrical coordinate system |
| $u_x$ | Nodal displacement in global $X$-direction |

| | |
|---|---|
| $u_y$ | Nodal displacement in global $Y$-direction |
| $u_z$ | Nodal displacement in global $Z$-direction |
| $v$ | Nodal displacement in global $Y$-direction |
| $\dot{v}_i$ | First time derivative of nodal displacement of node $i$ in global $Y$-direction |
| $v_i$ | Nodal displacement of node $i$ in global $Y$-direction |
| $V$ | Volume |
| $V_e$ | Element volume |
| $w$ | Nodal displacement in global $Z$-direction |
| $\dot{w}_i$ | First time derivative of nodal displacement of node $i$ in global $Z$-direction |
| $w_i$ | Nodal displacement of node $i$ in global $Z$-direction |
| $W$ | Penalty weight |
| $W_f$ | Work done by external forces |
| $W_i$ | Weight coefficient $i$ |
| $W_j$ | Weight coefficient $j$ |
| $W_k$ | Weight coefficient $k$ |
| $x$ | Nodal coordinate in global $X$-direction |
| $\boldsymbol{x}$ | Nodal coordinate vector in fixed coordinate system |
| $\dot{\boldsymbol{x}}$ | First time derivative of nodal coordinate vector |
| $\ddot{\boldsymbol{x}}$ | Second time derivative of nodal coordinate vector |
| $x_i$ | Integration point $i$ |
| $\boldsymbol{x}_i$ | Vector of coordinates of node $i$ |
| $x_j$ | Nodal coordinate in global $X$-direction of node $j$ |
| $\boldsymbol{x}_j$ | Vector of coordinates of node $j$ |
| $\boldsymbol{x}_n$ | Vector of coordinates of node $n$ |
| $X$ | Cartesian coordinate system axis in global $X$-direction |
| $X'$ | Cylindrical coordinate system axis in global radial direction |
| $y$ | Nodal coordinate in global $Y$-direction |
| $y_i$ | Nodal coordinate of node $i$ in global $Y$-direction |
| $y_j$ | Nodal coordinate in global $Y$-direction of node $j$ |
| $Y$ | Cartesian coordinate system axis in global $Y$-direction |
| $Y'$ | Cylindrical coordinate system axis in global tangential direction |
| $z$ | Nodal coordinate in global $Z$-direction |
| $z_i^c$ | Number of repetitions in $i$th stress class |
| $z_i$ | Nodal coordinate of node $i$ in global $Z$-direction |
| $\boldsymbol{z}_i$ | Eigenvector of $i$th eigenmode |
| $z_j$ | Nodal coordinate of node $j$ in global $Z$-direction |
| $Z$ | Cartesian coordinate system axis in global $Z$-direction |
| $Z'$ | Cylindrical coordinate system axis in global axial direction |

GREEK LETTERS

| | |
|---|---|
| $\alpha$ | Thermal expansion coefficient |
| $\boldsymbol{\alpha}$ | Vector of thermal expansion coefficients |

| | |
|---|---|
| $\alpha_p$ | Proportional coefficient for stiffness matrix |
| $\alpha_x$ | Thermal expansion coefficient in global $X$-direction |
| $\alpha_y$ | Thermal expansion coefficient in global $Y$-direction |
| $\alpha_z$ | Thermal expansion coefficient in global $Z$-direction |
| $\beta$ | S-N curve slope |
| $\beta_p$ | Proportional coefficient for mass matrix |
| $\boldsymbol{\gamma}'_0$ | Vector of logical multipliers |
| $\gamma_{xy}$ | Shear strain in $XY$-plane |
| $\gamma_{xy,0}$ | Initial shear strain in $XY$-plane |
| $\gamma_{xz}$ | Shear strain in $XZ$-plane |
| $\gamma_{yx}$ | Shear strain in $YX$-plane |
| $\gamma_{yz}$ | Shear strain in $YZ$-plane |
| $\gamma_{yz,0}$ | Initial shear strain in $YZ$-plane |
| $\gamma_{zx}$ | Shear strain in $ZX$-plane |
| $\gamma_{zx,0}$ | Initial shear strain in $ZX$-plane |
| $\gamma_{zy}$ | Shear strain in $ZY$-plane |
| $\delta_{\text{rad}}$ | Radial interference |
| $\delta u_i$ | Distance between source and target node $i$ |
| $\Delta L$ | Change of length |
| $\Delta T$ | Change of temperature |
| $\Delta T_n$ | Temperature difference of node $n$ |
| $\Delta \boldsymbol{u}'_0$ | Vector of initial radial distances between source–target nodes in cylindrical coordinates |
| $\Delta \boldsymbol{u}'_{\text{trial}}$ | Vector of radial distances between source–target nodes in cylindrical coordinates after trial force evaluation |
| $\Delta u'_{\text{trial},i}$ | Radial distances between source and target node $i$ in cylindrical coordinates after trial force evaluation |
| $\Delta \sigma$ | Stress variation |
| $\Delta \sigma_{\text{eq}}$ | Calculated equivalent stress |
| $\epsilon$ | Strain |
| $\boldsymbol{\epsilon}$ | Strain vector |
| $\boldsymbol{\epsilon}_0$ | Initial strain vector |
| $\epsilon_x$ | Normal strain in $X$-direction |
| $\epsilon_{x,0}$ | Initial normal strain in $X$-direction |
| $\epsilon_y$ | Normal strain in $Y$-direction |
| $\epsilon_{y,0}$ | Initial normal strain in $Y$-direction |
| $\epsilon_z$ | Normal strain in $Z$-direction |
| $\epsilon_{z,0}$ | Initial normal strain in $Z$-direction |
| $\zeta$ | Natural coordinate |
| $\zeta_i$ | Integration point $i$ |
| $\zeta_k$ | Integration point $k$ |
| $\zeta_l$ | Natural coordinate $\zeta$ of node $l$ |
| $\eta$ | Natural coordinate |
| $\eta_i$ | Integration point $i$ |
| $\eta_j$ | Integration point $j$ |
| $\eta_l$ | Natural coordinate $\eta$ of node $l$ |

| | |
|---|---|
| $\theta$ | Rotational degree of freedom |
| $\dot{\theta}_x$ | First time derivative of nodal rotation around global $X$-axis |
| $\dot{\theta}_y$ | First time derivative of nodal rotation around global $Y$-axis |
| $\dot{\theta}_z$ | First time derivative of nodal rotation around global $Z$-axis |
| $\theta_x$ | Nodal rotation around global $X$-axis |
| $\theta_y$ | Nodal rotation around global $Y$-axis |
| $\theta_z$ | Nodal rotation around global $Z$-axis |
| $\kappa$ | Number of the rainflow stress classes |
| $\lambda$ | Lagrangian multiplier |
| $\boldsymbol{\lambda}$ | Vector of Lagrangian multipliers |
| $\lambda_i^i$ | Imaginary part of eigenvalue $i$ |
| $\lambda_i^r$ | Real part of eigenvalue $i$ |
| $\lambda_i$ | Eigenvalue of $i$th eigenmode |
| $\nu$ | Poisson's ratio |
| $\xi$ | Natural coordinate |
| $\xi_i^d$ | Damping ratio of $i$th eigenmode |
| $\xi_i$ | Integration point $i$ |
| $\xi_l$ | Natural coordinate $\xi$ of node $l$ |
| $\Pi$ | Strain energy |
| $\rho$ | Material density |
| $\boldsymbol{\sigma}$ | Element stress vector |
| $\sigma_f'$ | Fatigue strength coefficient |
| $\boldsymbol{\sigma}_{\mathrm{brg}}$ | Bearing stress vector |
| $\sigma_{\mathrm{eq}}$ | Equivalent stress |
| $\sigma_{\mathrm{max}}$ | Maximum stress |
| $\boldsymbol{\sigma}_{\mathrm{rotor}}$ | Rotor stress vector |
| $\sigma_x$ | Normal stress in $X$-direction |
| $\sigma_y$ | Normal stress in $Y$-direction |
| $\sigma_z$ | Normal stress in $Z$-direction |
| $\tau$ | Torque |
| $\tau_{xy}$ | Shear stress in $XY$-plane |
| $\tau_{xy,0}$ | Initial shear stress in $XY$-plane |
| $\tau_{xz}$ | Shear stress in $XZ$-plane |
| $\tau_{yx}$ | Shear stress in $YX$-plane |
| $\tau_{yz}$ | Shear stress in $YZ$-plane |
| $\tau_{yz,0}$ | Initial shear stress in $YZ$-plane |
| $\tau_{zx}$ | Shear stress in $ZX$-plane |
| $\tau_{zx,0}$ | Initial shear stress in $ZX$-plane |
| $\tau_{zy}$ | Shear stress in $ZY$-plane |
| $\omega_{d,i}$ | Damped natural frequency of $i$th eigenmode |
| $\omega_{n,i}$ | Undamped natural frequency of $i$th eigenmode |
| $\omega_x$ | Angular velocity around global $X$-axis |
| $\omega_y$ | Angular velocity around global $Y$-axis |
| $\omega_z$ | Angular velocity around global $Z$-axis |
| $\Omega$ | Rotational speed |
| $\boldsymbol{\Omega}$ | Rotational speed matrix |

| | |
|---|---|
| $\dot{\Omega}$ | Angular acceleration |

ABBREVIATIONS

| | |
|---|---|
| 1D | One-dimensional |
| 2D | Two-dimensional |
| 3D | Three-dimensional |
| AMB | Active magnetic bearing |
| BM | Bending mode |
| BW | Backward whirl |
| CAD | Computer-aided design |
| CS | Critical speed |
| DOF | Degree of freedom |
| EMA | Experimental modal analysis |
| FE | Finite element |
| FEA | Finite element analysis |
| FEM | Finite element method |
| FW | Forward whirl |
| MPC | Multipoint constraint |
| PMSM | Permanent magnet synchronous motor |

# Introduction

Rotating machines are used in various processes, such as transforming energy from one form into another. Commonly, electrical energy is transformed into mechanical rotational motion or vice versa. As the rotational machines are developed, they get more optimized and efficient. Traditional industrial electrical motor-driven blowers use a low-speed electric motor and a transmission to increase the rotational speed for the blower. By getting rid of the transmission – typically the main source of unwanted frictional losses – as well as designing the electrical motor for increased rotational speed applications resulting in a direct-driven system, the total efficiency of the system can be increased. This type of machine is generally called a high-speed machine. The benefits of proceeding towards high-speed technology are generally the smaller size and weight of the rotating machines. Also, a greater power density and better efficiency of fluid flow process in various industrial process components such as high-speed electrical fans, blowers and pumps, are achieved.
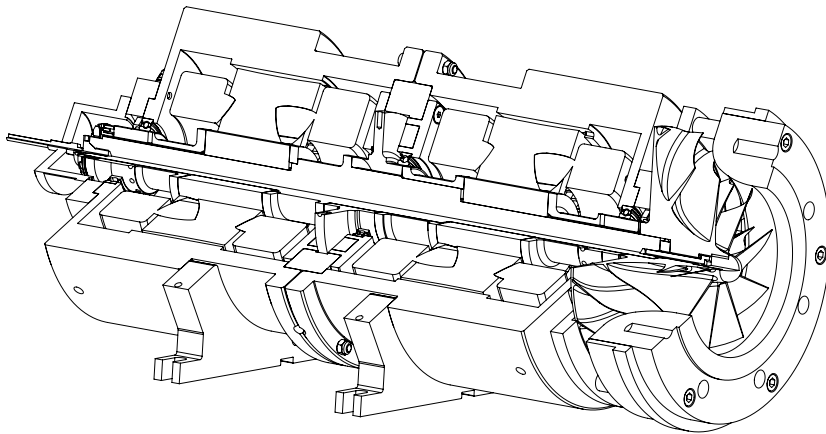


**Figure 1.1.** Cut view illustration of a magnetically levitated high-speed compressor unit

Modern high-speed rotating machines consist of multiple parts. A cut view of a magnetically levitated high-speed compressor unit is shown in Figure 1.1. A rotor of a high-speed motor has typically one main shaft component and a number of other components, such as impellers and lamination stacks, depending on the motor-rotor type and bearing solution, attached on the shaft. Quite often, these parts are attached using a frictional joint. These joints are capable of causing nonlinearities in the rotating structure dynamics.

A high-speed rotating operation is that which, from the mechanical point of view, could be regarded as a rotating operation having the peripheral velocity of the rotation part high enough, typically above 150 m/s [85]. The angular velocity or revolutions per minute is a relative quantity, and thus should not be considered as a definition for high-speed. The strength of material is typically the limiting factor for high-speed machine design. Often, in rotating high-speed machines, the strength of the material used sets the upper limit for the rotational speed.

In addition to loads induced by high-speed rotation, heat loads induced by power loss of an electrical machine should be taken into account in the form of thermal stress. This doctoral dissertation examines high-speed rotating structures, commonly referred as rotors. The research on these rotors – rotor assemblies as more detailed in most cases – is a special field and a part of structural dynamics referred to as *rotor dynamics*. The main tool used in this dissertation is the three-dimensional solid finite element method, as part of the finite element method used within the field of structural engineering.

## 1.1   Motivation

The interest for programming 3D solid finite element problems arises from the capability to use customized contact models and solution routines for coupled analyses, thus extending the capabilities of commercial FE software. Coupled analysis can be, for example, a combined thermal structural stress analysis: in the first phase, the temperature state is solved and used as an input for the second phase. The solved temperature distribution is applied as an initial thermal strain, thus contributing the total stresses in a form of thermal stress.

Another example of coupled analysis can be a static structural–modal analysis, or pre-stressed modal analysis, in order to include the effect of external structural loads in the modal analysis. An eigenvalue problem cannot handle structural loads directly: thus, a static structural analysis is performed to solve the stress state of the structure. The solved stress state can be included into the eigenvalue problem as a pre-stress state by utilizing the stress-stiffening effect; an additional stiffness matrix to represent the stress-stiffening effect can be formed using the pre-solved stress state of the structure.

Many commercial FE software can be used to solve coupled field problems as described above. Even so, performing an analysis using self-programmed solution routines and finite elements may be required in certain cases if commercial software does not support a particular analysis routine. For example, a control design for

active magnetic bearing using a 3D solid element rotor model having multiple contact and possible contact-induced disturbances.

## 1.2 Literature survey

Rotor dynamics analysis is an important part of the design process in high-speed machinery design. The traditional one-dimensional (1D) Timoshenko beam element approach in rotor dynamics can represent only flexible shafts, while the disks and impellers are modeled as rigid mass points. [74, 73, 34] Although this element type can have degrees of freedom (DOFs) in up to three dimensions, it is commonly referred as 1D element because of the element formulation. Beam elements are actively used because of their benefits: a low number of degrees of freedom is required to represent a full rotor model. Because of a low number of DOFs, transient simulation for solving nonlinear problems is fast and design optimization is easy to implement. These 1D elements do not normally take into account the deformation of the shaft cross section. In certain rotating machinery applications, the effect of deformable shaft cross sections for flexible disks and turbine blades are required to be included into the simulation model. These features enable the inclusion of the stress-stiffening effect, meaning that the total stiffness of the rotor assembly is affected by the internal stress of the component. [32] These effects can be included when using two-dimensional (2D) axisymmetric harmonic or three-dimensional (3D) solid finite elements. [35, 69, 80] The use of a 2D element is typically limited to axisymmetric structures and axisymmetric loads, whereas 3D elements in practice can be used to describe any rotating structure. In addition, high-fidelity coupled field analyses become easier to implement when using the same solid finite element mesh for various analyses.

The use of three-dimensional solid finite elements in rotor dynamic analysis allows the inclusion of nonlinear contact behavior in the study of a rotor assembly. Modern complex rotor assemblies used in high-speed rotating machinery can include multiple parts with various types of joints as shown in Figure 1.1. The contact modeling and inclusion of frictional joint-based excitations are features that have been challenging to include in the analysis when using the conventional beam element approach. The use of axisymmetric elements will limit the capabilities to model arbitrary external loads and load directions. Therefore, the use of 3D solid finite element approach is a solution for the detailed modeling of contact-based phenomena. Additional phenomena, such as centrifugal stiffening or stress stiffening, will yield further accuracy in the finite element solution. Centrifugal stiffening is derived from the centrifugal load only; whereas stress stiffening is derived, not only from centrifugal load, but from all external loads being taken into consideration.

### 1.2.1 Rotor dynamics modeling using finite element method

In certain applications, such as turbines, fans and pumps, high-speed motors can be more suitable due to process-based demands than lower speed motors which rotate

at the power grid frequency, since high-speed motors can operate without the need for transmission. In some applications, mechanical bearings are not suitable for supporting the rotor of high-speed electrical motors, because mechanical bearings require lubrication, can wear out, and the occurring vibrations, as a result of rotor-bearing contact, could be critical. Active magnetic bearings (AMBs) are often seen as the answer to the demand of supporting the high-speed rotor, since they do not have mechanical contact, and they are also oil-free. In addition, the efficiency of an AMB-supported rotor is better than that of a conventional rolling element bearing-supported rotor, as the system lacks contact-induced friction. Furthermore, the stiffness of AMBs can be adjusted for recovering possible critical speed or other disturbance, and the rotor lateral position and axial clearances can be adjusted if so desired.

However, a failure can occur in the AMB system, and for this reason the backup bearings – typically a set of rolling element bearings – are used to support the rotor in any eventual abnormal operation. In practice, this means that, due to the backup bearings, possible contact is avoided between the stator of the electric motor or stator of the AMBs and the rotating rotor. The AMB-supported rotor dropdown event has been clarified extensively. For instance, in studied by Ishii and Kirk [40], Zeng [97] and Cole *et al.* [19] the dropdown event between the rotor and bearing is examined, covering the views of modeling the stiffness, damping and friction. They studied the dynamic behavior of a rolling element backup bearing after rotor impact and stated that for minimizing the energy dissipation in the inner ring of the bearing, it should be allowed to accelerate as rapidly as possible in order to minimize the friction-induced whirling of the rotor.

In previous research, significant research has been performed in the studying of AMB-supported rotor deflections. Schmied and Pradetto [88] did one of the first studies in the field of the contact event between AMB-supported rotor and backup bearings. In the recent years, the rotor deflections have been investigated in normal runs of the AMB-supported rotor, as in Jalali *et al.* [42] and Stimac *et al.* [93]. In Jalali *et al.*, the theoretical and experimental results from a high-speed rotor are found to be in good agreement. The rotating system is studied by means of the Campbell diagram, and critical speeds and operational deflection shapes are obtained. In Stimac *et al.*, the finite element method based on Bernoulli-Euler beam element theory is used for the rotor model. Frequency responses of the system model with amplitudes in rotor lateral displacements are verified by means of measured results. Zhou *et al.* [100] investigated cracked shafts supported with AMBs. The contact region of even a slight crack can open or close due to the normal rotation of the shaft and can thereby produce an excited dynamic system. Therefore, it is critical to examine rotor stresses, as the rotor stress state may initiate the rotor cracks. Nevertheless, the stresses that arise in the rotor itself have not been examined in the literature.

A limited number of publications can be found that particularly focus on bearing life and the stress analysis of backup bearings. Stress and life time are important issues for engineers designing backup bearings, especially since the rolling element in backup bearing applications undergoes exceptional loading. Sun [94] estimated

the fatigue life of the backup bearing. He evaluated the Hertzian contact stresses and implemented Lundberg-Palmgren method to approximate the fatigue life of the bearing. The Lundberg-Palmgren method is applicable only for steady state loading conditions, while the loading of backup bearing is varies with regard to the time period. After a few years, Lee and Palazzolo [55] applied rainflow analysis to consider the time-dependent stress in evaluating the fatigue life of backup bearing.

The use of beam element-based modeling for transient problems, such as rotor dropdown event or other purposes such as solving stress history of backup bearing, has proven to be useful – and is still in active use, despite its limitations with regard to the detailed modeling capabilities of the rotor geometry.

General 3D rotor dynamics modeling is discussed in Jalali *et al.* [42], where the modal results of beam and 3D modeling approaches are compared against experimentally measured results. In Kumar *et al.* [53], an aircraft engine strength and life time analysis is given, where transient forces including gyroscopic loads during maneuvers are included. For the life time analysis, a flight cycle profile is used. In [69] is given a general 3D theory for rotor dynamics modeling using both the rotating frame of reference approach, which includes the Coriolis and spin softening effects, and the fixed frame of reference approach.

A multistage rotor system of a high-speed pump is investigated by Jammi [43]. The rotor system consists of three rotors on the same axis of rotation that are coupled, as well as multiple supports using rolling element bearings. Moreover, the effect of seals and nonlinear stiffness of the bearings and flexible pump frame are included in the analysis. In addition, the pressure inside the pump during operation is studied, and it is shown that the pressure is causing a pre-stress effect on the frame. Multiple Campbell diagrams are presented showing the simulated response when the frame is taken into account and when the pre-stress condition of frame is added.

The sub-synchronous rotor dynamic instability caused by the shrink fit interface is studied by Jafri [41]. The experimental studies showed that above the first critical speed of the rotor system, due to the shrink fit interface, a strong unstable sub-synchronous vibration occurred. In [41] was stated that the unstable sub-synchronous vibration originate from friction forces which are developed by the slippage in the shrink fit interface. It was stated that the slippage-induced friction forces are acting as destabilizing cross coupled moments, while the rotor is operating above the first critical speed. Transient whirl behavior including stress stiffening and spin softening effects is studied by Rao [81] in which the unbalance response and stability of the rotor-bearing system is analyzed during acceleration.

Chen *et al.* [14] used Ansys to perform a pre-stressed modal study of a hollow shaft assembly with shrink fit joints. They used the native contact elements TARGE170 and CONTA174. They performed an experimental modal analysis (EMA) in order to verify the numerical results. A similar study was presented by Chen [13], where an optimal equivalent direct model was proposed for manipulating the local stiffness in the contact region, by means of optimizing the elastic modulus of the material.

The effect of stress stiffening is shown as an important aspect to take into account in any finite element-based frequency analysis. Kupnik *et al.* [54] showed how significantly the natural frequencies of a gas turbine blade can be affected by inclusion of the stress-stiffening effect. Donaldson *et al.* [23] presented the results of change in harmonic response frequencies of an ultrasonic transducer while the stress-stiffening effect is included.

An opposite effect to stress stiffening is an effect called spin softening. Rao and Sreenivas [82] reported spin softening having significant effect on critical speeds and the unbalance response. Later, Genta and Silvagni in [33] and [34] criticized the importance of the spin softening effect. It was shown that with speeds high enough – i.e., well beyond the speed of mechanical integrity – the effect is becoming visible. Unlike the stress-stiffening effect, the spin-softening effect is not depended on rotor geometrical interactions, such as contact induced stress. Instead, the magnitude of this effect is directly dependent on rotor spin speed and the material properties used. Thus, at speeds achievable before the material strength limit is met, the spin-softening effect seems negligible.

General finite element contact problems are discussed by Zhang and Wang [98], in which translational joint contact with friction force is studied in 2D. In Nejati, Paluszny and Wimmerman [72], an internal friction of contact on a cracked region is studied. Many publications considering the use of a traditional beam such as Santos *et al.* [86] and Chen *et al.* [15] typically present a case-dependent solution for a contact problem in shrink-fitted sleeve–shaft contact. The solution is achieved in most cases by tuning the sleeve material properties based on the theory developed.

Bolted structures with the impact of the preload effect are studied by Kim *et al.* in [47], using the solid finite element method. Their study involved the use of commercial FE-software (Ansys) and using its contact element methods. Multiple bolted joint-modeling approaches are studied; use of solid elements, spider mesh with beam elements, spider mesh with direct degree of freedom coupling and a custom proposed method that does not use additional finite elements, but the pressure load is mapped on the washer area in order to provide a preload effect.

Other interesting types of contacts used in rotating machines are studied in Richardson *et al.* [84] and Qin *et al.* [79]. In [84], the bolt-jointed Curvic coupling is studied, using the 3D FE method. The Curvic coupling is used typically in aero-engines for transmitting torque between a sectioned rotor using a set of matching axial teeth having a similar analogy as Hirth coupling. In [79], the joints of the bolted disk-drum are studied using a formulated analytical model, and the FE approach using Ansys software.

Sasek [87] studied the sensitivity of eigenvalues in the flexible rotor-disk system. He proposed a method of using individual subsystems, one for the flexible disk, and another for the shaft. These subsystems were connected using a global coupling force vector. Tannous *et al.* [95] introduced an interesting approach for transient rotor dynamics analysis using beam and 3D element modeling approaches, while allowing the switch from beam to 3D during the transient solution. The

main benefit, besides computational efficiency, is the detailed transient modeling for events such as rotor-stator contact. The method proposed is proven and the inertial, velocity and acceleration corrections due to the model switch are implemented.

Wagner *et al.* [96] presented a comprehensive review of modal reduction methods that can be used for rotor dynamics analysis. A discussion of the suitability of various methods was given. 3D solid element modeling is used as the basis for the beam element-based rotor model update for the dual rotor system studied by Miao *et al.* [68]. The optimization of model updating and performance gained is discussed.

Inclusion of a flexible frame for a comprehensive dynamic response analysis of a rotating machinery is beneficial. Mounting of frame to the foundation and the machine foundation modeling itself are aspects that determine the accuracy of the harmonic response of machine frame and foundation. Machine foundation properties are investigated in Prakash and Puri [78], in which a number of analytical stiffness and damping coefficient equations are provided for various basic types of machine foundation. Vibration isolation and absorption for machine foundations is investigated in Öztürk and Öztürk [105].

### 1.2.2 Thermal stress modeling using finite element method

Study of the thermal condition in a structure can be important for calculating the stress condition of the structure. Even a small temperature difference over the structure may yield a moderate initial stress state, due to the thermal expansion-induced forces inside the structure. Thermal FEM is typically done prior to structural strength analysis, and used as the loading condition in the structural analysis. Measured on-board diagnostics data of a vehicle is used for transient thermal stress studies by Rashid and Strömberg [83], where frictional heating of disc brakes was studied. The coupled field problem of thermal stress analysis for a 3D cut disk structure is studied by Paramonov and Gonin [77]. Abawi [1] presented thermal stress-induced bending in a non-homogeneous composite structure. Chen and Nelson [17] studied thermal stress distribution in bonded joints. Measured drive cycle data of a vehicle was used as the basis for transient thermal stress studies in Sikanen *et al.* [92], where the thermal stress history and life time calculation is given for a traction motor application.

Combined mechanical and thermal loads were studied in Çallioğlu *et al.* [7] where the application studied was functionally graded rotating discs. A similar approach is studied in Celebi *et al.* [11], where stress due to a steady-state thermal condition with mechanical loads was studied for a thick-walled cylinder made of functionally graded material. Ma and Wang [66] investigated thermal post-buckling of a functionally graded circular plate under thermal, mechanical and combined thermal mechanical loads.

An analytical expression for calculating thermal stress in a receiver tube used at a solar energy plant is formulated in Logie *et al.* [62]. Thermal stress is also a

relative issue in electrical engineering and printed circuit board design. In Lu *et al.* [65], Lu *et al.* [64] and Jiang *et al.* [45], thermal stresses of through-silicon-vias connectors were studied.

Gabrielson [30] provided multiple approaches for calculating temperature and material damping-dependent mechanical thermal noise in micromachined acoustic and vibration sensors. Lin and Lee [57] studied residual stresses in a machined workpiece using an FEM approach with a large deflection thermal elastic-plastic method.

Thermal fatigue of a reinforced composite under thermal and mechanical loads is investigated in Long and Zhou [63], using experimental and numerical analysis. Zhao *et al.* [99] studied a composite disk clutch system using a coupled transient temperature-displacement analysis in order to investigate the thermomechanical behavior of the system under frictionally induced thermal loads.

Thermal stresses are studied also in the field of electric vehicular technology. There are many varying traction motor drives and drivetrain architectures that have been proposed for electric vehicle use [22, 25, 5]. In traction motor applications, the operating conditions vary significantly: the multidisciplinary analysis should be conducted over the drive cyclea as was done, for example, in Fatemi *et al.* [26]. In [21, 6], electromagnetic forces are applied in mechanical analysis to find out the noise and vibration characteristics.

The calculation of structural stresses and the fatigue life of a permanent magnet synchronous motor (PMSM) rotor structure in traction applications is often based on varying analytical and finite element-based numerical approaches. According to the results found in Chai *et al.* [12], Knetsch *et al.* [49], and Lindh *et al.* [58], centrifugal force acting on the rotor structure is regarded as the dominant stress source, but in all the cases studied, the effect of the thermal loads on mechanical stresses and fatigue life were neglected.

Stress levels are directly coupled with the fatigue life, which can be analyzed by various methods, as introduced in [56]. According to the published literature, the main interest in the impacts of thermomechanical stress in electrical machines is limited to the rotor bar braking mechanisms in squirrel-cage induction machines [18], or degradation of stator insulation [44]. In the traditional mechanical design of the rotor structure of a permanent magnet traction motor, thermomechanical stresses are typically neglected, leading to a situation where the mechanical design is based mostly on the centrifugal forces affecting the rotor.

## 1.3   Objectives and scientific contribution

There seems to be a limited number of publications regarding the rotor stresses occurring from the contact with backup bearings. The stresses occurring in the rotor from contact between the rotor and backup bearings can be a limiting issue, especially in flywheel applications, which often use AMBs.

All the results presented in publications regarding contact studies using 3D solid elements are made using commercial FE software. Typically, Ansys is used with

native TARGE170 and CONTA174 contact elements. These elements can be considered to be general purpose contact elements. By default, the constraint equation method Ansys uses with these elements is augmented Lagrangian. It is a very practical method, since under normal circumstances the convergence of the contact is rapid. Based on the publications found related to solid finite element rotor dynamics modeling, it appears to be that the use of 3D solid elements for contact modeling without using commercial FE software is a topic that is not much studied. There also seems to be only a limited number of publications regarding coupled field static structural–modal analysis studies for rotor dynamics analysis in the frequency domain.

In literature, coupled field thermal structural stress analyses also lean on the use of commercial FE software. According to literature, a typical traction motor design is based on taking only centrifugal forces into account and neglecting the effect of thermal stresses. A limited number of publications regarding detailed thermal stress analysis as based on measured loading history in the field of structural analysis of electric vehicles exists.

The objectives of this doctoral dissertation are as follows:

- To prove how important proper contact modeling for rotor critical speed analysis is. For a multi-step modal analysis such as making a Campbell diagram, updating the loading and contact status on every speed step can be essential.

- To provide new information about the importance of the impact of thermal stress during rotating machine operation. In addition to a steady state condition, transient thermal effects should also be analyzed. Although this work does not focus on fatigue life calculation, an introduction to the theory is presented and implemented in the results section.

This doctoral dissertation provides the following scientific contribution:

- The effect of contact status-induced nonlinearities affecting rotor eigenfrequencies is proven. The forces induced by high-speed operation can partially open a certain type of contacts in rotor assemblies having multiple parts. This contact opening is documented and is shown to cause shifting in the rotor whirling mode frequencies. Operational conditions, such as high spin speed-induced deformations and uneven temperature distribution, can have an effect on the rotor critical speeds when an analysis is done using the three-dimensional solid finite element modeling approach, including custom contact formulations.

- Taking into account the thermal condition while analyzing the stress state of components of rotating machines has proven to be indispensable. A computationally efficient coupled field solution routine is proposed for thermal stress analysis. A significant reduction of fatigue life in a traction

motor rotor, while including the transient thermal stress state, is proven. Besides the analysis of steady-state condition, it is also important to analyze various transient operational points.

- Analyses of rotor and bearing stress conditions during transient rotor dropdown on backup bearings are proven to be essential for machine design. Rotor stress history during dropdown can be crucial information for rotor design. Similarly, the stress history of backup bearing is essential for bearing life.

## 1.4 Published articles

This doctoral dissertation includes research from the following publications:

- Sikanen, E., Heikkinen, J. E. and Sopanen, J., 2018, "Shrink-Fitted Joint Behavior Using Three-Dimensional Solid Finite Elements in Rotor Dynamics with Inclusion of Stress-Stiffening Effect," *Advances in Mechanical Engineering*, 10(6), pp. 1–13.

- Sikanen, E., Nerg, J., Heikkinen, J. E., Gerami Tehrani, M. and Sopanen, J., 2018, "Fatigue Life Calculation Procedure for the Rotor of an Embedded Magnet Traction Motor Taking into Account Thermomechanical Loads," *Mechanical Systems and Signal Processing*, 111, pp. 36–46.

- Neisi, N., Sikanen, E., Heikkinen, J. E. and Sopanen, J., 2018, "Effect of Off-Sized Balls on Contact Stresses in a Touchdown Bearing," *Tribology International*, 120, pp. 340–349.

- Sikanen, E., Halminen, O., Heikkinen, J. E., Sopanen, J., Mikkola, A. and Matikainen, M., 2015, "Stresses of an AMB-Supported Rotor Arising from the Sudden Contact with Backup Bearings," *Proceedings of the ASME 2015 International Mechanical Engineering Congress and Exposition IMECE2015*.

The other published articles that falls apart from the core of this dissertation:

- Neisi, N., Heikkinen, J. E., Sikanen, E. and Sopanen, J., 2017, "Stress Analysis of a Touchdown Bearing Having an Artificial Crack," *ASME International Design Engineering Technical Conferences and Information in Engineering Conference IDETC/CIE*.

- Jaatinen-Värri, A., Nerg, J., Uusitalo, A., Ghalamchi, B., Uzhegov, N., Smirnov, A., Sikanen, E., Grönman, A., Backman, J. and Malkamäki, M., 2016, "Design of a 400 kW Gas Turbine Prototype," *Proceedings of ASME Turbo Expo 2016: Turbine Technical Conference and Exposition GT2016*.

- Sikanen, E., Jastrzebski, R., Jaatinen, P., Sillanpää, T., Smirnov, A., Sopanen, J. and Pyrhönen, O., 2016, "Mechanical Design of Reconfigurable Active Magnetic Bearing Test Rig," *The 15th International Symposium on Magnetic Bearings ISMB15.*

- Jaatinen, P., Sillanpää, T., Jastrzebski, R., Sikanen, E. and Pyrhönen, O., 2016, "Automated Parameter Identification Platform for Magnetic Levitation Systems: Case Bearingless Machine," *The 15th International Symposium on Magnetic Bearings ISMB15.*

# Finite element modeling of rotating structures

Finite element modeling based on the use of beam element approach has been used for many decades for rotor dynamics modeling and simulations. Various beam element formulations have been developed. Nowadays, the most commonly used approach is based on the shear deformable Timoshenko beam theory. Beam elements for rotor dynamics modeling are typically 3D formulations, and they describe volumes efficiently with certain symmetry-based limitations. [80]

Use of the beam element approach makes finite element modeling efficient for various problems, such as transient and eigenvalue analyses. Further simplification can be achieved by using modal reduction, or other dynamic condensation method [96]. Modeling of the gyroscopic effect is fairly simple with beam elements, since these elements typically have shape functions describing the rotational DOFs [16]. Various rotor-stator contacts, such as a seal rub, are typically handled using analytical-based contact force expressions.

Normally, beam elements do not take into account the deformation of the shaft cross section accurately enough. The effect of deformable shaft cross section for flexible disks and turbine blades are required when analyzing certain types of applications such steam turbines. In addition, contacts between different components of the rotor assembly cannot be modeled realistically, although good approximations can be modeled using, for example, speed or otherwise dependent spring elements between the shaft and sleeve components. Centrifugal or, in general, stress-stiffening effects typically cannot be included in beam element-based modeling. Major limitations in including thermal effects also exist. [80]

Many of these limitations can be fixed when using 2D axisymmetric harmonic elements. [35, 80] The use of a 2D element is typically limited to geometries of axisymmetric structures and axisymmetric loads. When introducing 3D solid element modeling, the geometrical limitations-related cross section and loading conditions are also excluded.

The need for a switch from the beam element in the 3D solid element approach

arises from the need for more detailed geometric modeling. Perhaps the most important feature of solid element is the inclusion of contact induced effects in rotor assemblies having multiple parts. The modeling of body forces such as centrifugal force becomes important for a rotor assembly having multiple parts, thus having multiple contacts. The inclusion of a realistic thermal state also becomes possible to model. Centrifugal force and other forces such as thermal expansion and contact induced forces can cause stress stiffening, which is known to have an effect on the eigenfrequencies of the rotating structure.

In this chapter, the fundamentals of the structural and thermal three-dimensional solid finite element for rotor dynamics modeling are given. Although, the 3D structural and thermal modeling of rotating structures is the main topic in this chapter, a brief introduction to beam element-based modeling is given. The importance of including thermal modeling arises from the typical operational conditions of rotating machinery. Electrical losses can appear as an internal heat source in rotors, especially in electric machines. These losses can change the temperature state of the rotor significantly, and if temperature gradients appear, the thermal expansion-induced forces should be studied for two reasons. Because the thermal expansion effect can cause force distributions having significant magnitude, the stress state of the structure should be studied. Also, the thermal expansion-induced forces will cause deformations of the structure; thus, the effect of thermal state on the structure shape should be studied.

Constraint equations as part of rotor modeling having multiple parts are introduced. The generally used constraint equations introduced represent a fundamental part of this dissertation, because the same constraint equations can be applied for both beam element and 3D solid element-based modeling. Common constraint equation methods are presented, and a custom application-specific constraint method developed in [91] is introduced. In addition, constraint equations can be applied essentially in any kind of structural finite element study examining static, transient, modal and harmonic response. The use of a suitable constraint equation method for a particular study requires an understanding of the behavior of various constraint methods. Some constraint methods are not well-suited for transient studies, and others may yield numerical error due to the excessively high stiffness coefficients used.

Solution routines for various coupled field analyses are presented. These routines are used to generate the results presented in this work. Solution routines for transient simulation for solving the rotor and bearing stresses during the dropdown event, using the beam element approach and generating a Campbell diagram for a rotor having multiple parts with contacts using the 3D solid element approach, are presented. In addition, routines for the modeling of transient effects of thermal expansion induced stresses in rotating structures as well as the solved transient stress history, which can be used as an input for fatigue life calculation, are presented.

Beam element-based rotor dynamics modeling is still common. Regardless of certain limitations in the beam element approach, it is found to be extremely

useful in transient analyses. Beam element-based transient analyses are discussed in [71] and [90]. Because the work done in these publications does form a significant part of this dissertation, an introduction to the beam element approach is given here. The general equations of motions are presented especially for beam element purposes. An illustration of beam element having a circular shaped cross section is presented in Figure 2.1. Typical beam element used has six nodal degrees of freedom: $\{u_x \quad u_y \quad u_z \quad \theta_x \quad \theta_y \quad \theta_z\}$. Comprehensive theory section of formulating beam element shape functions and structural matrices is given in [16].
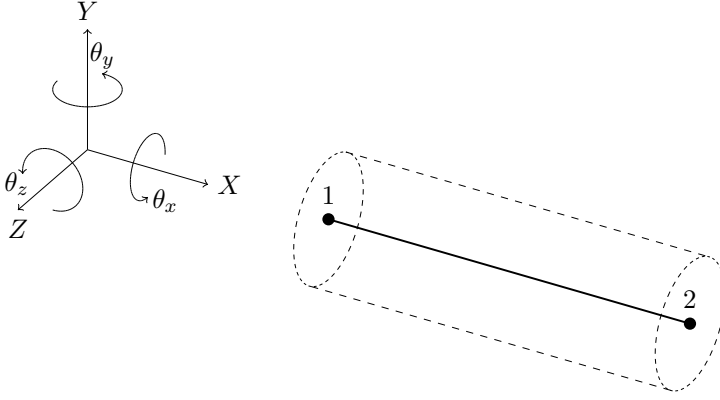


**Figure 2.1.** 2-node beam element having a circular shaped cross section

Equations of motion in fixed frame of reference for general finite element modeling having variable rotation speed is [50]

$$\mathbf{M}\ddot{\boldsymbol{x}} + (\mathbf{C}_e + \Omega\mathbf{G})\,\dot{\boldsymbol{x}} + \left(\mathbf{K}_e + \frac{1}{2}\dot{\Omega}\mathbf{G}\right)\boldsymbol{x} = \Omega^2\boldsymbol{F}_{\mathrm{UB}} + \dot{\Omega}\boldsymbol{F}_{\alpha,\mathrm{UB}} + \boldsymbol{F}_{\mathrm{ext}} \qquad (2.1)$$

where

| | |
|---|---|
| $\mathbf{M}$ | is the mass matrix |
| $\mathbf{C}_e$ | is the elastic damping matrix |
| $\Omega$ | is the rotational speed |
| $\mathbf{G}$ | is the skew-symmetric gyroscopic matrix |
| $\mathbf{K}_e$ | is the elastic stiffness matrix |
| $\boldsymbol{x}$ | is the nodal coordinate vector in a fixed coordinate system |
| $\boldsymbol{F}_{\mathrm{UB}}$ | is the unbalance force vector at constant rotational speed |
| $\dot{\Omega}$ | is the angular acceleration |
| $\boldsymbol{F}_{\alpha,\mathrm{UB}}$ | is the unbalance force vector due to angular acceleration [16] |
| $\boldsymbol{F}_{\mathrm{ext}}$ | is the external force vector |

Rotational speed dependent matrix $\mathbf{G}$ and vector $\boldsymbol{F}_{\mathrm{UB}}$ are formed using reference speed of 1.0 rad/s. Angular acceleration dependent vector $\boldsymbol{F}_{\alpha,\mathrm{UB}}$ is formed using reference acceleration of 1.0 rad/s$^2$. In Equation (2.1), internal damping of the rotor is neglected [50].

## 2.1 Finite element method for 3D solids

In this section, 3D solid finite element theory focusing on the use of rotor dynamics applications for structural and thermal modeling is presented. First, an introduction to solid finite elements is given. Then, the formulation of structural element matrices and force vectors based on energy principle is presented. Finally, the heat transfer theory related to the rotor dynamics application is presented, and element matrices and load vectors based on Galerkin formulation for 3D solid finite element method are shown.

The equations of motion presented in Equation (2.2) are formulated for a fixed frame of reference. The equation presented is meant for problems utilizing the solution of eigenvalue problem, such as making the Campbell diagram, as well as studying contact behavior in the rotor structure. For this reason, time-dependent terms, such as centrifugal force, are not present. The equations of motion for studying rotating structures utilizing 3D solid finite element theory, modified from [48], can be written as follows:

$$\mathbf{M}\ddot{\boldsymbol{x}} + \left(\mathbf{C}_e + \Omega\mathbf{G}\right)\dot{\boldsymbol{x}} + \mathbf{K}_e\boldsymbol{x} = \Omega^2\boldsymbol{F}_\Omega + \boldsymbol{F}_{\text{ext}} \tag{2.2}$$

where

| | |
|---|---|
| $\mathbf{M}$ | is the mass matrix |
| $\mathbf{C}_e$ | is the elastic damping matrix |
| $\Omega$ | is the rotational speed |
| $\mathbf{G}$ | is the skew-symmetric gyroscopic matrix |
| $\mathbf{K}_e$ | is the elastic stiffness matrix |
| $\boldsymbol{x}$ | is the nodal coordinate vector in fixed coordinate system |
| $\boldsymbol{F}_\Omega$ | is the centrifugal force vector |
| $\boldsymbol{F}_{\text{ext}}$ | is the external force vector |

Rotational speed dependent matrix $\mathbf{G}$ and vector $\boldsymbol{F}_\Omega$ are formed using reference speed of 1.0 rad/s. The pre-stress effect caused by any external forces can be included into eigenvalue problem by utilizing an additional stiffness matrix, the stress-stiffening matrix $\mathbf{K}_G$, introduced in Equation (2.36).

### 2.1.1 Introduction to three-dimensional elements

Certain finite elements that are useful for rotor dynamics analysis are introduced in this subsection. For simplicity, only linear elements are presented. Typical three-dimensional solid elements are shown in Figure 2.2. The most common 3D solids used are the tetrahedron and hexahedron. Tetrahedron is a general-purpose element that can be used to mesh any 3D geometry. It is extremely useful for volumetric geometries with circular shapes that are very common in the field of rotor dynamics. Tetrahedron is also the choice when mesh biasing, a relatively great change in element size over the 3D geometry, is required. Typical mesh biasing application is structural stress analysis for a body with curved surfaces.
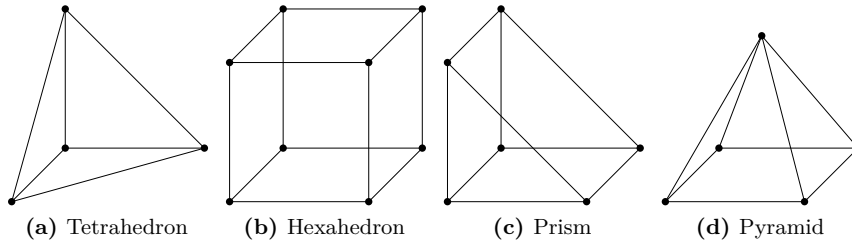
**(a)** Tetrahedron     **(b)** Hexahedron     **(c)** Prism     **(d)** Pyramid

**Figure 2.2.** Linear three-dimensional finite elements

The only drawback for this element is its difficulty to describe volume efficiently; therefore, a great number of tetrahedron elements are typically required. [60, 103]

Hexahedron element is very efficient for describing volumes, when the 3D body is prismatic, meaning there are no relative small curved surfaces nor any need for significant mesh biasing. These requirements limit the use of this element in rotor dynamics-analysis. It is nevertheless still possible to mesh certain types of rotors, at least partially, using a hexahedron. In this case the quadratic (or higher order) hexahedron element can be utilized. Higher than first order elements can be used to describe curved surfaces. Considering the finite element theory for solids, this is allowed, although the use of elements with curved surfaces should be limited, since the element quality suffers [60]. For this reason, a mesh generator typically uses the curved surface only at the geometry outer boundary if needed, and the internal elements are mesh as straight surfaces. The element quality is assessed normally during the mesh generation. The geometric shape of an element is evaluated using parameters such as aspect ratio and warping [4].

Other less used 3D elements are the prism or wedge and pyramid. Both are a combination of triangular and rectangular surfaces. The wedge element is, in certain cases, useful for the rotor dynamic application. When the element is rotated ideally, it has a triangle surfaces in axial direction, thus making it useful for meshing shaft like circular surfaced geometries. The pyramid element is probably the least used 3D element. Typically, it is required only if hexahedrons are improperly used for mesh they do not fit well. Regardless of the pros and cons of different elements, all of these elements can be used for mixed mesh: meaning that they can be used simultaneously for meshing a single solid body.

Two-dimensional elements are presented in Figure 2.3. Although, these elements are two-dimensional in nature, implementations of three-dimensional use, as discussed in the end of this subsection, exist. There is a similar analogy between 3D tetrahedron and 2D triangle elements as between 3D hexahedron and 2D quadrilateral elements. Therefore, there is no need to repeat the same introductions given with the 3D solid elements. Instead, the different options of how to use the 2D elements are discussed here. The most simple application is the 2D plane with thin or thick representation. This kind of element has only translational nodal degrees of freedom in the 2D plane. It is very efficient for plane finite element problems compared to the use of 3D solid elements, but limited to applications

that have constant thickness, such as plate geometries. A comparison of the nodal degrees of freedom of different elements is provided in Table 2.1, where $u$ represents translational degree of freedom and $\theta$ represents rotational degree of freedom.
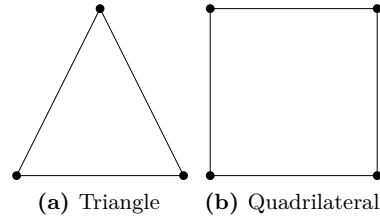


(a) Triangle    (b) Quadrilateral

**Figure 2.3.** Linear two-dimensional finite elements

**Table 2.1.** Nodal degrees of freedom of certain elements

| Element type | Nodal degrees of freedom |
|---|---|
| 3D solid | $\{u_x \quad u_y \quad u_z\}$ |
| 2D plane | $\{u_x \quad u_y\}$ |
| Axisymmetric solid | $\{u_r \quad u_w\}$ or $\{u_r \quad u_w \quad \theta\}$ |
| 3D shell | $\{u_x \quad u_y \quad u_z \quad \theta_x \quad \theta_y \quad \theta_z\}$ |
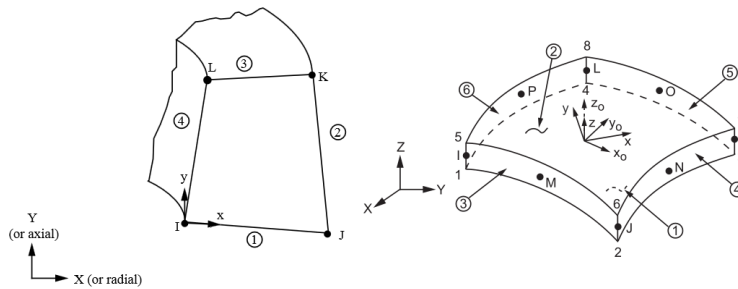


**Figure 2.4.** Applications for 2D elements: on the left, the axisymmetric element, and on the right, the 3D shell element [4]

Axisymmetric solids are one practical application for considering rotor dynamics purposes. The axisymmetric model is very efficient compared to the 3D representation of rotor geometry. The downside of the axisymmetric element is its deficiency with respect to the description of any complex shapes. The axisymmetric and 3D shell elements are illustrated in Figure 2.4.

As seen in Figure 2.4, the 3D shell elements can describe 3D surfaces. 3D shell elements may not be useful for modeling rotor components themselves, perhaps, for some features such as turbine blades. But they can be very useful for modeling the frame of the rotating machine. In comparison, 3D elements typically requires

at least two element layers, even with quadratic elements, in order to to accurately model 3D walls.

There are even more uses for a 2D element when the structure is modeled using 3D solids. Surface loads such as structural pressure load and convective or radiating heat transfer loads require integration over the loading surface; thus, 2D elements are used for surface loads. Also, certain FE-software use 3D shells for contact detection in the 3D domain. Common isoparametric 2D and 3D elements are introduced in Appendix B. The shape functions formulated for these isoparametric elements as introduced are given in Appendix A and numerical integration schemes for isoparametric elements are given in Appendix C.

### 2.1.2 Energy principle for formulating element matrices

Finite element matrices can be formulated using the energy principle, and dividing it further into kinetic and elastic strain energies. Hamilton's principle is introduced in references such as Liu and Quek [60], and Lagrangian principle in Kirchgäßner [48]. The outcome of full formulation is the equations of motion. The basic formulations required for mass, gyroscopic and stiffness matrices and fundamental force vectors are presented here.

The kinetic energy of translational motion and kinetic energy, due to the gyroscopic effect can be written as follows [60, 35]:

$$T_k = T_m + T_g \tag{2.3}$$

where $T_m$ is the kinetic energy of translational motion and $T_G$ is the kinetic energy due to the gyroscopic effect. Based on $T_m$ and $T_G$ expressions, element mass and gyroscopic damping matrices can be formulated, respectively. The kinetic energy of translational motion can be written as follows:

$$T_m = \frac{1}{2} \int_V \rho \dot{\boldsymbol{u}}^\mathrm{T} \dot{\boldsymbol{u}} dV \tag{2.4}$$

where $\rho$ is the material density. Three-dimensional displacement interpolation using shape functions can be written as follows [103]:

$$\boldsymbol{u} = \mathbf{N} \boldsymbol{d}_e = \sum_{i=1}^{n} \mathbf{N}_i \boldsymbol{d}_i \tag{2.5}$$

The element displacement vector can be written as follows [60]:

$$\boldsymbol{u} = \begin{bmatrix} u \\ v \\ w \end{bmatrix} \tag{2.6}$$

The nodal displacement vector can be written as follows:

$$\boldsymbol{d}_i = \begin{bmatrix} u_i \\ v_i \\ w_i \end{bmatrix} \tag{2.7}$$

When substituting Equation (2.5) in Equation (2.4), the kinetic energy of translational motion can be written as follows:

$$T_m = \frac{1}{2}\dot{\boldsymbol{d}}_e^{\mathrm{T}} \left( \int_V \rho \mathbf{N}^{\mathrm{T}} \mathbf{N} dV \right) \dot{\boldsymbol{d}}_e \tag{2.8}$$

Based on Equation (2.8), symmetric element mass matrix can be written as follows:

$$\mathbf{M}^e = \int_V \rho \mathbf{N}^{\mathrm{T}} \mathbf{N} dV \tag{2.9}$$

Element shape function matrix $\mathbf{N}$ can be written as follows:

$$\mathbf{N} = \begin{bmatrix} \mathbf{N}_1 & \mathbf{N}_2 & \cdots & \mathbf{N}_n \end{bmatrix} \tag{2.10}$$

where $n$ is the number of element shape functions. Element shape function matrix of node $i$ $\mathbf{N}_i$ can be written as follows:

$$\mathbf{N}_i = \begin{bmatrix} N_i & 0 & 0 \\ 0 & N_i & 0 \\ 0 & 0 & N_i \end{bmatrix} \tag{2.11}$$

where $N_i$ is the $i$th shape function of an element. Shape functions for common 3D solid elements are introduced in Appendix B. Considering the rotation around the global $X$-axis, general kinetic energy due to the gyroscopic effect, adopted from [35, 101], can be written as follows:

$$T_g = -\int_V \rho \dot{\theta}_x u \left( \dot{\theta}_y y + \dot{\theta}_z z \right) dV \tag{2.12}$$

where

$$\theta_x = \Omega t \tag{2.13}$$

$$\theta_y = \frac{1}{2} \left( \frac{\partial u}{\partial z} - \frac{\partial w}{\partial x} \right) \tag{2.14}$$

$$\theta_z = \frac{1}{2} \left( \frac{\partial v}{\partial x} - \frac{\partial u}{\partial y} \right) \tag{2.15}$$

By substituting Equations (2.13–2.15) into Equation (2.12) and replacing displacements with shape functions and generalized coordinates according to Equation (2.5), kinetic energy due to the gyroscopic effect for solid elements can be written as follows:

$$
\begin{aligned}
T_g = \Omega \sum_{i=1}^{n} \sum_{j=1}^{n} & \left( \dot{u}_i \left( \frac{1}{2} \rho \int_V \left( \frac{\partial N_i}{\partial y} N_j z_i - \frac{\partial N_i}{\partial z} N_j y_i \right) dV \right) u_j \right. \\
& \left. + \dot{v}_i \left( -\frac{1}{2} \rho \int_V \frac{\partial N_i}{\partial x} N_j z_i dV \right) u_j + \dot{w}_i \left( \frac{1}{2} \rho \int_V \frac{\partial N_i}{\partial x} N_j y_i dV \right) u_j \right)
\end{aligned}
\tag{2.16}
$$

Equation (2.16) can be written in matrix form, as follows:

$$
T_g = \Omega \sum_{i=1}^{n} \left( \dot{\boldsymbol{d}}_{e,i}^{\mathrm{T}} \frac{1}{2} \rho \int_V \begin{bmatrix} \dfrac{\partial N_i}{\partial y} z_i - \dfrac{\partial N_i}{\partial z} y_i & 0 & 0 \\[2mm] -\dfrac{\partial N_i}{\partial x} z_i & 0 & 0 \\[2mm] \dfrac{\partial N_i}{\partial x} y_i & 0 & 0 \end{bmatrix} \mathbf{N} dV \right) \boldsymbol{d}_e = \Omega \dot{\boldsymbol{d}}_e^{\mathrm{T}} \overline{\mathbf{G}}^e \boldsymbol{d}_e \tag{2.17}
$$

Based on Equation (2.17), the skew-symmetric element gyroscopic damping matrix can be written as follows [101]:

$$
\mathbf{G}^e = \overline{\mathbf{G}}^e - \overline{\mathbf{G}}^{e\mathrm{T}} \tag{2.18}
$$

Based on the strain energy expression, the element elastic stiffness matrix can be formulated. The strain energy can be written as follows [60]:

$$
\Pi = \frac{1}{2} \int_V \boldsymbol{\epsilon}^{\mathrm{T}} \boldsymbol{\sigma} dV \tag{2.19}
$$

The element strain vector can be written as follows:

$$
\boldsymbol{\epsilon} = \mathbf{L} \boldsymbol{u} \tag{2.20}
$$

Strain-displacement relationships for linear isotropic material in 3D domain can be written as follows [61]:

$$\epsilon_x = \frac{\partial u}{\partial x}$$

$$\epsilon_y = \frac{\partial v}{\partial y}$$

$$\epsilon_z = \frac{\partial w}{\partial z}$$

$$\gamma_{xy} = \frac{\partial u}{\partial y} + \frac{\partial v}{\partial x} = \gamma_{yx} \tag{2.21}$$

$$\gamma_{yz} = \frac{\partial v}{\partial z} + \frac{\partial w}{\partial y} = \gamma_{zy}$$

$$\gamma_{zx} = \frac{\partial w}{\partial x} + \frac{\partial u}{\partial z} = \gamma_{xz}$$

The matrix of partial differential operations can be written as follows [61]:

$$\mathbf{L} = \begin{bmatrix} \partial/\partial x & 0 & 0 \\ 0 & \partial/\partial y & 0 \\ 0 & 0 & \partial/\partial z \\ \partial/\partial y & \partial/\partial x & 0 \\ 0 & \partial/\partial z & \partial/\partial y \\ \partial/\partial z & 0 & \partial/\partial x \end{bmatrix} \tag{2.22}$$

The element stress vector can be written as follows:

$$\boldsymbol{\sigma} = \mathbf{D}\boldsymbol{\epsilon} \tag{2.23}$$

The matrix of material constants $\mathbf{D}$ for linear isotropic material is expressed as

$$\mathbf{D} = \frac{E}{(1+\nu)(1-2\nu)} \begin{bmatrix} 1-\nu & \nu & \nu & 0 & 0 & 0 \\ \nu & 1-\nu & \nu & 0 & 0 & 0 \\ \nu & \nu & 1-\nu & 0 & 0 & 0 \\ 0 & 0 & 0 & \frac{1-2\nu}{2} & 0 & 0 \\ 0 & 0 & 0 & 0 & \frac{1-2\nu}{2} & 0 \\ 0 & 0 & 0 & 0 & 0 & \frac{1-2\nu}{2} \end{bmatrix} \tag{2.24}$$

where $E$ is the elastic modulus and $\nu$ is the Poisson's ratio [61]. The element strain matrix $\mathbf{B}$ can be written as follows:

$$\mathbf{B} = \mathbf{L}\mathbf{N} \tag{2.25}$$

By substituting Equations (2.20), (2.23) and (2.25) in Equation (2.19), the strain energy can be written as follows:

$$\Pi = \frac{1}{2}\boldsymbol{d}_e^{\mathrm{T}} \left( \int_V \mathbf{B}^{\mathrm{T}}\mathbf{D}\mathbf{B}dV \right) \boldsymbol{d}_e \tag{2.26}$$

Symmetric element elastic stiffness matrix can be written as follows

$$\mathbf{K}_e^e = \int_V \mathbf{B}^\mathrm{T}\mathbf{D}\mathbf{B}dV \tag{2.27}$$

Elastic damping matrix using proportional damping expression based on stiffness and mass matrices can be written as follows [3]:

$$\mathbf{C}_e = \alpha_p\mathbf{K}_e + \beta_p\mathbf{M} \tag{2.28}$$

where $\alpha_p$ and $\beta_p$ are proportional coefficients for stiffness and mass matrices.

**Formulation of external force vectors**

Element body and surface force vectors can be formulated from virtual work principle. Work done by external forces can be written as follows [60]:

$$W_f = \int_V \boldsymbol{u}^\mathrm{T}\boldsymbol{f}_b^e dV + \int_S \boldsymbol{u}^\mathrm{T}\boldsymbol{f}_s^e dS \tag{2.29}$$

By substituting Equation (2.5) into Equation (2.29) the work done by external force can be written as follows:

$$W_f = \boldsymbol{d}_e^\mathrm{T}\left(\int_V \mathbf{N}^\mathrm{T}\boldsymbol{f}_b^e dV\right) + \boldsymbol{d}_e^\mathrm{T}\left(\int_S \mathbf{N}^\mathrm{T}\boldsymbol{f}_s^e dS\right) \tag{2.30}$$

The element nodal body force vector can be written as follows:

$$\boldsymbol{f}_b^e = \begin{bmatrix} f_x \\ f_y \\ f_z \end{bmatrix} \tag{2.31}$$

The element nodal surface force vector can be written as follows:

$$\boldsymbol{f}_s^e = \begin{bmatrix} f_x \\ f_y \\ f_z \end{bmatrix} \tag{2.32}$$

The nodal surface force vector is having same analogy than in Equation (2.31). Element body force vector can be written as follows:

$$\boldsymbol{F}_b^e = \int_V \mathbf{N}^\mathrm{T}\boldsymbol{f}_b^e dV \tag{2.33}$$

Element surface force vector can be written as follows:

$$\boldsymbol{F}_s^e = \int_S \mathbf{N}^\mathrm{T} \boldsymbol{f}_s^e dS \tag{2.34}$$

Total work done by external force is thus given as

$$W_f = \boldsymbol{d}_e^\mathrm{T} \boldsymbol{F}_b^e + \boldsymbol{d}_e^\mathrm{T} \boldsymbol{F}_s^e = \boldsymbol{d}_e^\mathrm{T} \boldsymbol{F}_{\mathrm{ext}}^e \tag{2.35}$$

where $\boldsymbol{F}_{\mathrm{ext}}^e$ is the element total external force vector.

**Stress-stiffening effect**

The stress stiffness matrix can be used for eigenvalue analysis of the pre-stressed structure. Stress stiffening – also known as geometric stiffening – for a single element can be written as follows [48]:

$$\mathbf{K}_G^e = \int_V \mathbf{B}_\epsilon^\mathrm{T} \mathbf{S}_0 \mathbf{B}_\epsilon dV \tag{2.36}$$

The matrix $\mathbf{B}_\epsilon$ containing the spatial derivatives of the element shape functions can be written as follows:

$$\mathbf{B}_\epsilon = \begin{bmatrix} \mathbf{I}_3 \dfrac{\partial N_1}{\partial x} & \mathbf{I}_3 \dfrac{\partial N_2}{\partial x} & \cdots & \mathbf{I}_3 \dfrac{\partial N_n}{\partial x} \\ \mathbf{I}_3 \dfrac{\partial N_1}{\partial y} & \mathbf{I}_3 \dfrac{\partial N_2}{\partial y} & \cdots & \mathbf{I}_3 \dfrac{\partial N_n}{\partial y} \\ \mathbf{I}_3 \dfrac{\partial N_1}{\partial z} & \mathbf{I}_3 \dfrac{\partial N_2}{\partial z} & \cdots & \mathbf{I}_3 \dfrac{\partial N_n}{\partial z} \end{bmatrix} \tag{2.37}$$

and the initial stress matrix $\mathbf{S}_0$ is

$$\mathbf{S}_0 = \begin{bmatrix} \mathbf{I}_3 \sigma_x & \mathbf{I}_3 \tau_{xy} & \mathbf{I}_3 \tau_{xz} \\ \mathbf{I}_3 \tau_{yx} & \mathbf{I}_3 \sigma_y & \mathbf{I}_3 \tau_{yz} \\ \mathbf{I}_3 \tau_{zx} & \mathbf{I}_3 \tau_{zy} & \mathbf{I}_3 \sigma_z \end{bmatrix} \tag{2.38}$$

where $\mathbf{I}_3$ is a $3 \times 3$ identity matrix. The element stress vector can be written as follows [61]

$$\begin{Bmatrix} \sigma_x & \sigma_y & \sigma_z & \tau_{xy} & \tau_{yz} & \tau_{zx} \end{Bmatrix}^\mathrm{T} = \mathbf{D}\mathbf{B}\boldsymbol{u} \tag{2.39}$$

where $\{\sigma_x \quad \sigma_y \quad \sigma_z\}$ are the element normal stress components and $\{\tau_{xy} \quad \tau_{yz} \quad \tau_{zx}\}$ are the element shear stress components. Element-based normal stress and shear stress components are illustrated in Figure 2.5. Note that for linear isotropic material, the strain components are equal in the following manner

$$\tau_{xy} = \tau_{yx}$$
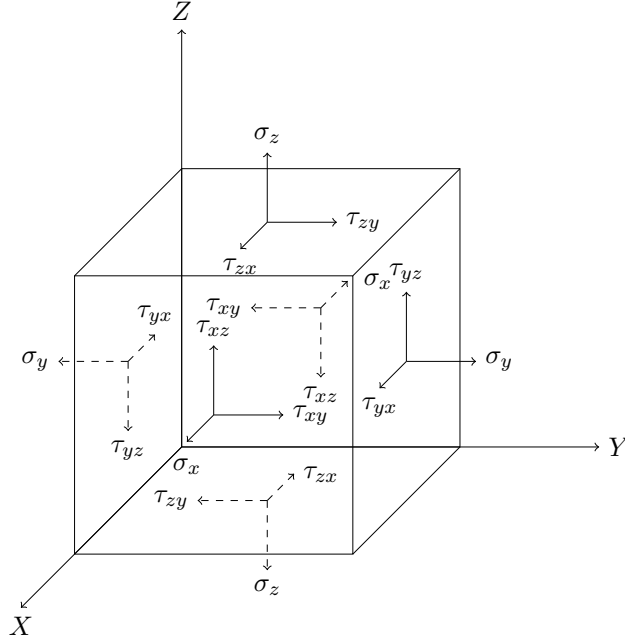$$\tau_{yz} = \tau_{zy} \qquad (2.40)$$
$$\tau_{zx} = \tau_{xz}$$



**Figure 2.5.** Three-dimensional stress components

**Common force vectors for structural analysis**

Formulations of 3D solid element force vectors for centrifugal force, translational acceleration, surface pressure and thermal expansion are presented. The element centrifugal force vector can be written as follows [48]:

$$\Omega^2 \boldsymbol{F}_\Omega^e = \Omega^2 \sum_{i=1}^{n} \rho \int_V \mathbf{N}_i^{\mathrm{T}} \boldsymbol{\Omega}^{\mathrm{T}} \boldsymbol{\Omega} \boldsymbol{x}_i dV \qquad (2.41)$$

where $\boldsymbol{x}_i$ is the vector of coordinates of node $i$. The matrix $\boldsymbol{\Omega}$ indicating the axis of rotation can be written as follows:

$$\boldsymbol{\Omega} = \begin{bmatrix} 0 & -\omega_z & \omega_y \\ \omega_z & 0 & -\omega_x \\ -\omega_y & \omega_x & 0 \end{bmatrix} \qquad (2.42)$$

where $\omega_x$, $\omega_y$ and $\omega_z$ are the normalized angular velocity components, according to the global coordinate system, $|\{\omega_x \quad \omega_y \quad \omega_z\}| = 1$. Based on Newton's second law, the general element translational acceleration force vector can be written as follows:

$$\boldsymbol{F}_g^e = \rho \int_V \mathbf{N}^{\mathrm{T}} \boldsymbol{g}_a dV \tag{2.43}$$

where

$$\boldsymbol{g}_a = \begin{bmatrix} g_x \\ g_y \\ g_z \end{bmatrix} \tag{2.44}$$

where $g_x$, $g_y$ and $g_z$ are the translational acceleration components, according to the Cartesian coordinate system. By applying the standard acceleration of gravity into Equation (2.44), the gravitational body force can be modeled. Element pressure force vector can be written as follows:

$$\boldsymbol{F}_p^e = \int_S \mathbf{N}^{\mathrm{T}} \boldsymbol{p}_p dS \tag{2.45}$$

where

$$\boldsymbol{p}_p = \begin{bmatrix} p_x \\ p_y \\ p_z \end{bmatrix} \tag{2.46}$$

where $p_x$, $p_y$ and $p_z$ are the pressure normal component according to the Cartesian coordinate system. The element force vector due to initial strain can be written as follows [103]:

$$\boldsymbol{F}_\epsilon^e = \int_V \mathbf{B}^{\mathrm{T}} \mathbf{D} \boldsymbol{\epsilon}_0 dV \tag{2.47}$$

where

$$\boldsymbol{\epsilon}_0 = \begin{bmatrix} \epsilon_{x,0} \\ \epsilon_{y,0} \\ \epsilon_{z,0} \\ \gamma_{xy,0} \\ \gamma_{yz,0} \\ \gamma_{zx,0} \end{bmatrix} \tag{2.48}$$

The linear thermal expansion can be written as follows:

$$\Delta L = L\alpha \left( T - T_{\mathrm{ref}} \right) \tag{2.49}$$

Thus, strain $\epsilon$ can be written as follows:

$$\epsilon = \frac{\Delta L}{L} = \alpha \Delta T \tag{2.50}$$

where $\alpha$ is the thermal expansion coefficient. The nodal temperature can be non-uniform over the element. Thus, by expanding the Equation (2.50) into three-dimensional domain and substituting it into Equation (2.47), the element thermal expansion force vector can be written as follows [28]:

$$\boldsymbol{F}_{\Delta T}^e = \sum_{i=1}^n \int_V \mathbf{B}_i^\mathrm{T} \mathbf{D} \boldsymbol{\alpha} \Delta T_i dV \tag{2.51}$$

where $\Delta T_i$ is the temperature difference of node $i$. The vector $\boldsymbol{\alpha}$ can be written as follows:

$$\boldsymbol{\alpha} = \begin{bmatrix} \alpha_x \\ \alpha_y \\ \alpha_z \\ 0 \\ 0 \\ 0 \end{bmatrix} \tag{2.52}$$

### 2.1.3 Heat transfer theory

The heat transfer equation is introduced in this subsection. Heat transfer analysis can be coupled with structural analysis if a structure is experiencing thermal loads such as internal heat generation or boundary heat flow from solid into medium. In this case, the need for solving the thermal state of a structure becomes necessary for analyzing the effect of thermal expansion-induced stresses. The heat transfer equation can be written as follows [76]:

$$-\left(\frac{\partial q_x}{\partial x} + \frac{\partial q_y}{\partial y} + \frac{\partial q_z}{\partial z}\right) + Q = \rho c \frac{\partial T}{\partial t} \tag{2.53}$$

where $q_x$, $q_y$ and $q_z$ are the components of heat flow through the unit area, $Q$ is the internal heat generation rate per unit volume, $\rho$ is the material density, $c$ is the specific heat capacity, $T$ is the temperature and $t$ is the time. The heat flow components in isotropic case can be written as follows:

$$\begin{aligned} q_x &= -k_x \frac{\partial T}{\partial x} \\ q_y &= -k_y \frac{\partial T}{\partial y} \\ q_z &= -k_z \frac{\partial T}{\partial z} \end{aligned} \tag{2.54}$$

where $k_x$, $k_y$ and $k_z$ are the thermal conductivity coefficients in global X, Y and $Z$-directions, respectively. By substituting the heat flow components in Equation (2.53), the heat transfer equation can be written as follows:

$$\frac{\partial}{\partial x}\left(k_x \frac{\partial T}{\partial x}\right) + \frac{\partial}{\partial y}\left(k_y \frac{\partial T}{\partial y}\right) + \frac{\partial}{\partial z}\left(k_z \frac{\partial T}{\partial z}\right) + Q = \rho c \frac{\partial T}{\partial t} \qquad (2.55)$$

There are four typical loading types to be used with the heat equation: the internal volumetric heat generation, boundary surface heat flow according to Equation (2.56), boundary surface convection heat transfer according to Equation (2.57), and heat radiation, which is excluded from the heat equation. In addition, a fixed temperature on surface or on a single node can be used as the boundary condition.

$$q_x n_x + q_y n_y + q_z n_z = -q_s \qquad (2.56)$$

$$q_x n_x + q_y n_y + q_z n_z = h\left(T_s - T_e\right) \qquad (2.57)$$

where $h$ is the convection coefficient, $T_s$ is the surface temperature and $T_e$ is the reference temperature for convective heat transfer. This reference temperature is normally the ambient temperature of the fluid on the boundary surface of a structural domain.

### 2.1.4   Finite element method for three-dimensional heat transfer

In this subsection, thermal modeling using the 3D solid finite element method is introduced. Formulation of heat transfer matrices and loading vectors are given. Using the Galerkin method, the heat transfer equation can be written as follows [76]:

$$\int_V \left(\frac{\partial q_x}{\partial x} + \frac{\partial q_y}{\partial y} + \frac{\partial q_z}{\partial z} - Q + \rho c \frac{\partial T}{\partial t}\right) N_i dV = 0 \qquad (2.58)$$

$$\begin{aligned}
&\int_V \rho c \frac{\partial T}{\partial t} N_i dV - \int_V \left[\frac{\partial N_i}{\partial x} \quad \frac{\partial N_i}{\partial y} \quad \frac{\partial N_i}{\partial z}\right] \boldsymbol{q} dV \\
&= \int_V Q N_i dV - \int_S \boldsymbol{q}^{\mathrm{T}} \boldsymbol{n} N_i dS \\
&+ \int_S q_s N_i dS - \int_S h\left(T_s - T_e\right) N_i dS
\end{aligned} \qquad (2.59)$$

where

$$\begin{aligned}
\boldsymbol{q}^{\mathrm{T}} &= \begin{bmatrix} q_x & q_y & q_z \end{bmatrix} \\
\boldsymbol{n}^{\mathrm{T}} &= \begin{bmatrix} n_x & n_y & n_z \end{bmatrix}
\end{aligned} \qquad (2.60)$$

where $\boldsymbol{n}$ is an outer normal to the surface of the body. The finite element equation for heat transfer can be written as follows:

$$\mathbf{C}\dot{\boldsymbol{T}}_N + (\mathbf{K}_C + \mathbf{K}_h)\,\boldsymbol{T}_N = \boldsymbol{R}_T + \boldsymbol{R}_Q + \boldsymbol{R}_q + \boldsymbol{R}_h \qquad (2.61)$$

where

| | |
|---|---|
| $\mathbf{C}$ | is the heat capacity matrix |
| $\mathbf{K}_C$ | is the heat conduction matrix |
| $\mathbf{K}_h$ | is the surface convection matrix |
| $\boldsymbol{T}_N$ | is the nodal temperature vector |
| $\boldsymbol{R}_T$ | is the specified boundary temperature vector |
| $\boldsymbol{R}_Q$ | is the internal heat generation vector |
| $\boldsymbol{R}_q$ | is the boundary heat flow vector |
| $\boldsymbol{R}_h$ | is the surface convection vector |

The element heat capacity matrix can be written as follows:

$$\mathbf{C}^e = \int_V \rho c \boldsymbol{N}^{\mathrm{T}} \boldsymbol{N} dV \qquad (2.62)$$

where the vector of element shape functions $\boldsymbol{N}$ can be written as follows [24]:

$$\boldsymbol{N} = \begin{bmatrix} N_1 & N_2 & \cdots & N_n \end{bmatrix} \qquad (2.63)$$

The element heat conduction matrix can be written as follows [76]:

$$\mathbf{K}_C^e = \int_V \mathbf{B}_d^{\mathrm{T}} \mathbf{D}_c \mathbf{B}_d dV \qquad (2.64)$$

where $\mathbf{B}_d$ is the matrix of shape function derivatives and $\mathbf{D}_c$ the conductivity matrix. The matrix of shape function derivatives can be written as follows:

$$\mathbf{B}_d = \begin{bmatrix} \partial/\partial x \\ \partial/\partial y \\ \partial/\partial z \end{bmatrix} \boldsymbol{N} \qquad (2.65)$$

The conductivity matrix can be written as follows [24]:

$$\mathbf{D}_c = \begin{bmatrix} k_x & 0 & 0 \\ 0 & k_y & 0 \\ 0 & 0 & k_z \end{bmatrix} \qquad (2.66)$$

The element surface convection matrix can be written as follows:

$$\mathbf{K}_h^e = \int_S h \boldsymbol{N}^{\mathrm{T}} \boldsymbol{N} dS \qquad (2.67)$$

The element specified boundary temperature vector can be written as follows:

$$\boldsymbol{R}_T^e = -\int_S \boldsymbol{q}^{\mathrm{T}} \boldsymbol{n} \boldsymbol{N}^{\mathrm{T}} dS \tag{2.68}$$

The element internal heat generation vector can be written as follows:

$$\boldsymbol{R}_Q^e = \int_V Q \boldsymbol{N}^{\mathrm{T}} dV \tag{2.69}$$

The element boundary heat flow vector can be written as follows:

$$\boldsymbol{R}_q^e = \int_S q_s \boldsymbol{N}^{\mathrm{T}} dS \tag{2.70}$$

The element surface convection vector can be written as follows:

$$\boldsymbol{R}_h^e = \int_S h T_e \boldsymbol{N}^{\mathrm{T}} dS \tag{2.71}$$

## 2.2   Constraint equations and contact modeling

In this subsection, the concept constraint equation is introduced, and multiple different methods of applying constrain equations are presented. Constraint equation is an equation which describes the motion between two or more degrees of freedom. Boundary condition, such as a DOF displacement, can be defined by applying the constraint equation to a boundary DOF in the model. In such a case, the constraint equation is applied between a particular boundary DOF and the ground; thus, it is referred to as boundary constraint. Similarly, boundary constraints such as cyclic symmetry can be described. Four different constraint modeling methods are introduced: master-slave, penalty function, Lagrangian multiplier method [29, 102, 103, 104], and a novel proposed application specific constraint method called trial force method developed in [91]. Constraint equations are implemented inside the stiffness matrix, and they limit the movement of unconstrained DOFs. Two main types of constraint equations are considered: homogeneous equations that constraints the DOF movement, and non-homogeneous equations that describe how a single DOF can move in accordance with one or more DOFs. In Figure 2.6, the procedure of using constraint equations is presented.

Master-slave and penalty function methods both use direct stiffness matrix manipulation, which yields the desired displacement vector output, but not the force vector corresponding to the constrained structure. Direct manipulation in this instance considers the manipulation of stiffness terms to be directly related to the DOFs of a particular constraint equation. Both the Lagrangian multiplier and trial force method do not use direct stiffness matrix manipulation, which yields the desired displacement vector output and the force vector corresponding

to the constrained structure. Instead, both methods employ indirect stiffness matrix manipulation. Lagrangian multiplier method extends the stiffness matrix by adding a bordered stiffness matrix part. In the trial force method, the boundary conditions are manipulated by adding constraints to the model boundary.
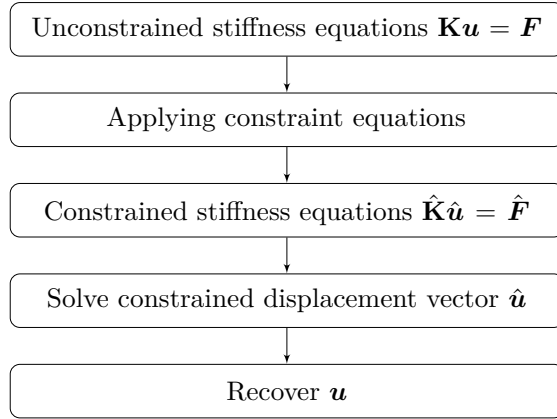
Unconstrained stiffness equations $\mathbf{K}\boldsymbol{u} = \boldsymbol{F}$

Applying constraint equations

Constrained stiffness equations $\mathbf{\hat{K}}\boldsymbol{\hat{u}} = \boldsymbol{\hat{F}}$

Solve constrained displacement vector $\boldsymbol{\hat{u}}$

Recover $\boldsymbol{u}$

**Figure 2.6.** Scheme for applying constraint equations

In this section, a one-dimensional structure with five degrees of freedom shown in Figure 2.7 is used as an example. The stiffness equation for the structure in question can be written as follows:
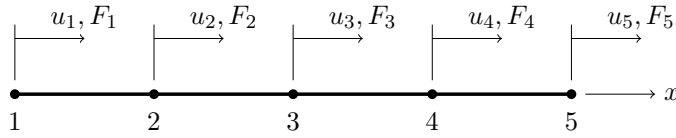


**Figure 2.7.** One-dimensional structure discretized to four bar elements

$$\mathbf{K}\boldsymbol{u} = \boldsymbol{F} \tag{2.72}$$

which in expanded form can be written as follows:

$$\begin{bmatrix} k_{11} & k_{12} & 0 & 0 & 0 \\ k_{21} & k_{22} & k_{23} & 0 & 0 \\ 0 & k_{32} & k_{33} & k_{34} & 0 \\ 0 & 0 & k_{43} & k_{44} & k_{45} \\ 0 & 0 & 0 & k_{54} & k_{55} \end{bmatrix} \begin{bmatrix} u_1 \\ u_2 \\ u_3 \\ u_4 \\ u_5 \end{bmatrix} = \begin{bmatrix} F_1 \\ F_2 \\ F_3 \\ F_4 \\ F_5 \end{bmatrix} \tag{2.73}$$

### 2.2.1 Master-slave method

The master-slave constraint method, also known as the multipoint constraint (MPC) method, is considered the simplest constraint method to be used for

presenting the use of the homogeneous constraint equation. [29] Let us apply a constraint to the structure given in Figure 2.7 between DOFs $u_2$ and $u_4$ as follows:

$$u_2 = u_4 \tag{2.74}$$

Based on Equation (2.74), let us propose that DOF $u_4$ is a slave of DOF $u_2$, thus $u_4$ has to move exactly the same quantity than DOF $u_2$. Let us introduce a transformation matrix $\mathbf{T}$ to apply the constraint equation given in Equation (2.74) as follows:

$$\begin{bmatrix} u_1 \\ u_2 \\ u_3 \\ u_4 \\ u_5 \end{bmatrix} = \begin{bmatrix} 1 & 0 & 0 & 0 \\ 0 & 1 & 0 & 0 \\ 0 & 0 & 1 & 0 \\ 0 & 1 & 0 & 0 \\ 0 & 0 & 0 & 1 \end{bmatrix} \begin{bmatrix} u_1 \\ u_2 \\ u_3 \\ u_5 \end{bmatrix} \tag{2.75}$$

where the transformation matrix $\mathbf{T}$ is originally a square identity matrix size of $n \times n$, where $n$ is the number of DOFs. In the transformation matrix $\mathbf{T}$, the row of the slave DOF is replaced with the row of the master DOF, and the column of the slave DOF is removed. Using matrix notation, the described transformations of matrix $\mathbf{T}$ can be written as follows:

$$\begin{aligned} \mathbf{T} &= \mathbf{I}_{n \times n} \\ \boldsymbol{T}_k &= \boldsymbol{T}_i \\ \boldsymbol{T}_j &= \emptyset, \quad i = j \end{aligned} \tag{2.76}$$

where subscripts $n$, $i$, $k$ and $j$ are the number of DOFs, $i$th row corresponding to the master DOF, $k$th row corresponding to the slave DOF and $j$th column corresponding to the master DOF, respectively, and $\emptyset$ is the symbol for the empty set representing an empty column vector. This method can be impractical for handling multiple constraints. Thus, an alternative method for manipulating the transformation matrix $\mathbf{T}$ and introduction of diagonal matrix $\mathbf{T}_d$ can be written as follows:

$$\begin{aligned} \mathbf{T} &= \mathbf{I}_{n \times n} \\ \boldsymbol{T}_k &= \boldsymbol{T}_i \\ \mathbf{T}_d &= \mathbf{0}_{n \times n} \\ T_{d,ij} &= 1, \quad i = j \end{aligned} \tag{2.77}$$

where subscripts $n$, $i$ and $k$ are the number of DOFs, $i$th row corresponding to the master DOF and $k$th row corresponding to the slave DOF and $\mathbf{T}_d$ is the transformation matrix containing diagonal terms. This method keeps the original DOF order and thus is practical to be used for a problem having multiple constraints. Although, some numerical solvers of software such as Matlab may lack the capability to skipping empty rows and column, and thus requires

additional diagonal markings, therefore the diagonal matrix $\mathbf{T}_d$ according to Equation (2.77) is required. In Equation (2.80), the use of the $\mathbf{T}_d$ matrix is introduced. Equation (2.75) can be written as follows:

$$\boldsymbol{u} = \mathbf{T}\hat{\boldsymbol{u}} \tag{2.78}$$

By replacing Equation (2.75) into (2.72) and multiplying by $\mathbf{T}^{\mathrm{T}}$ yields modified stiffness equations as follows:

$$\hat{\mathbf{K}}\hat{\boldsymbol{u}} = \hat{\boldsymbol{F}} \tag{2.79}$$

When using the alternative method for generating the transformation matrix as given in Equation (2.77), the modified stiffness matrix can be written as follows:

$$\hat{\mathbf{K}} = \mathbf{T}^{\mathrm{T}}\mathbf{K}\mathbf{T} + \mathbf{T}_d \tag{2.80}$$

$$\hat{\boldsymbol{F}} = \mathbf{T}^{\mathrm{T}}\boldsymbol{F} \tag{2.81}$$

By expanding Equation (2.79), the result can be written as follows:

$$\begin{bmatrix} k_{11} & k_{12} & 0 & 0 \\ k_{21} & k_{22} + k_{44} & k_{23} + k_{43} & k_{45} \\ 0 & k_{32} + k_{34} & k_{33} & 0 \\ 0 & k_{45} & 0 & k_{55} \end{bmatrix} \begin{bmatrix} u_1 \\ u_2 \\ u_3 \\ u_5 \end{bmatrix} = \begin{bmatrix} F_1 \\ F_2 + F_4 \\ F_3 \\ F_5 \end{bmatrix} \tag{2.82}$$

Recovering the slave DOFs can be performed by using Equation (2.78). A set of multiple homogeneous constraint equations can be applied. Let us introduce a second constraint equation as follows:

$$u_1 + 2u_3 = 0 \tag{2.83}$$

Again, selecting the slave DOF, now $u_3$, Equation (2.83) can be written as follows:

$$u_3 = -\frac{1}{2}u_1 \tag{2.84}$$

When applying both constraint equations (2.74) and (2.83), Equation (2.78) can be rewritten as follows:

$$\begin{bmatrix} u_1 \\ u_2 \\ u_3 \\ u_4 \\ u_5 \end{bmatrix} = \begin{bmatrix} 1 & 0 & 0 \\ 0 & 1 & 0 \\ -\frac{1}{2} & 0 & 0 \\ 0 & 1 & 0 \\ 0 & 0 & 1 \end{bmatrix} \begin{bmatrix} u_1 \\ u_2 \\ u_5 \end{bmatrix} \tag{2.85}$$

In addition to homogeneous constraint equations, there are also non-homogeneous constraint equations that yield differentiating relationship between the constraint DOFs. An example of a non-homogeneous constraint equation can be written as follows:

$$u_2 - u_4 = 2 \tag{2.86}$$

Again, DOF $u_4$ is selected as slave DOF. Non-homogeneous constraint equations can be used to model a gap or overlapping to the meshed geometry. Now, Equation (2.78) is expanded by adding a vector for non-homogeneous part of the constraint equations. Equation (2.78) can be written as follows:

$$\boldsymbol{u} = \mathbf{T}\hat{\boldsymbol{u}} + \boldsymbol{g} \tag{2.87}$$

where $\boldsymbol{g}$ is the vector of non-homogeneous coefficients. Equation (2.87) in expanded form can be written as follows:

$$\begin{bmatrix} u_1 \\ u_2 \\ u_3 \\ u_4 \\ u_5 \end{bmatrix} = \begin{bmatrix} 1 & 0 & 0 & 0 \\ 0 & 1 & 0 & 0 \\ 0 & 0 & 1 & 0 \\ 0 & 1 & 0 & 0 \\ 0 & 0 & 0 & 1 \end{bmatrix} \begin{bmatrix} u_1 \\ u_2 \\ u_3 \\ u_5 \end{bmatrix} + \begin{bmatrix} 0 \\ 0 \\ 0 \\ -2 \\ 0 \end{bmatrix} \tag{2.88}$$

By multiplying Equation (2.87) by $\mathbf{T}^{\mathrm{T}}\mathbf{K}$ and substituting Equation (2.72) into Equation (2.87) and passing all the terms to the right-hand side, the force vector can be written as follows:

$$\hat{\boldsymbol{F}} = \mathbf{T}^{\mathrm{T}} \left( \boldsymbol{F} + \mathbf{K}\boldsymbol{g} \right) \tag{2.89}$$

Equation (2.89) in expanded form can be written as follows:

$$\begin{bmatrix} k_{11} & k_{12} & 0 & 0 \\ k_{21} & k_{22} + k_{44} & k_{23} + k_{43} & k_{45} \\ 0 & k_{32} + k_{34} & k_{33} & 0 \\ 0 & k_{45} & 0 & k_{55} \end{bmatrix} \begin{bmatrix} u_1 \\ u_2 \\ u_3 \\ u_5 \end{bmatrix} = \begin{bmatrix} F_1 \\ F_2 + F_4 - 2k_{44} \\ F_3 - 2k_{34} \\ F_5 - 2k_{45} \end{bmatrix} \tag{2.90}$$

The master-slave constraint method is exact. This method reduces the total number of degrees of freedom, if so desired; it can therefore be regarded as a form of model reduction. Due to the simplicity of the master-slave constraint method, it was used here to introduce homogeneous and non-homogeneous constraint equations. The master-slave method can also be used for kinematic model reduction, when the displacements of the slave DOFs can be expressed using series kinematic constraint equations, though this is rarely useful. In other words, the method can be used only if the elastic behavior can be expressed fully kinematically: meaning the structures must be very simple.

### 2.2.2 Penalty function method

The penalty function constraint method is easier to implement than the master-slave method. This method uses a fictional, massless, penalty element. [29] This element is elastic, though very stiff, which leads to a situation that the constraint equation using the penalty method is not exact, unlike the master-slave method, owing to the elastic nature of the penalty element. The same structure introduced in Section 2.2 with a penalty element in accordance with constraint equation (2.74) is illustrated in Figure 2.8.
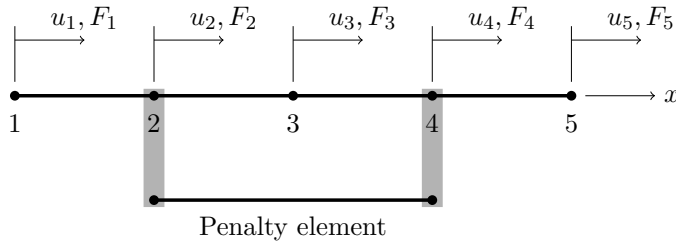


**Figure 2.8.** Five-DOF bar element model with penalty element

The local penalty element stiffness equation can be written as follows:

$$W \begin{bmatrix} 1 & -1 \\ -1 & 1 \end{bmatrix} \begin{bmatrix} u_1 \\ u_4 \end{bmatrix} = \begin{bmatrix} 0 \\ 0 \end{bmatrix} \tag{2.91}$$

where $W$ is the penalty weight or the stiffness coefficient for the penalty element. The penalty method uses full matrices, substituting Equation (2.91) in Equation (2.73) using global DOFs yields

$$\begin{bmatrix} k_{11} & k_{12} & 0 & 0 & 0 \\ k_{21} & k_{22}+W & k_{23} & -W & 0 \\ 0 & k_{32} & k_{33} & k_{34} & 0 \\ 0 & -W & k_{43} & k_{44}+W & k_{45} \\ 0 & 0 & 0 & k_{54} & k_{55} \end{bmatrix} \begin{bmatrix} u_1 \\ u_2 \\ u_3 \\ u_4 \\ u_5 \end{bmatrix} = \begin{bmatrix} F_1 \\ F_2 \\ F_3 \\ F_4 \\ F_5 \end{bmatrix} \tag{2.92}$$

Multiple DOF constraint equations can be applied using the penalty method. Let us consider a non-homogeneous constraint equation as follows:

$$u_1 + 3u_4 - 4u_5 = 1 \tag{2.93}$$

Equation (2.93) expressed in matrix form can be written as follows:

$$\begin{bmatrix} 1 & 3 & -4 \end{bmatrix} \begin{bmatrix} u_1 \\ u_4 \\ u_5 \end{bmatrix} = 1 \tag{2.94}$$

By multiplying both sides using the coefficient vector and the penalty weight, Equation (2.94) can be written as follows:

$$W \begin{bmatrix} 1 & 3 & -4 \\ 3 & 9 & -12 \\ -4 & -12 & 16 \end{bmatrix} \begin{bmatrix} u_1 \\ u_4 \\ u_5 \end{bmatrix} = W \begin{bmatrix} 1 \\ 3 \\ -4 \end{bmatrix} \tag{2.95}$$

By substituting Equation (2.95) in (2.73) using global DOFs, we get

$$\begin{bmatrix} k_{11}+W & k_{12} & 0 & 3W & -4W \\ k_{21} & k_{22} & k_{23} & 0 & 0 \\ 0 & k_{32} & k_{33} & k_{34} & 0 \\ 3W & 0 & k_{43} & k_{44}+9W & k_{45}-12W \\ -4W & 0 & 0 & k_{54}-12W & k_{55}+16W \end{bmatrix} \begin{bmatrix} u_1 \\ u_2 \\ u_3 \\ u_4 \\ u_5 \end{bmatrix} = \begin{bmatrix} F_1+W \\ F_2 \\ F_3 \\ F_4+3W \\ F_5-4W \end{bmatrix} \tag{2.96}$$

Attention must be paid when selecting the penalty weight. Since the penalty constraint using penalty element is not exact, owing to the fact that the penalty element has finite stiffness, the penalty weight selected should be as large as possible. If the penalty coefficient selected is too large, the stiffness matrix may become ill-conditioned with respect to inversion.

The constraint error of the penalty method, taking the example non-homogeneous constraint equation (2.93) into consideration, is $e_g = \mid u_1 + 3u_4 - 4u_5 - 1 \mid$. The magnitude of this constraint error $e_g$ is dependent on the penalty weight used. With sufficiently large penalty weights the constraint error becomes $1/W$.

The square root rule is provided as a general guide for selecting the penalty weight coefficient. The rules states that the penalty weight should be $W \approx 10^{k_{\max}} \sqrt{10^{p_w}}$, where $k_{\max}$ is the magnitude of the largest stiffness coefficient in the unconstrained stiffness matrix, and $p_w$ is the working precision of the software used. [29]

### 2.2.3   Lagrangian multiplier method

Unlike the penalty function method, the Lagrangian multiplier constraint method can be exact. This method uses additional coefficients, Lagrangian multipliers $\lambda$, thus increasing the size of global matrices. [29] Let us consider a constraint equation as follows:

$$u_2 = u_4 \tag{2.97}$$

The Lagrangian multiplier constraint, Equation (2.97), can be illustrated as shown in Figure 2.9, where $-\lambda, \quad \lambda$ are the constraint forces.

By applying Equation (2.97) the stiffness equation (2.73) we get
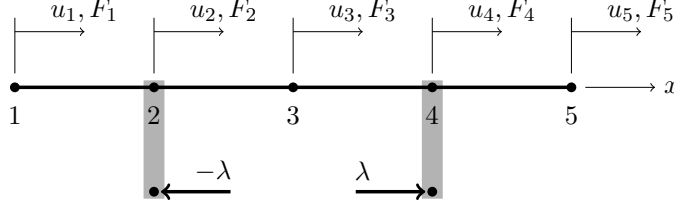
**Figure 2.9.** Five-DOF bar element model with illustration of Lagrangian multipliers

$$
\begin{bmatrix}
k_{11} & k_{12} & 0 & 0 & 0 \\
k_{21} & k_{22} & k_{23} & 0 & 0 \\
0 & k_{32} & k_{33} & k_{34} & 0 \\
0 & 0 & k_{43} & k_{44} & k_{45} \\
0 & 0 & 0 & k_{54} & k_{55}
\end{bmatrix}
\begin{bmatrix}
u_1 \\ u_2 \\ u_3 \\ u_4 \\ u_5
\end{bmatrix}
=
\begin{bmatrix}
F_1 \\ F_2 - \lambda \\ F_3 \\ F_4 + \lambda \\ F_5
\end{bmatrix}
\tag{2.98}
$$

where $\lambda$ is the Lagrangian multiplier. By moving the unknown $\lambda$ to the left-hand side, modifying the stiffness matrix by keeping it square and appending the vector of displacements, we get a multiplier-augmented system as follows:

$$
\begin{bmatrix}
k_{11} & k_{12} & 0 & 0 & 0 & 0 \\
k_{21} & k_{22} & k_{23} & 0 & 0 & 1 \\
0 & k_{32} & k_{33} & k_{34} & 0 & 0 \\
0 & 0 & k_{43} & k_{44} & k_{45} & -1 \\
0 & 0 & 0 & k_{54} & k_{55} & 0 \\
0 & 1 & 0 & -1 & 0 & 0
\end{bmatrix}
\begin{bmatrix}
u_1 \\ u_2 \\ u_3 \\ u_4 \\ u_5 \\ \lambda
\end{bmatrix}
=
\begin{bmatrix}
F_1 \\ F_2 \\ F_3 \\ F_4 \\ F_5 \\ 0
\end{bmatrix}
\tag{2.99}
$$

The symmetric, appended stiffness matrix, is called bordered stiffness matrix. Solving the Equation (2.99) will provide a solution for the constraint forces through the unknown $\lambda$. Let us consider two general constraint equations as follows:

$$
\begin{aligned}
u_2 - u_4 &= 0 \quad and \\
u_1 + 3u_4 - 4u_5 &= 1
\end{aligned}
\tag{2.100}
$$

Adding these two constraint equations to the unmodified stiffness equation (2.73) using Lagrangian multiplier method yields as follows:

$$
\begin{bmatrix}
k_{11} & k_{12} & 0 & 0 & 0 & 0 & 1 \\
k_{21} & k_{22} & k_{23} & 0 & 0 & 1 & 0 \\
0 & k_{32} & k_{33} & k_{34} & 0 & 0 & 0 \\
0 & 0 & k_{43} & k_{44} & k_{45} & -1 & 3 \\
0 & 0 & 0 & k_{54} & k_{55} & 0 & -4 \\
0 & 1 & 0 & -1 & 0 & 0 & 0 \\
1 & 0 & 0 & 3 & -4 & 0 & 0
\end{bmatrix}
\begin{bmatrix}
u_1 \\ u_2 \\ u_3 \\ u_4 \\ u_5 \\ \lambda_1 \\ \lambda_2
\end{bmatrix}
=
\begin{bmatrix}
F_1 \\ F_2 \\ F_3 \\ F_4 \\ F_5 \\ 0 \\ 1
\end{bmatrix}
\tag{2.101}
$$

The general matrix form for Lagrangian multiplier can be written as follows:

$$\begin{bmatrix} \mathbf{K} & \mathbf{A}_b^{\mathrm{T}} \\ \mathbf{A}_b & \mathbf{0} \end{bmatrix} \begin{bmatrix} \boldsymbol{u} \\ \boldsymbol{\lambda} \end{bmatrix} = \begin{bmatrix} \boldsymbol{F} \\ \boldsymbol{g} \end{bmatrix} \tag{2.102}$$

Solving Equation (2.102) will provide the vectors $\boldsymbol{u}$ and $\boldsymbol{\lambda}$. According to the Equation (2.102), the constraint forces can be calculated as $-\mathbf{A}_b^{\mathrm{T}}\boldsymbol{\lambda}$. The constraint equations can be removed if these constraint forces are applied.

### 2.2.4 Trial force method

Trial force method is a custom application specific constraint method developed for cylindrical shrink fitted joints introduced by Sikanen *et al.* [91]. This constraint equation method is one of the main contributions of this dissertation. It is formulated for use with the cylindrical coordinate system. This method does not require a transformation nor an extension of the stiffness matrix size, though it requires proper boundary constraints: for this purpose, cylindrical constraint description is commonly used. The trial force method has similarities to the penalty function method, because it is based on the use of stiffness coefficients, and thus the solution is an approximation with one notable exception: the stiffness coefficient is updated during the contact evaluation.
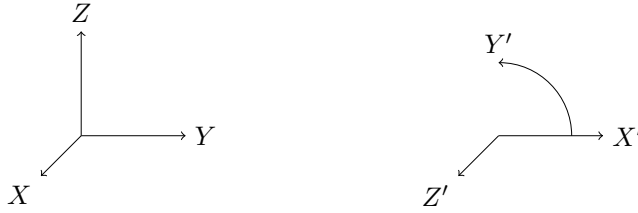


**Figure 2.10.** Two coordinate systems used; on the left is the right-handed Cartesian coordinate system, and on the right is the cylindrical coordinate system

Solution of the contact model introduced here requires two evaluation steps. The deformations are mapped from the Cartesian coordinate system in the cylindrical coordinate system, in which the contact detection is done. At this point, it is assumed that the axis of rotation observed the global $X$-axis. The two coordinate systems used are presented in Figure 2.10. The coordinate transformations are given in Equations (2.103) and (2.103).

$$\begin{aligned} X' &= \sqrt{Y^2 + Z^2} \\ Y' &= \arctan\left(Z, Y\right) \\ Z' &= X \end{aligned} \tag{2.103}$$

$$\begin{aligned} X &= Z' \\ Y &= X' \cos Y' \\ Z &= X' \sin Y' \end{aligned} \tag{2.104}$$

where $X'$, $Y'$ and $Z'$ are the radial, tangential and axial direction of the cylindrical coordinate system, respectively. After the contact force vector is calculated, the force vector components are mapped back into the Cartesian coordinate system. The first evaluation, according to Equation (2.105), takes all the external forces into account, with the exception of the possible contact forces. The deformation vector for the first evaluation can be written as follows:

$$\boldsymbol{u}_0 = \mathbf{K}_{e,\text{CYL}}^{-1} \boldsymbol{F}_{\text{ext}} \tag{2.105}$$

where $\mathbf{K}_{e,\text{CYL}}$ is stiffness matrix applied with cylindrical constraints. The radial distance between source–target nodes $\boldsymbol{\Delta u}_0'$ can be written as follows:

$$\boldsymbol{\Delta u}_0' = \boldsymbol{u}_{0,s}' - \boldsymbol{u}_{0,t}' \tag{2.106}$$
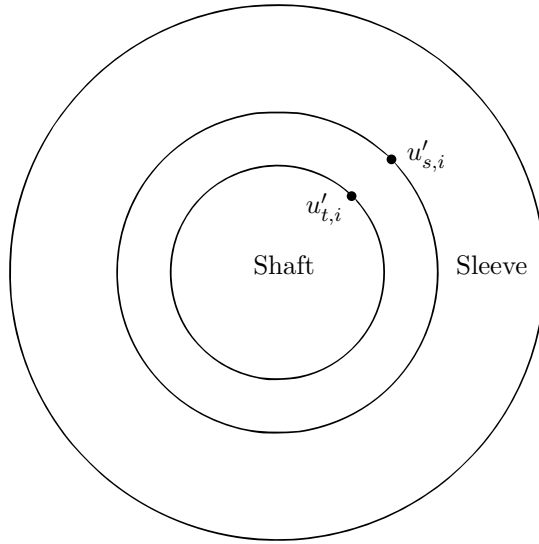


**Figure 2.11.** Source and target node $i$ of sleeve and shaft body

where the superscript $'$ describes the cylindrical coordinate system and the subscripts $s$ and $t$ correspond to the source and target as seen in Figure 2.11. The vector of logical multipliers $\boldsymbol{\gamma}_0'$ denotes which contact node pairs are opened and which are closed. This vector can be written as follows:

$$\boldsymbol{\gamma}_{0,u_i}' = \begin{cases} 1, & \text{if } \Delta u_{0,i}' < \delta_{\text{rad}} \\ 0, & \text{if } \Delta u_{0,i}' \geqslant \delta_{\text{rad}} \end{cases} \tag{2.107}$$

where $\boldsymbol{\gamma}_{0,u_i}'$ is the multiplier of radial component of source–target node pair $i$ and $\delta_{\text{rad}}$ is the radial interference of the shrink fit joint. The second evaluation step uses the inclusion of external force and trial contact force. Two known

variables, external force $\boldsymbol{F}_{\text{ext}}$ and trial contact force $\boldsymbol{F}_{c,\text{trial}}$, help in determining the unknown contact stiffness $\boldsymbol{k}_f k_0$. The final contact force $\boldsymbol{F}'_c$ can be calculated by solving the contact stiffness. The deformation vector in global Cartesian coordinates for the second evaluation can be written as follows:

$$\boldsymbol{u}_{\text{trial}} = \mathbf{K}^{-1}_{e,\text{CYL}} \left( \boldsymbol{F}_{\text{ext}} + \boldsymbol{F}_{c,\text{trial}} \right) \tag{2.108}$$

where $\boldsymbol{F}'_{c,\text{trial}}$ is the vector of trial contact force in the cylindrical coordinate system written as follows:

$$\boldsymbol{F}'_{c,\text{trial}} = k_0 \boldsymbol{\Delta u}'_0 \cdot \boldsymbol{\gamma}'_0 \tag{2.109}$$

where $k_0$ is the initial value for the contact stiffness. The final contact force vector can be written as follows:

$$\boldsymbol{F}'_c = \boldsymbol{k}_f \cdot \boldsymbol{F}'_{c,\text{trial}} \tag{2.110}$$

where $\boldsymbol{k}_f$ is the vector of multipliers for initial contact stiffness. When using the linear isotropic material model, the multiplier for source–target node pair $i$ is given as follows:

$$\delta_{\text{rad}} - \Delta u'_{0,i} - k_{f,i} \left( \Delta u'_{\text{trial},i} - \Delta u'_{0,i} \right) \gamma'_{0,u_i} = 0 \tag{2.111}$$

If $\gamma'_{0,u_i} = 1$, then

$$k_{f,i} = \frac{\delta_{\text{rad}} - \Delta u'_{0,i}}{\Delta u'_{\text{trial},i} - \Delta u'_{0,i}} \tag{2.112}$$

The vector $\boldsymbol{\Delta u}'_{\text{trial}}$ calculated as based on the trial evaluation can be written as follows:

$$\boldsymbol{\Delta u}'_{\text{trial}} = \boldsymbol{u}'_{trial,s} - \boldsymbol{u}'_{trial,t} \tag{2.113}$$

Since the trial force method does not use cross coupling stiffness terms in the stiffness matrix, the solution of stiffness equations can be distributed as expressed in Equation (2.114) by rearranging the equations:

$$\mathbf{K}_{\text{assembly}} \boldsymbol{u}_{\text{tot}} = \boldsymbol{F}_{\text{tot}}$$
$$\begin{bmatrix} \mathbf{K}_{\text{shaft}} & \mathbf{0} \\ \mathbf{0} & \mathbf{K}_{\text{sleeve}} \end{bmatrix} \begin{bmatrix} \boldsymbol{u}_{\text{shaft}} \\ \boldsymbol{u}_{\text{sleeve}} \end{bmatrix} = \begin{bmatrix} \boldsymbol{F}_{\text{tot,shaft}} \\ \boldsymbol{F}_{\text{tot,sleeve}} \end{bmatrix} \tag{2.114}$$

### 2.2.5 Use of constraint equations for contact modeling

Constraint equations are used for contact modeling. The contact modeling description given here refers to static contact problems, and the solution can be applied for eigenvalue problems. Generally, any contact can be open meaning the contact bodies do not touch each others, or closed, when the contact bodies are connected together. Simplification of opened and closed contacts is illustrated in Figure 2.12, where the gap $g$ represents the normal distance between two bodies. Let us consider the following cases

1. Contact is opened when the normal distance between two bodies is positive

2. Contact is closed with no reaction forces, when the normal distance between two bodies is zero

3. Contact is closed and reaction forces are required, when the normal distance between two bodies is negative
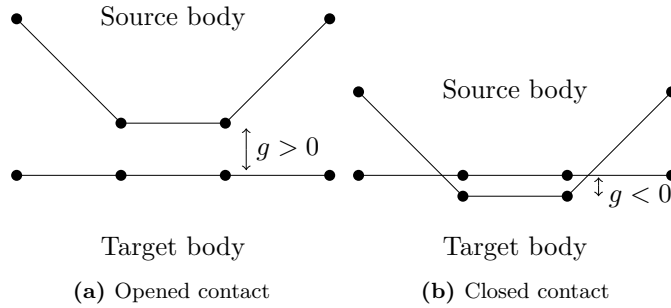


**Figure 2.12.** Simplified expressions of opened and closed contacts

In case 3, the required reaction forces repair the overlapping, ideally returning it according to case 2 and thus causing initial stress stiffening. It is also possible to apply a constant numerical gap or overlapping between two bodies by using non-homogeneous constraint equations.

In addition to solid element mesh, commercial software may use separate surface elements for contact detection. Regardless of use or non-use of separate contact elements, the contact treatment is based on employing constraint equations. In this dissertation, the focus is on elementless contact detection and treatment done at node points. Certain commercial FE software such as Ansys do also use integration point-based contact detection [4]. This method can enable more accurate contact detection since the number of detection points is increased. Elementless contact detection denotes then non-use of separate contact elements. Because separate contact elements are not used, contact detection is performed on a nodal basis. This procedure is referred as node-to-node contact detection, and for contact treatment for the use of constraint equations, source–target node
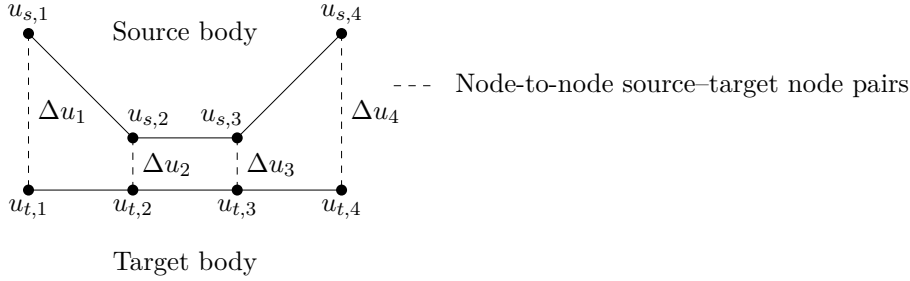
**Figure 2.13.** Illustration of elementless node-to-node contact detection

pairs are formed. A simplified illustration of node-to-node contact detection and source–target node pairs between two bodies is provided in Figure 2.13.

Here, the contact details specified to rotor dynamics use are discussed. Let us consider a shrink fitted shaft–sleeve contact. The starting point would be a clean unmodified geometry, and the contact specific geometric modification would be done only as numerical modifications.

- If external forces are not present, the normal distance between two bodies must be increased to the required radial shrink fit value by applying non-homogeneous constraints.

- If external forces are present but the normal distance between two bodies remains smaller than the required radial shrink fit value, non-homogeneous constraints must be applied to increase the normal distance to the required radial shrink fit value.

- If external forces are present and the normal distance between two bodies is greater than the required radial shrink fit value, no contact treatment is required.

Certain meshing tools can create a mesh where nodes of the source and target surface are overlapping, meaning the distance between source and target nodes is zero, thus enabling node-to-node contact. If the overlapping node discretization on the contact region of two different bodies is not achieved by the mesh generator, other methods may be used. One method is node duplication; the contact region between two bodies must be removed by combining these bodies into a group, and after meshing the duplication of nodes on this boundary must be done. Another method is to form node groups and interpolate weight coefficients for these grouped nodes; in terms of contact force vectors, one source node is selected and, for example, the three closest corresponding target nodes are selected and the contact reaction force is divided for these target nodes using proper weight coefficients. The latter method given here is not used in this dissertation.

### 2.2.6   Summary on constraint equations

The master-slave method is exact, but because of the forced displacements used, the global force vector should be evaluated and inspected for the possible presence of extremely high amplitude force components. If this method is improperly used for structural stress analysis, extreme hot spot stress peaks may appear in near proximity of the constrained surface. The analyst must pay attention to these evaluated forces and, if needed, use a different constraint method. Also, the use of the transformation matrix with sparse matrices may cause unwanted excessive use of the random-access memory.

The penalty function method is a good choice for the general contact problem, because of the use of the penalty weight. This method is based on the use of a stiffness coefficient and should reach accurate force equilibrium, though the convergence of the solution is dependent on the penalty weight used. If too large weight is used, the stiffness matrix may become ill-conditioned and the solution inaccurate. The accuracy of this method is proportional to the magnitude penalty weight used.

Use of the Lagrangian method will extend the stiffness matrix size. Although the bordered matrix added may be sparse enough, the total number unknowns is nevertheless increased. On the other hand, the part in the modified stiffness matrix storing the original stiffness equations remains unchanged, thereby differing from the master-slave or penalty function method. This method yields an accurate solution, and the Lagrangian multiplier contains the information about the constraint forces. Neither, the MPC and Lagrangian method, do not allow residual penetration in the contact. Because of this, these methods may not well suited for transient analysis, because the contact may oscillate between opened and closed status.

The trial force method is a custom application-specific constraint method developed for the purposes of modeling shrink-fitted joints for rotor dynamics analyses. For this reason, the formulation is provided in the cylindrical coordinate system. This method is unique to other constraint methods presented. The trial force method is used typically with cylindrical constraints applied, and the actual contact treatment is handled by manipulating the total external force vector.

The augmented Lagrangian method based on the use of Lagrangian multipliers from the Lagrangian method and penalty weight from penalty function method. This method is, perhaps, the most complex constraint equation method, but it also has certain benefits. Many commercial FE software support this method. The main reasons would be data storage and the fact that the unconstrained stiffness matrix may be kept unmodified. In addition, contact convergence is much easier due to the augmented part, because minor residual penetration of the contact region is allowed. With an exact constraint method, contact can only be either opened or closed. This can cause unwanted oscillation between

opened and closed contact status, especially during transient structural analysis. Stiffness coefficient based methods introduced, the penalty function, trial force and augmented Lagrangian methods, may be used in transient analysis with proper contact damping. These method allow residual penetration in the contact, thus no oscillation of contact status should appear.

Different constraint methods have varying requirements for solving the stiffness equations. When using Lagrangian based method, the system of linear equations must be solved directly, which can be computationally more expensive [4]. The penalty function method and trial force method, on the other hand, do not require direct solution: the solution of the system of linear equations can be iterative, thus computationally more effective. This is typically achieved using an iterative solver obtaining a solution in the system of linear equations [4]. The use of an iterative solver may, however, results in a minor error in the solution, since the solution is obtained when the tolerance, or error margin, is passed. The trial force method does have another beneficial feature. The penalty function method uses cross coupling terms in the modified stiffness matrix. The trial force method does not require these cross coupling terms: thus, by rearranging the equations, the stiffness equations can be distributed as expressed in Equation (2.114). By doing so, the solution for a smaller system of linear equation – for a single body, for example – can be obtained using either a full or iterative solver routine. In addition, if so desired, various DOF reduction methods such as the static condensation method can be implemented, making the problem solution even more computationally effective.

## 2.3   Solution methods

Solution methods for pre-stressed eigenvalue problem with contact non-linearities, for transient thermal mechanical stress analysis and for the transient rotor dropdown event simulation, are provided. The theory of undamped and damped eigenvalue problems is also given. The solution routines are presented in the form of flowcharts. The results presented in Section 3 are produced using the solution methods introduced.

### 2.3.1   Undamped and damped eigenvalue problem

Undamped and damped eigenvalue problems with regard to rotor dynamics analysis are presented. The solution routine for generating a Campbell diagram including contact non-linearities and the stress-stiffening effect is proposed.

**Undamped eigenvalue problem**

The undamped eigenvalue problem is used to study structures without any

damping, including gyroscopic damping. The equation of motion can be written as follows

$$\mathbf{M}\ddot{\boldsymbol{x}} + \mathbf{K}_{\text{tot}}\boldsymbol{x} = \mathbf{0} \tag{2.115}$$

where $\mathbf{K}_{\text{tot}}$ contains all stiffness properties: elastic structural stiffness, possible bearing stiffness components, possible contact stiffness description and possible stress-stiffening description. The eigenvalue equation for undamped problem can be written as follows [60]:

$$\left(\mathbf{K}_{\text{tot}} - \lambda_i \mathbf{M}\right)\boldsymbol{z}_i = 0 \tag{2.116}$$

where $\boldsymbol{z}_i$ is the eigenvector and $\lambda_i$ is the eigenvalue of the $i$th eigenmode. If matrices are not symmetrical, the eigenvalue solution yields complex eigenvalues.

**Damped eigenvalue problem**

The damped eigenvalue problem, also known as the quadratic eigenvalue problem, is used to study the rotating structures for such purposes as generating a Campbell diagram. The equation of motion can be written as follows:

$$\mathbf{M}\ddot{\boldsymbol{x}} + \left(\mathbf{C}_{\text{tot}} + \Omega\mathbf{G}\right)\dot{\boldsymbol{x}} + \mathbf{K}_{\text{tot}}\boldsymbol{x} = \mathbf{0} \tag{2.117}$$

The following non-symmetric state space matrix $\mathbf{A}$ can be formed from Equation (2.117).

$$\mathbf{A} = \begin{bmatrix} \mathbf{0} & \mathbf{I} \\ -\mathbf{M}^{-1}\mathbf{K}_{\text{tot}} & -\mathbf{M}^{-1}\left(\mathbf{C}_{\text{tot}} + \Omega\mathbf{G}\right) \end{bmatrix} \tag{2.118}$$

where $\mathbf{K}_{\text{tot}}$ contains all stiffness properties: elastic structural stiffness, possible bearing stiffness components, possible contact stiffness description and possible stress-stiffening description. Similarly, $\mathbf{C}_{\text{tot}}$ contains all damping properties: elastic damping, possible bearing damping components and possible contact damping description. The eigenvectors and eigenvalues are provided by solving the eigenvalue problem [38]

$$\mathbf{A}\boldsymbol{z}_i = \lambda_i \boldsymbol{z}_i \tag{2.119}$$

Damped eigenvalues appear in a form of complex conjugate pairs, the $i$th eigenvalue pair can be written as follows:

$$\lambda_i = \lambda_i^r \pm \lambda_i^i i_u \tag{2.120}$$

where $\lambda_i^r$ and $\lambda_i^i$ are the real and imaginary parts of eigenvalue $i$, correspondingly, $\beta_i$ is the damped natural frequency of $i$th eigenmode and $i_u$ is the imaginary unit $i_u = \sqrt{-1}$. Equation (2.120) can be written as follows [38]:

$$\lambda_i = -\xi_i^d \omega_{n,i} \pm \omega_{d,i} i_u \tag{2.121}$$

where $\xi_i^d$ is the damping ratio, $\omega_{n,i}$ is the undamped natural frequency and $\omega_{d,i}$ is the damped natural frequency of eigenmode $i$, correspondingly. The correlation between the damped and undamped natural frequency can be written as follows:

$$\omega_{d,i} = \omega_{n,i}\sqrt{1 - \xi_i^{d2}} \tag{2.122}$$

**Solution method for Campbell diagram**

The solution routine for Campbell diagram for a rotor having multiple parts is introduced in Figure 2.14. First, using the rotational speed $\Omega$ of the analysis step $n$, the deformations due to external forces are calculated. Based on initial deformations, proper contact treatment is performed. If contact remains fully or partially closed, contact force vector is generated. The total deformations due to external forces and contact forces are solved. Based on these deformations, the stresses of the structure are calculated and the stress stiffness matrix is formulated. Bearing coefficient matrices $\mathbf{K}_b$ and $\mathbf{C}_b$ describing the bearing stiffness and damping, respectively, are introduced. The description of the contact stiffness matrix $\mathbf{K}_c$ is given after the general solution routine description.

The undamped eigenvalue problem is solved using the total stiffness $\mathbf{K}_{\text{tot}}$ and the mass matrix $\mathbf{M}$. A subset of $n$ lowest eigenmode vectors is solved and used to form the modal structural matrices. The use of modal matrices is justified duo to the significantly lower memory consumption while solving the eigenvalues of the state space matrix. The solution of the damped eigenvalue problem yields the damped complex conjugated pair eigenvalues, and the damped parts of the conjugated pairs, $\beta_i$, are stored and plotted with the rotational speed vector, in order to generate the Campbell diagram.

The contact stiffness matrix $\mathbf{K}_c$ describes the connections on the contact region between the source and target nodes of the contact bodies. These stiff connections are established by applying the penalty elements between the DOFs of source and target nodes. As illustrated in Figure 2.14, the vector of logical multipliers $\boldsymbol{\gamma}_0'$ is used to determine which source–target node pairs remain closed and are applied with the penalty element, and which node pairs are opened and do not require any attention.
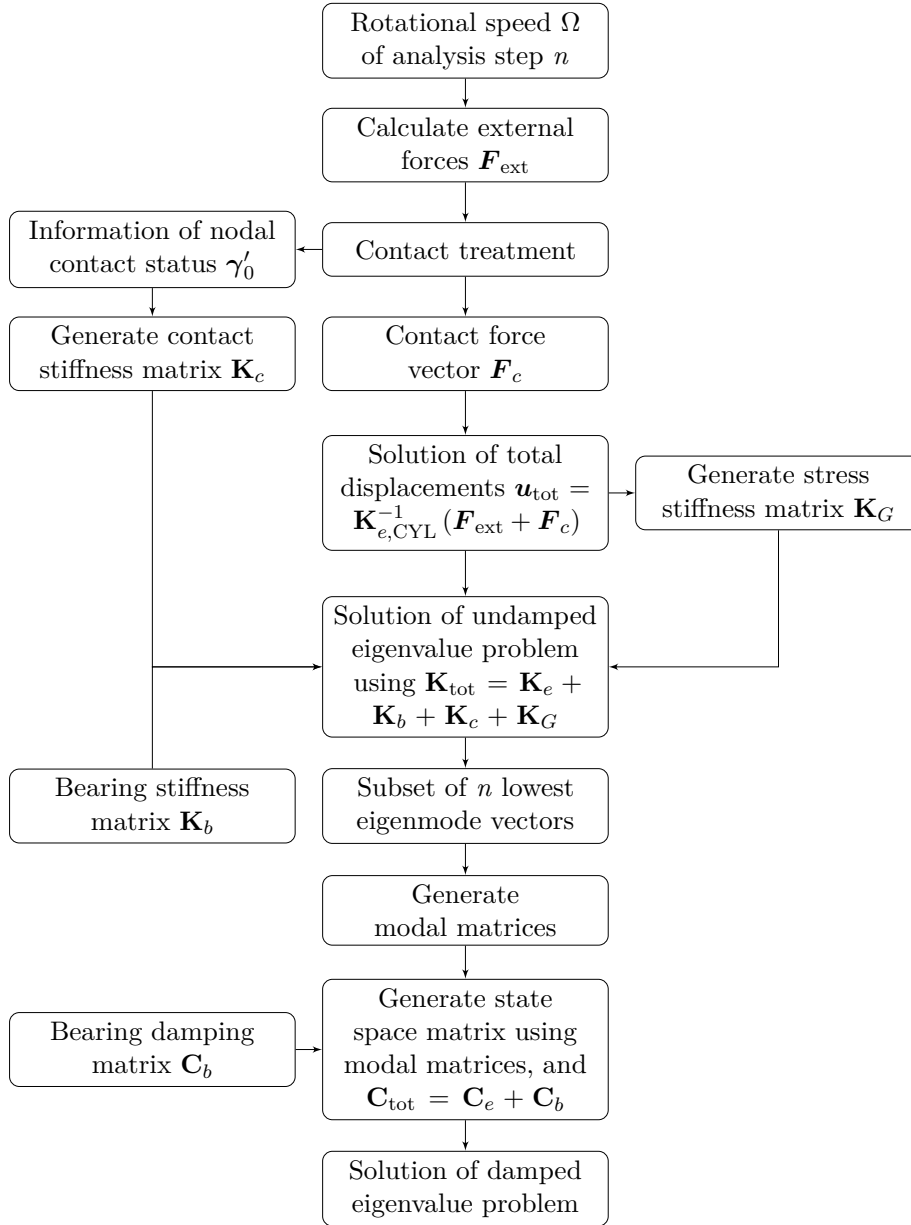
**Figure 2.14.** Process diagram for generating Campbell diagram for a rotor model with contacts

### 2.3.2 Coupled thermal mechanical analysis

The indirectly coupled thermal mechanical analysis routine, which can be applied to various of applications such as electric motor rotors, is introduced here. Indirectly coupled, also called as weakly coupled, problem is considered more

memory-efficient than the directly coupled problem, because the systems of linear equations for heat transfer and static structural problems are solved sequentially. Directly coupled problem has tendency to use larger system matrices as the two sets of linear equations, in this case, are directly coupled. The finite element analysis (FEA) is performed in two steps: first, a transient thermal study is carried out over the drive cycle to calculate the temperature distribution. Second, the temperature distribution is applied as an initial thermal condition for every simulation time step along with other mechanical loads. Figure 2.15 presents a schematic of thermal mechanical simulation steps describing the inputs and output.
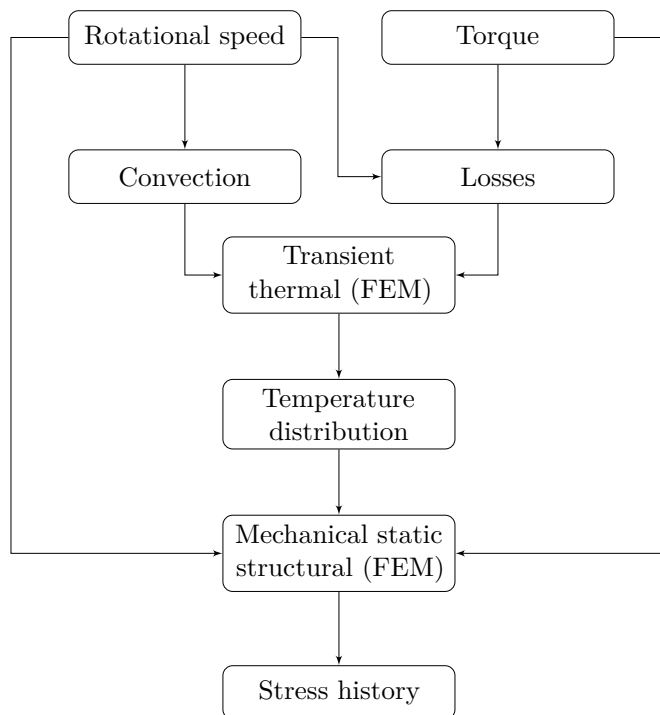


**Figure 2.15.** Process diagram for the thermomechanical stress analysis

In the transient thermal FEA, the temperature distribution of the rotating machinery is calculated as a function time. In FE model, the electromagnetic heat losses, that can be depended on torque and rotation speed, are modeled as volumetric heat sources in corresponding bodies, such as magnets and lamination stacks. Convective heat transfer boundaries are applied to the model as boundary conditions describing the effect of air cooling. The convection coefficients used are dependent on the speed differences and are thereby dependent on the rotational speed of the rotor.

In the mechanical static structural FEA, the previously solved temperature history is used as one of the input loads. In every simulation step, the thermal expansion effect must be converted into expanding body force distribution in order to provide

superposition of all the mechanical forces. The conversion from temperature into force is done as a pre-process by first calculating only the strain caused by thermal expansion, and then the strain state is converted into the body force vector. After this, the rest of the mechanical forces are applied, the tangential forces generated by the torque, and the centrifugal forces from the rotational speed. Finally, all the mechanical forces are combined to solve the total stress history.

### 2.3.3 Fundamentals of fatigue life calculation

A fatigue life calculation is performed using the calculated stress history calculated. Rainflow cycle counting as well as Palmgren-Miner linear damage hypothesis method are applied to evaluate the equivalent stress cycle $\Delta\sigma_{\text{eq}}$ from a complex and non-uniform stress history. The equivalent stress is used to identify the stress reversals and to prepare damage summation for the structure [59, 52]. The equivalent stress cycle that would cause similar fatigue as cumulative fatigue damage during the load cycle can be written as follows:

$$\Delta\sigma_{\text{eq}} = \sqrt[\beta]{\frac{\sum_{i=1}^{\kappa} z_i^c \Delta\sigma^{\beta}}{N}} \tag{2.123}$$

where $\kappa$ is the number of the rainflow stress classes, $z_i^c$ is the number of repetitions in class $i$, $\Delta\sigma$ is the stress variation in the class, $\beta$ is the S-N curve slope, and $N$ is the number of stress repetitions in total. The number of rainflow stress classes is selected independently for each stress history curve using a suitable binwidth. A proper binwidth can be defined as suggested in Shimazaki and Shinumoto [89]. The selected binwidth takes the minimum and maximum stresses as well as stress variation over the used stress history into account. The binwidth should also be small enough to take the essential stress variation into consideration.

The Basquin equation for the number of applied equivalent stress fluctuations $N_f$ that the structure can tolerate until fatigue damage is developed, and it can be solved from the following equation [37]:

$$N_f = 0.5 \left(\frac{\Delta\sigma_{\text{eq}}}{2\sigma_f'}\right)^{1/b_e} \tag{2.124}$$

where $\sigma_f'$ is the fatigue strength coefficient and $b_e$ is the Basquin exponent or the fatigue strength exponent, which varies between -0.05 and -0.12 for most metals. From Equation (2.124), a smaller $b_e$ results in a longer fatigue life [8, 27].

### 2.3.4 Transient analysis of rotor dropdown event

Transient rotor dropdown event on backup bearings is studied in Neisi *at al.* [71], Sikanen *et al.* [90] and Neisi *et al.* [70]. In these publications, the rotor orbits and the contact forces on backup bearings are simulated. The backup bearing

internal stresses and the rotor bending stresses using 1D Timoshenko beam element approach are also studied. In Figure 2.16, a basic diagram of transient solution for rotor dropdown event on backup bearings is presented.
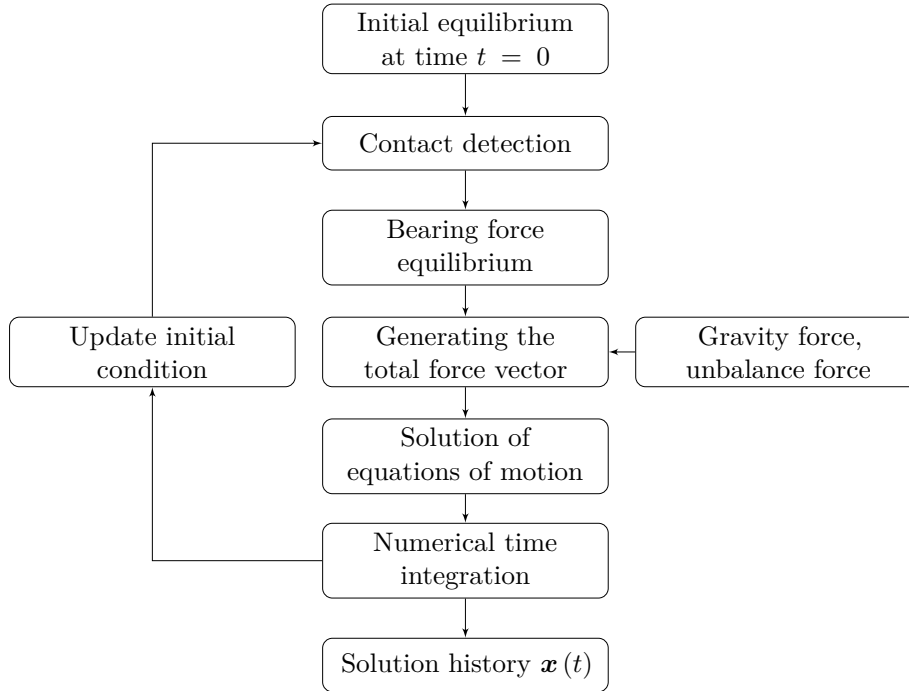


**Figure 2.16.** Process diagram for the transient solution of a rotor dropdown event on backup bearings

Time integration using a numerical integrator scheme is applied to solve the non-linear transient rotor-bearing contact. A detailed description of contact and bearing models are shown in [71] and [70]. Before the transient integration loop is initiated, the equilibrium solution of the numerical model should be obtained. During the integration loop, the system equations of motion are solved and proper nonlinear forces – such as contact force, bearing reaction force, and other general forces such as gravitation force and unbalance force – are taken into account. The solution of the integrated step solution is then inserted as a new initial condition, and a new time step is solved.

The rotor and bearing stress history can be solved separately after the main transient problem, because the transient problem is not dependent on the stress results. The diagram of routine for calculating the rotor and bearing stress is given in Figure 2.17. During this post-process phase, the solved displacement history is used to re-evaluate the equations of motion in order to recalculate the required force components: in this case, the bearing forces. The rotor stresses, on the other hand, can be calculated without the need to re-evaluate the equations of motion, because the rotor stresses are dependent only on the nodal displacements that are already solved. Because the solution of equations of motion does not
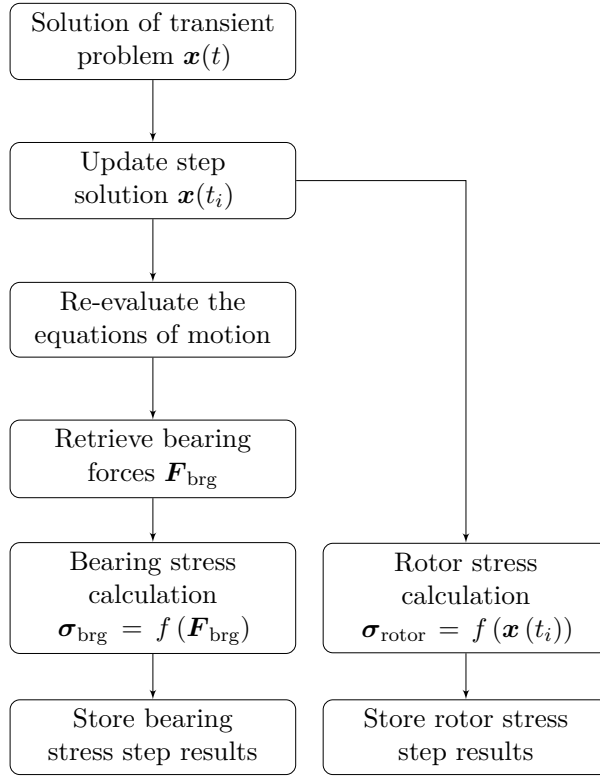
**Figure 2.17.** Process diagram for calculating the rotor and bearing stress history

require evaluation of the rotor stress calculation function, it can be omitted during transient solution. The equations for rotor stress calculation are provided in [90], and the equations for bearing stress calculation in [71].

# Studies of rotating structures

In this chapter, transient beam element-based rotor dropdown simulation and the results of rotor and bearing stress history are presented. The correction of beam element-based rotor model properties using experimental modal data is presented. 3D solid element modeling is utilized for studying rotors having contacts. The numerical results of shrink-fitted joint behavior are verified using the experimental modal analysis results from manufactured test shafts. The results of transient thermal mechanical stress and fatigue analysis of a rotor of a traction motor using measured drive cycle data are presented. As introduced, all the numerical studies in this chapter utilize measured data. A comprehensive theory of structural and heat transfer finite element modeling introduced in Chapter 2 is utilized for generating the results presented in this chapter, including the solution routines and contact modeling introduced in Sections 2.3 and 2.2.5.

## 3.1   Rotor dropdown simulation

Rotor dropdown is an event when AMB-supported rotating machinery experiences a failure in the AMB control system. In the worst case scenario, the magnetic levitation field collapses and the rotor start to fall free. AMB-supported machinery is, by default, equipped with backup bearings, which will catch the falling rotor and prevent possible catastrophic rotor-stator contact from happening. This secondary bearing system will support the rotor during emergency shutdown. In this section, the rotor dropdown event on backup bearings is studied. These results are based on [90]. Rotor models are generated using the Timoshenko beam element approach for its good compatibility as computational speed for transient analysis purposes. Angular acceleration dependent effects according to Equation (2.1) are neglected. The stress state of a flexible rotor during dropdown is calculated, as based on the previously solved displacement history. In addition, backup bearing Hertzian stress history is calculated as a post-process by re-evaluating the system equations of motion. Both of these stress calculation routines are provided in Section 2.3.4.

### 3.1.1 Dropdown simulation of an AMB-supported rotor

The schematic of the AMB-supported rotor studied is presented in Figure 3.1. The finite element model consists of 26 beam elements. The backup bearings are connected to nodes 2 and 25, while the axial AMB disk is located in node 4. The dropdown event is studied by performing simulations for the first 0.5 s of the dropdown event, and the transient data is stored at 10 µs intervals. Simulation is performed in Matlab using a native ode15s solver with a relative error of $1 \times 10^{-4}$ and maximum step size of $5 \times 10^{-6}$ s.
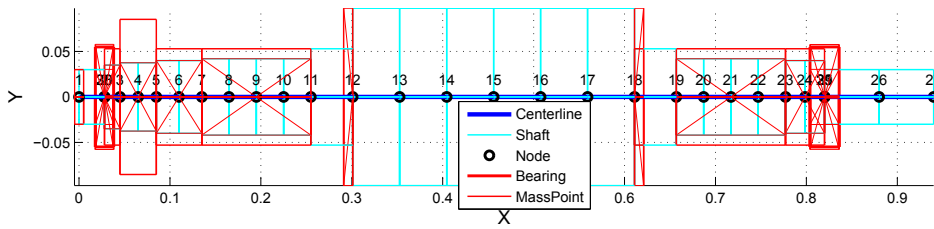


**Figure 3.1.** Rotor model elements and dimensions

The testing of the designed AMB system is performed in custom research code in Matlab environment. The virtual model of the rotor is verified using the experimental modal analysis for the rotor. The simulation model is fine-tuned as based on the measurement results, by modifying the stiffness of the rotor AMB laminations and other sleeve structures over the main shaft. Figure 3.2 presents the measurement setup where a scanning laser doppler vibrometer was used. The comparison of natural frequencies of the rotor gathered by experimental measurements and simulations is presented in Table 3.1. Only the four lowest bending mode (BM) pairs are observed, because the modes of the lowest orders contribute mainly in the dynamic performance; even though a total of four rigid body modes and 16 flexible lateral bending modes are used in simulation model. Axisymmetric description of the rotor elements is used in the rotor model. Therefore, the frequencies of the bending modes in both lateral directions in the model are equal. The actual system is asymmetric which can be seen from the measured natural frequencies that have deviation between the bending mode directions. The measured rotor is balanced in grade G2.5, as defined by ISO1940-1 standard [39]. Unbalance masses used in the simulation are assumed to be in three locations. The first one is assumed to be on the axial disc of the axial AMB with a value of 1.07 gmm. The second one is in the center of the rotor, with a value of 2.78 gmm. The last is located at the connection gear with a value of 4.56 gmm.

The dropdown event of the rotor system is simulated by dropping down the rotor to the backup bearings at the speed of 15,000 rpm. The simulation utilizes the method introduced by Kärkkäinen *et al.* [51] including the Hertzian contact model for rotor-bearing contact, and the bearing model is modified for cageless bearings by Halminen *et al.* [36]. The initial condition – the rotor-bearing system
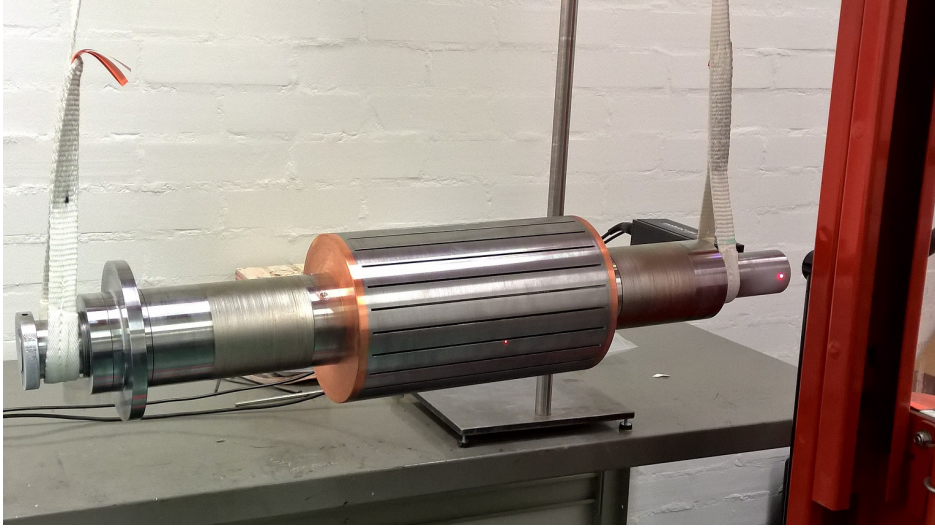
**Figure 3.2.** Measurement setup for experimental modal analysis

**Table 3.1.** Bending frequencies of fine-tuned rotor FE model and measured physical rotor

| Mode | Frequency (Hz) | |
| --- | --- | --- |
| | Simulated | Measured[1] |
| 1. bending | 673.5 | 661 / 670 |
| 2. bending | 1071 | 1096 / 1130 |
| 3. bending | 2363 | 2406 / 2427 |
| 4. bending | 2925 | 2857 / 2895 |

[1] Measurement performed in two planes

equilibrium – is set so that the rotor center point is located in its nominal center of the backup bearings when no misalignment is introduced. The translational velocities are also set as zero. During radial AMB levitation, the rotor can circulate around its nominal center of the AMB, thus having non-zero translational and tangential velocities. Therefore, this initial condition for the dropdown event should be taken into account, though the rotor dropdown behavior and the initial contact forces are highly dependent on the tangential velocity of the rotor right at the moment when the dropdown is initiated. Thus, the only simple way to set the initial condition for the dropdown event without including the AMB system model, is to assume the rotor lateral velocities to be zero. Some literature [9, 10] exist in which the steady-state condition of the AMB levitated system is described for use as an initial condition for the rotor dropdown simulation.

The air gap between the backup bearings and the rotor is 250 μm. The rotor system uses two individual backup bearing types. The bearing in the non-drive

end, the left end according to Figures 3.1 and 3.2, is 6014, a ceramic, deep groove, high-precision ball bearing. In the drive end, the bearing type is 5S-7914UC, a ceramic, deep groove, ball bearing. The properties of these bearings are shown in Table 3.2. In addition, the friction coefficients utilized between the rotor and the inner rings of the bearings are introduced. A total of three cases are studied. In the first studied case, both bearings are ideally aligned. In the two other cases, the horizontal misalignment between the bearings are 100 and 200 µm, respectively.
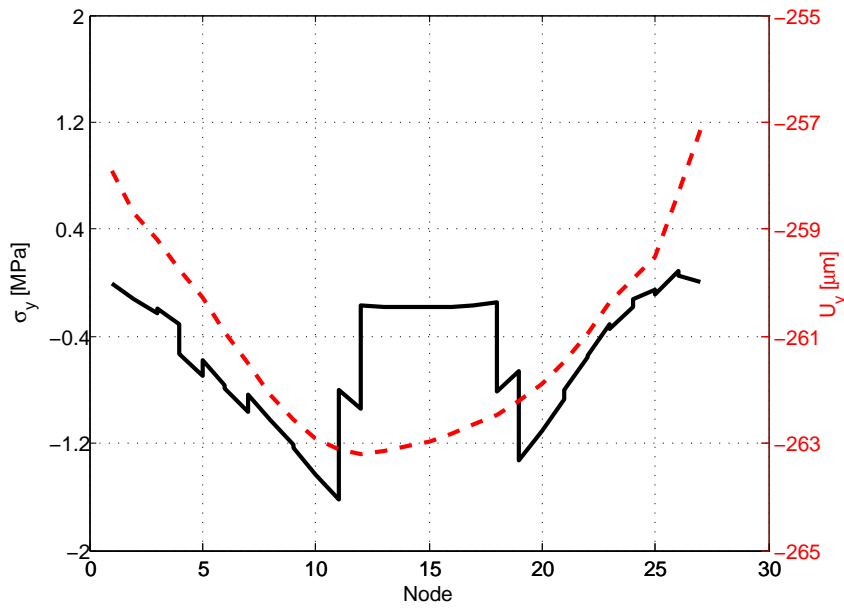


**Figure 3.3.** Static deflection and corresponding bending stress of a shaft laying freely on the bearings
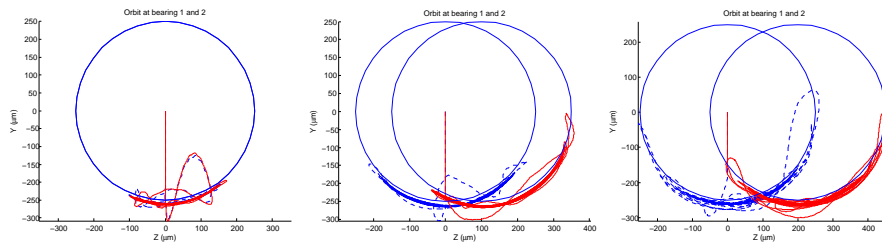


**Figure 3.4.** Orbits of the studied dropdown cases. From left to right the misalignments are 0 µm, 100 µm and 200 µm. The red solid line is the orbit at the free, end and the blue dashed line is the orbit on the drive side.

**Table 3.2.** Backup bearing properties

| Property | 6014 | 5S-7914UC |
|----------|------|-----------|
| Outer diameter (mm) | 110 | 110 |
| Bore diameter (mm) | 70 | 70 |
| Pitch diameter (mm) | 90 | 85 |
| Width (mm) | 20 | 16 |
| Ball diameter (mm) | 12 | 11.7 |
| Number of balls | 11 | 11 |
| Static load rating (N) | $31.0 \times 10^3$ | $20.9 \times 10^3$ |
| Damping coefficient (Ns/mm) | 0.30 | 0.27 |
| Internal clearance (mm) | $15 \times 10^{-3}$ | $9.0 \times 10^{-3}$ |
| Conformity ratio in | 0.52 | 0.52 |
| Conformity ratio out | 0.52 | 0.52 |
| Static friction factor | 0.11 | |
| Kinetic friction factor | 0.05 | |

### 3.1.2   Rotor stresses during dropdown event

Figure 3.4 shows the orbits of the rotor in dropdown. The orbits of all the studied cases are presented. As seen in Figure 3.4, the misalignment between the bearings greatly affect the behavior of the rotor after the dropdown. With the bearing completely aligned, the rotor bounces after the first contact, but after that it settles relatively fast at the bottom of the backup bearing inner rings. The misalignment of the bearings causes high oscillation behavior in the bottom of the bearing inner rings. The orbits in misaligned cases reach to the initial drop height in the vertical direction.

Figure 3.3 presents deflection and the bending stresses of the rotor during static equilibrium on the backup bearings. The mass of the rotor is not distributed evenly on the bearings at nodes 2 and 25, and the stiffness of the bearing on the other side is lower. Therefore, the displacement of the shaft at the locations of the bearing nodes is not equal.

**Table 3.3.** Comparison of maximum rotor stress components with various misalignments during dropdown

| Misalignment | Stress component (MPa) | | | |
|:---:|:---:|:---:|:---:|:---:|
| | $\sigma_y$ | $\sigma_z$ | $\tau_{xy}$ | $\tau_{xz}$ |
| 0 µm | 6.86 | 0.73 | 0.88 | 0.07 |
| 100 µm | 8.78 | 2.25 | 0.75 | 0.19 |
| 200 µm | 7.54 | 3.58 | 0.70 | 0.36 |

In Figures 3.5–3.8, the bending and shear stress behavior along the rotational axis by varying the horizontal misalignment of backup bearings is illustrated. The selection of the simulation results at the particular time is based on the maximum
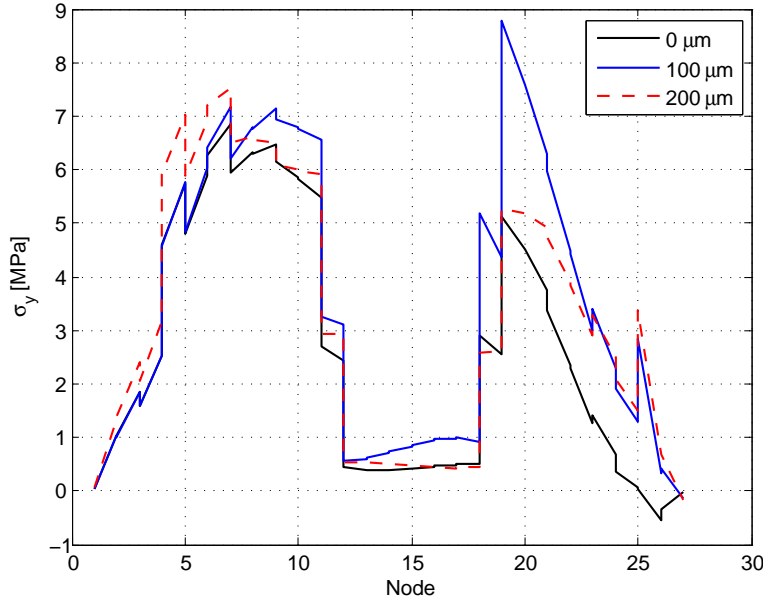
**Figure 3.5.** Rotor bending stress in $Y$-direction

bending stress at node 4, the axial AMB disk location, in $Y$-direction. Therefore, the time when the peak stress occurs in Figures 3.5–3.8 can differ among the misalignment cases studied. In all cases, the peak stress occurs immediately after initial contact. All absolute maximum bending and shear stresses are presented in Table 3.3 for comparison purposes.

### 3.1.3   Discussion

Rotor stresses during the dropdown event are studied. A Timoshenko beam element-based rotor model having 26 beam elements was generated. The eigenfrequencies of the FE model were compared against the results based on the experimental modal analysis, performed on a physical rotor. Based on the measured results, the FE model was modified so that the lowest flexible body bending mode eigenfrequencies of the FE model and physical rotor will match accordingly, emphasizing the first and second bending mode frequencies. Additional FE model tuning could include the verification of rotor mass. Also, in the case of non-trivial geometry, such as a squirrel cage rotor part, a segmented numerical verification becomes convenient. This means that in the beginning, only the rotor active part is modeled using beam elements. The mass, stiffness, and polar and diametral inertial are compared and tuned accordingly, emphasizing the desired parameters, thus achieving the optimum solution as based on a 3D solid element model. After this, trivial parts such as shoulders having a circular cross section can be included in a beam model. By doing so, we have managed to achieve an equivalent beam element model of complex 3D solid element geometry with significantly lower
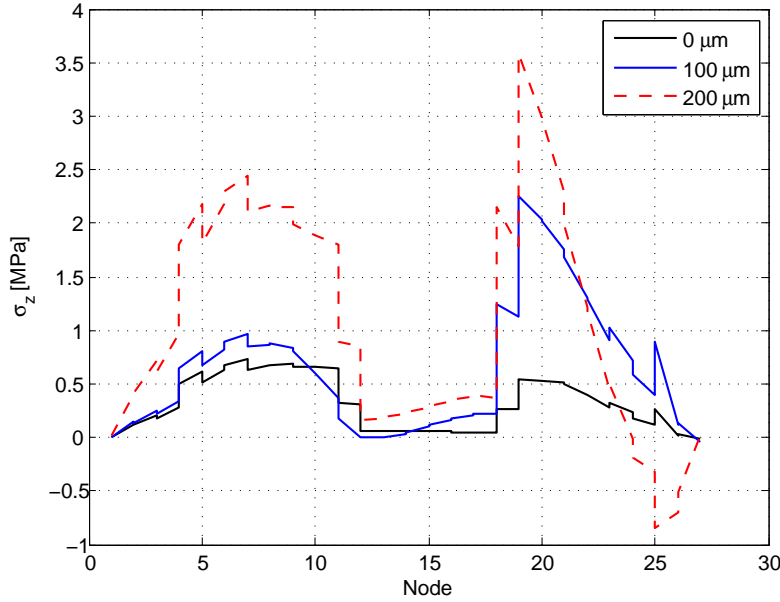
**Figure 3.6.** Rotor bending stress in *Z*-direction

computational requirements. In this studied rotor dropdown case, the rotor geometry modeled is axisymmetric, though, as introduced, the physical rotor is asymmetric. This asymmetry is due to the squirrel cage part of the rotor assembly. This is clearly visible in the EMA results in Table 3.1. Including this asymmetric effect requires the use of beam element formulated with inclusion of asymmetric cross section of element.

The static equilibrium of the rotor-backup bearing system is presented in Figure 3.3. The shape of the deflection and corresponding bending stress on the outer surface of the rotor are included. The absolute maximum rotor bending stress is approximately 1.6 MPa. This value is less that one-fifth of the maximum stress peak recorded during the dropdown event. This finding emphasizes how significant shifting in rotor bending stresses are, occurring after the dropdown has begun.

It can be seen that the difference of the cross section changes the stress distribution along the length of the rotor. Naturally, by changing the cross section properties, the stiffness of the rotor sections will change. Also, the change in diameter changes the distance of the observed point from the centerline, which exerts a direct impact on the stress results. Bending stresses at both ends of the rotor are zero. The bending stresses are low, due to the stiff cross section In the mid-section, where the active part of the electric machine is located.

The bending and shear stress behavior along the rotational axis having varied horizontal misalignment of the backup bearings is illustrated in Figures 3.5–3.8. By increasing the horizontal misalignment of the backup bearing, bending stress in the *Y*-direction in the vertical, gravitational direction will increase, as shown
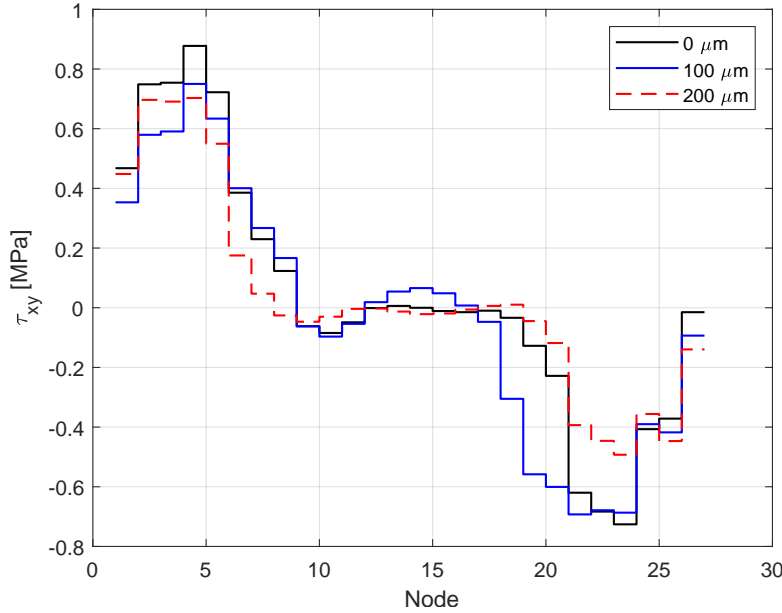
**Figure 3.7.** Rotor shear stress in $XY$-plane

in Figure 3.5. While using the axial AMB disk node as a reference point, the impact of increasing bearing misalignment is clearly present; though the highest bending stresses in Figures 3.5 and 3.6 are located at the drive end, right after the active part of the rotor. In the $Z$-direction horizontally, the bending stress also increases while additional misalignment is introduced. The shear stress variation in Figure 3.7 in $XY$-plane is minor, though in Figure 3.8 the stress increment in the $XZ$-plane is clearly proportional to the increased misalignment. Again, the peaks of absolute maximum shear stress are located at the drive end, directly after the active part of the rotor.

Although the free fall height when misalignment is introduced is less than with no misalignment and the change in potential energy is therefore less, the rotor still seems to bounce higher than in the case of no misalignment, according to Figure 3.4. Also, greater rocking motion is present. In Table 3.3, the maximum bending and shear stresses are compiled for comparison purposes. The effect of increased horizontal misalignment is visible. In addition, the time when the maximum stress peaks are present depends on the amount of misalignment. As discussed before, the increase in horizontal misalignment will reduce the vertical free fall height: it is thus expectable that maximum stresses may not occur at the same time.

The results of the rotor bending stress studies during rotor dropdown on backup bearings will give a good general understanding about the shifting rotor stress history during the dropdown event; though, in the physical rotor, there are also
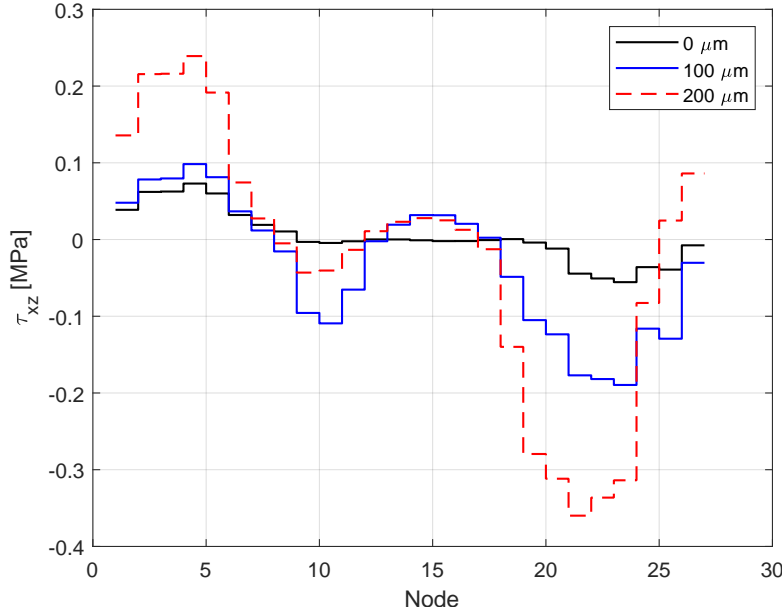
**Figure 3.8.** Rotor shear stress in $XZ$-plane

other stress sources present. The general stress state caused by the centrifugal force has significantly greater amplitude than the bending stresses, due to rotor contact on backup bearings as predicted using the beam element method. In addition, contact between other components, especially if shrink fitted joints are used, will yield high stress amplitudes. Thus, a physical rotor will experience significantly greater stresses even during normal use and even greater stresses during dropdown. When these speed and joint dependent stresses introduced are included in analysis by using the 3D solid element approach, the stress-stiffening effect should be taken into account. This effect can stiffen the rotor, and can have an effect on the rotor bending amplitude during the dropdown event. Regardless, the beam element approach for the rotor dropdown event is very useful for determining the rotor deformations. This information is essential for rotor-stator clearance design, especially in a case of overhung impeller.

## 3.2 Bearing stress simulation

An AMB-supported rotor system with backup bearing is studied in order to investigate the backup bearing stress history. The importance of analyzing the stresses that backup bearing experiences arises from the typical, often chaotic, nature of the dropdown event. During dropdown of a rotor of a high-speed motor, the bearing forces can be many times greater than during operation lower speed operation, when the connection between the rotor and bearing inner ring has no clearance. Because of the required operational air gap between rotor and

bearing inner ring, the rotor is allowed to bounce freely within the air gap. These results are based on [71]. Angular acceleration dependent effects according to Equation (2.1) are neglected. The main dimensions of the rotor and position of the AMBs and backup bearings are presented in Figure 3.10. Table 3.4 shows the parameters that are used in the dropdown event simulation. The FE model of the rotor is illustrated in Figure 3.9. The model comprises a total of 16 elements. The AMBs are located at nodes 6 and 12, and deep groove ball bearings used as backup bearings are located at nodes 4 and 14 in the FE model of the rotor. The parameters of the backup bearings are presented in Table 3.5. The Hertzian contact theory applied for the rotor-bearing contact is given in [71].

**Table 3.4.** Rotor data used for the bearing stress study

| Simulation parameter | Value |
|---|---|
| Mass of rotor | 97.3 kg |
| Initial rotation speed of the rotor | 20000 rpm |
| Modulus of elasticity | $2.0 \times 10^{11}$ Pa |
| Material density | 7801 kg/m$^3$ |
| Poisson's ratio | 0.3 |
| Support mass | 5 kg |
| Support stiffness | $5 \times 10^7$ N/m |
| Support damping | 5000 Ns/m |
| Contact stiffness[1] | $1.25 \times 10^9$ N/m$^{1.11}$ |
| Parameter for contact[2] | 0.08 |
| Air gap | 300 μm |
| Polar moment of inertia of rotor | 0.39 kgm$^2$ |
| Diameter moment of inertia of rotor | 2.82 kgm$^2$ |
| Inner diameter of sleeve | 60.6 mm |
| Outer diameter of sleeve | 80.0 mm |
| Unbalance mass (node 9) | $6 \times 10^5$ kgm at 0° |
| Static contact friction coefficient[1] | 0.2 |
| Dynamic contact friction coefficient[1] | 0.1 |

[1] Between rotor and inner race
[2] Associated with contact damping
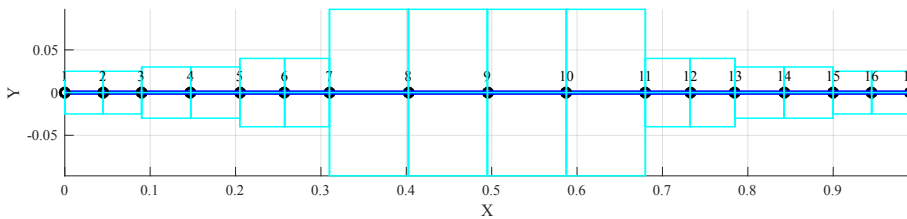


**Figure 3.9.** FE-mesh of the rotor used for bearing stress study

The dropdown event is simulated for 1 s, and the simulation time step is 10 μs. The equations of motion are time-integrated using Matlab ode45. The relative error and maximum step size are equal to $1 \times 10^{-5}$ and 10 μs, respectively.
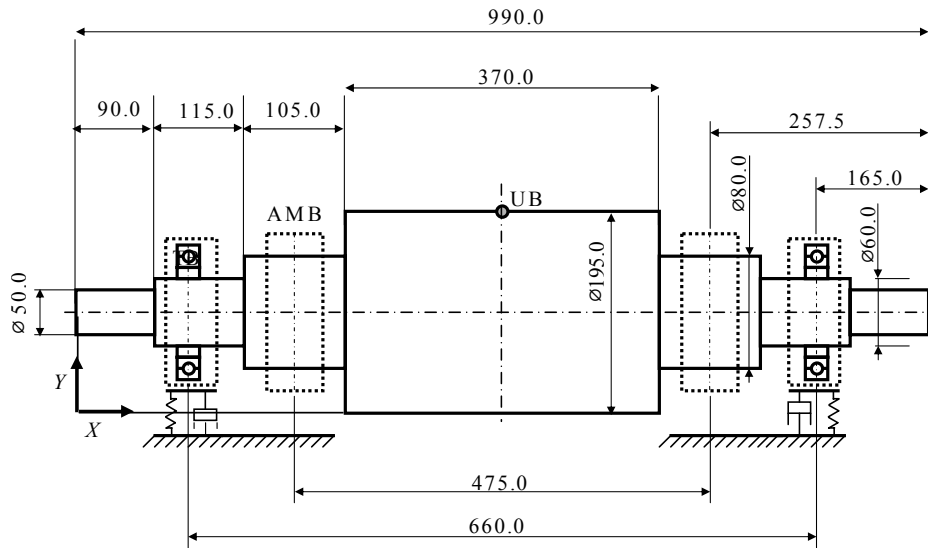


**Figure 3.10.** Main dimensions of the rotor model used for bearing stress study

**Table 3.5.** 6016 deep groove ball bearing properties used for the bearing stress study

| Bearing parameter | Value |
| --- | --- |
| Bearing damping coefficient | 0.25 Ns/mm |
| Bearing diametric clearance | 15 μm |
| Outer diameter | 125 mm |
| Ball diameter | 19.05 mm |
| Pitch diameter | 110 mm |
| Bore diameter | 80 mm |
| Modulus of elasticity of ball | $2 \times 10^{11}$ Pa |
| Modulus of elasticity of inner race | $2 \times 10^{11}$ Pa |
| Poisson's ratio of ball | 0.3 |
| Poisson's ratio of inner race | 0.3 |
| Conformity ratio | 0.52 |
| Number of balls | 10 |

### 3.2.1 Stress in a backup bearing during dropdown

In the simulation, the penetration of the ball in the inner race is calculated from the relative displacements between the inner and outer races. Figure 3.11 illustrates the orbit of rotor during the dropdown. In this figure, the dashed line

shows the air gap and the solid line shows the path of the rotor center point at
the bearing location during the dropdown event. After the first contact between
the rotor and bearing, the rotor bounces, after which it settles steadily on the
bottom of the inner race.
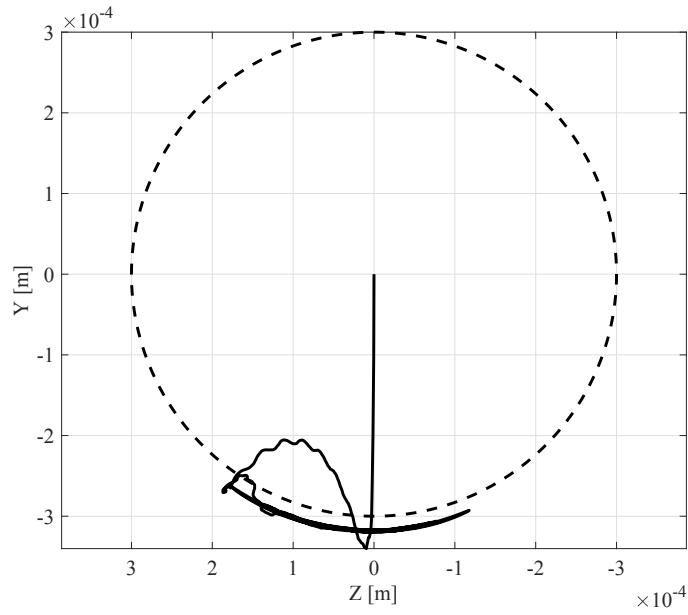


**Figure 3.11.** Orbit of the rotor during the dropdown event
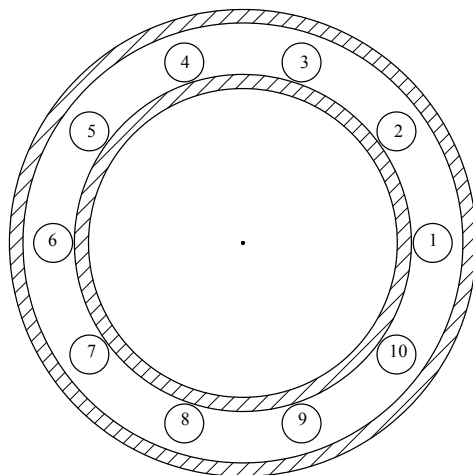


**Figure 3.12.** Ball arrangement at the start of the simulation
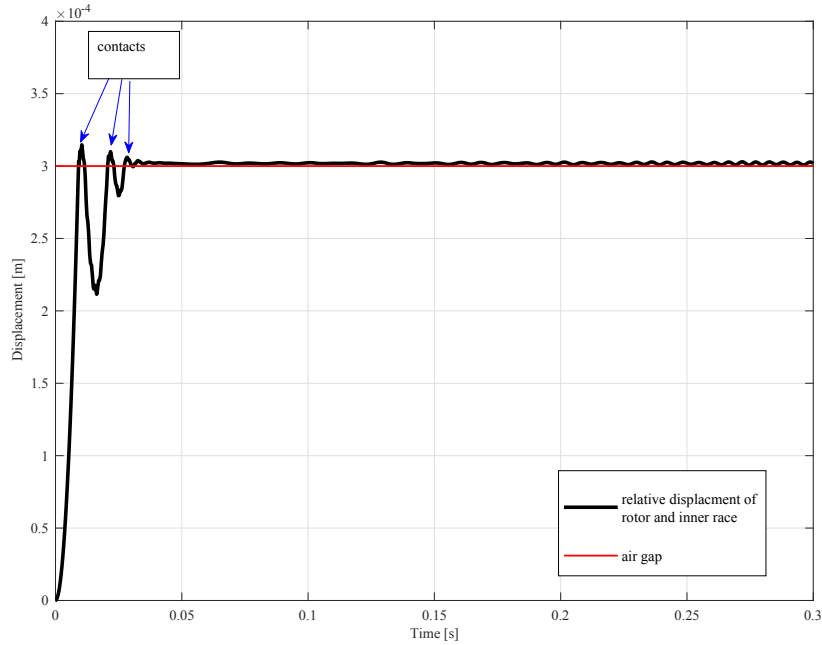
**Figure 3.13.** Relative displacement of the rotor and the inner race
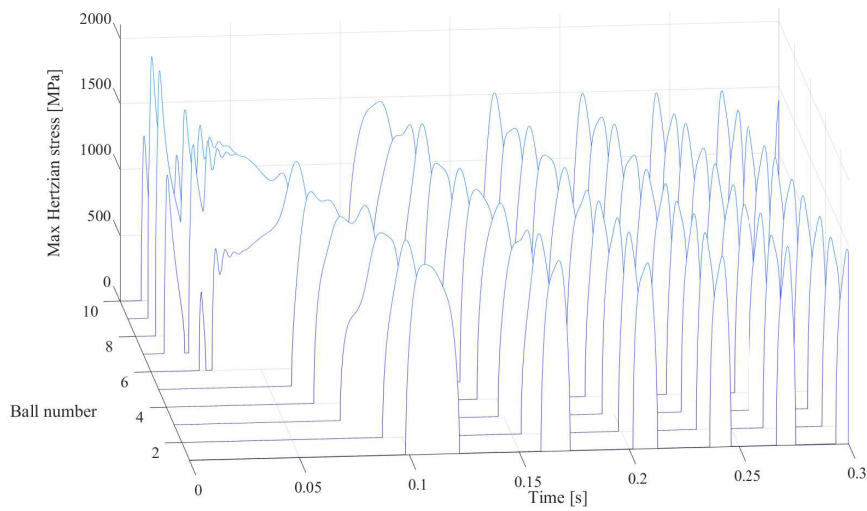


**Figure 3.14.** Maximum Hertzian stress of each ball

Figure 3.13 shows the relative displacement of the rotor and inner race as a function of time. The first contact of the rotor and backup bearing occurs 8.98 ms after the dropdown is initiated. Duration of this contact is approximately 2 ms;

after that, the rotor bounces back. The rotor contacts the inner race for the second time at 20.5 ms. After the third contact, at 27.06 ms, the rotor and inner race remain in continuous contact.

Figure 3.14 shows the stress history for the contact of each ball and the inner race. The theory for calculating the Hertzian contact stress is given in [71]. The stress history shows that the stresses are not uniformly distributed among the balls. After the first contact, the backup bearing experiences the highest contact stress of 2014 MPa. Then, the stresses decline and the differences in the stresses among the balls gradually decreases as the inner ring starts to rotate. The maximum Hertzian contact stress is experienced in the ball number 8, which was initially situated at 252° (Figure 3.12).
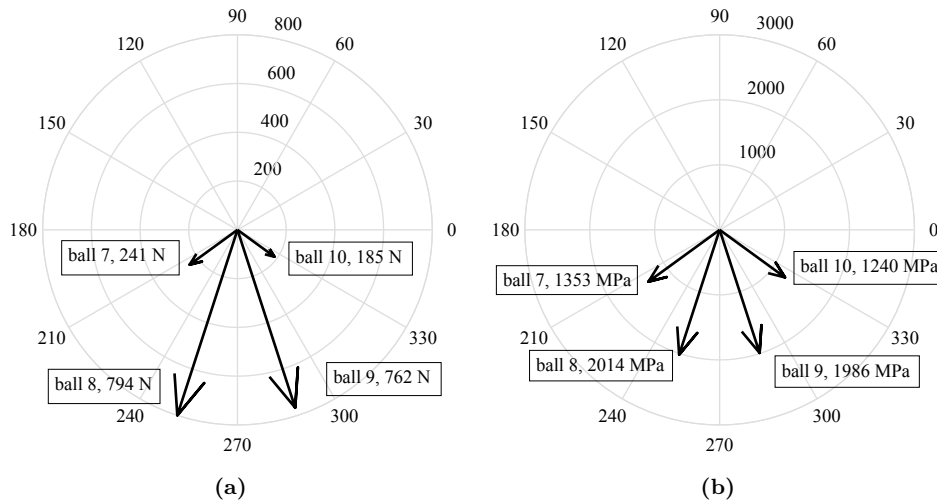


**Figure 3.15.** Distribution of load (a) and stress (b) in the backup bearing during the first contact

Figure 3.15 depicts the distribution of the load and the stress during the first contact of the rotor and the backup bearing. The maximum Hertzian stress distribution in second and third contact of the rotor and inner race is depicted in Figure 3.16.

### 3.2.2   Discussion

The backup bearing experiences the highest Hertzian stress directly after the initial rotor-bearing contact during the dropdown event. The bearing stress is not uniform during the first contact at the beginning of the simulation. The reason for this is that only a few balls are at the loaded zone during the first rotor-bearing contact. The loaded zone is formed by the ball under the horizontal center of the bearing (balls 7–10 according to Figure 3.12). In addition, the deep groove ball bearings have minor internal clearance, which contributes to the contact force distribution between an individual ball and the rings inside the bearing.
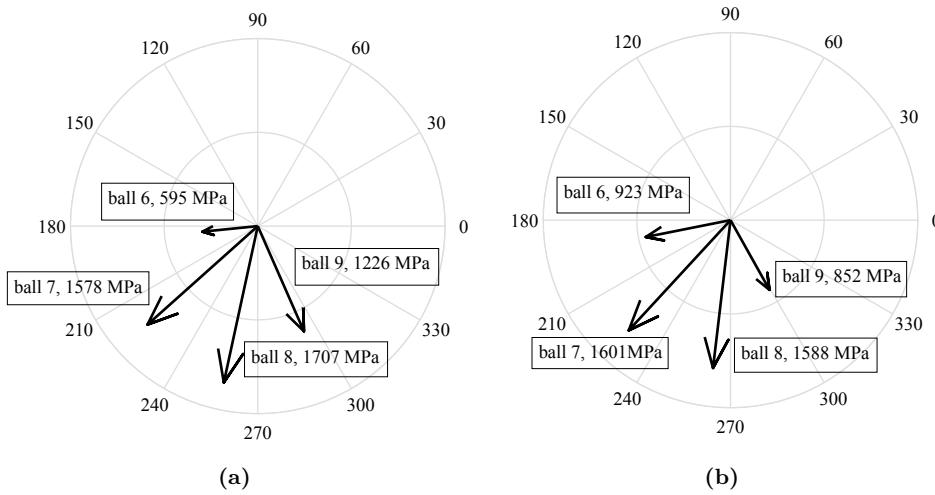
**Figure 3.16.** Maximum Hertzian stress distribution in the second (a) and third (b) contact of the rotor with the inner race

The distribution of the load and the stress during the first rotor-bearing contact is shown in Figure 3.15. During the first contact, the balls numbered 7–10 penetrate the inner race as in Figure 3.12. The locations of these balls are at phase angles 216°, 252°, 288° and 324°. The highest calculated stress is found in the contact between ball number 8 and the inner race, where the maximum contact force of 794 N is present, and the maximum Hertzian stress is 2014 MPa. The total contact force between the rotor and inner race has two components during the first contact of the rotor with the backup bearing. The vertical force component is due to gravitational force of the rotor weight. Because of the frictional contact, the friction force between the rotor and inner race is in the horizontal direction acting in the opposite direction to the rotation of the rotor. Therefore, the total contact force vector is pointing to the left towards ball number 8 (Figure 3.12).

Figure 3.16 presents the maximum Hertzian stress distribution of second and third contact of the rotor and inner race. During the second and third contacts, ball number 10 moved away from the loaded zone, and was no longer in contact with the inner race. Also, the location of the balls changed due to the friction force-induced acceleration of the inner ring. In the second contact, balls 6–9 were at 185°, 221°, 257°, and 293° phase angles, respectively, according to Figure 3.16a; and ball number 8 experienced the highest stress. In the third contact, balls 6, 7, 8 and 9 moved to 191°, 227°, 263° and 299° phase angles, according to Figure 3.16b; the highest stress was found in the contact between ball number 7 and the inner race. The simulation reveals that different balls were in contact with the inner race at various times as the bearing inner ring accelerated, due to the frictional forces induced by the rotor-bearing contact during the rotor dropdown event. Furthermore, the stress magnitude and the location of the ball with the

highest stress changed due to the rotation of inner ring and consequently due to the rotation of the balls in the bearing.

## 3.3   Rotors with internal contacts

Studies in this section are based on the use of the 3D solid element modeling approach for rotors having contacts. These results are based on [91]. The experimental results of manufactured test shafts having shrink-fitted joints are compared against the results generated using the proposed contact modeling method given in Section 2.2.5. The accuracy the constraint equation methods used for contact modeling between two solid bodies as well as the boundary constraints are presented and discussed. The solution routine for generating a Campbell diagram for a rotor having contact introduced in Section 2.3.1 is utilized for studying a shrink-fitted conical impeller-shaft contact and its dynamic behavior under centrifugal loads.

### 3.3.1   Experimental results of test shaft assembly

The test shaft assembly under investigation consists of a steel shaft and shrink-fitted aluminum sleeve, as shown in Figure 3.17. Certain material properties of individual components are verified by measuring mass properties and the lowest free-free natural bending mode frequencies (shafts only). For shrink-fitted joint testing purposes, three sets of test shaft assemblies are made with varying radial interferences, and then measured by means of experimental modal analysis. A scanning laser doppler vibrometer is used for modal analysis, which provides contactless measurement and does not require sensors that would add mass on the test pieces. The experimental results are shown in Table 3.6. Based on the measured first free-free natural bending frequencies, the radial interference in the shrink fit joint does not exert a significant effect on the natural frequencies of the test assemblies.

**Table 3.6.** Experimental results of various radial interferences of test shaft assemblies

| Test shaft assembly | Radial interference $\delta_{\mathrm{rad}}$ (µm) | 1. BM (Hz) | 2. BM (Hz) |
|---|---|---|---|
| 1 | 3.0 | 1105.9 | 3084.0 |
| 2 | 9.0 | 1108.2 | 3098.4 |
| 3 | 14 | 1108.6 | 3095.7 |
| Average | | 1107.6 | 3092.7 |
| Difference (max/min)[1] | | +0.09 % / -0.15 % | +0.18 % / -0.28 % |

[1] Max/min value compared against the corresponding averaged value
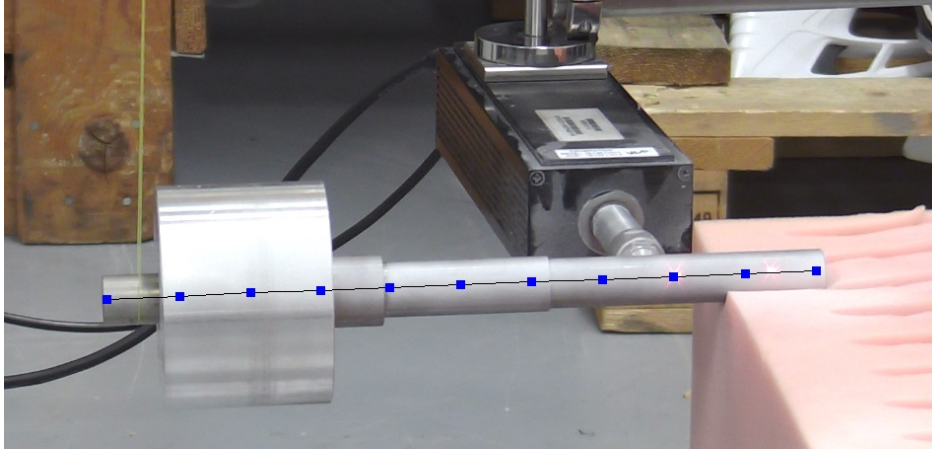
**Figure 3.17.** Test shaft assembly during experimental modal analysis

Component level verification of certain material properties was performed before assembling the shrink-fitted sleeves. Table 3.7 presents the material parameters as verified and applied in the numerical studies. The density of both materials used is verified by means of measuring the masses of all test pieces and comparing the averaged results against known volume. The known volume is taken from the corresponding computer-aided design (CAD) model. Manufactured bodies will have marginally different dimensions due to the tolerances; however, the change in volume between test pieces is considered insignificant. The same conclusion is made while comparing the volumes of the CAD body and FE mesh. The elastic modulus of S235 is verified by measuring the first natural bending mode frequencies of all shaft parts. The averaged results shown in Table 3.6 are set as a reference. The elastic modulus of S235 is found using the iteration loop in FE software (Ansys), where the elastic modulus is updated and solved subset lowest eigenfrequencies are stored. The elastic modulus of 6061-T6 aluminum was not verified. The elastic modulus used for 6061-T6 is taken from the material data sheet. Also, Poisson's ratios are based on material data sheets for both shaft and sleeve materials.

**Table 3.7.** Material parameters used with numerical studies of the test shaft assembly

| Part / Material | Density (kg/m$^3$) | Elastic modulus (GPa) | Poisson's ratio (-) |
|---|---|---|---|
| Shaft / S235 | 7812[1] | 210[1] | 0.3 |
| Sleeve / Al 6061-T6 | 2745[1] | 68.9 | 0.33 |

[1] Verified parameter

### 3.3.2   Numerical results of test shaft assembly

Based on the measured results of manufactured test shaft assemblies, the shrink
fit interference seems to have a minor impact on the free-free natural bending
frequencies. Therefore, the case of 3 μm interference is selected for numerical
studies. The FE mesh of the test shaft assembly used in the numerical studies
is presented in Figure 3.18. The mesh generator in Ansys Mechanical is used
for generating the FE mesh. The mesh consists of 36,838 ten-node quadratic
tetrahedron elements. By using a mesh imported from Ansys, possible differences
of model discretization are avoided, and differences between the two modeling
approaches are thereby minimized. The main dimensions of the test shaft assembly
are presented in Figure 3.19. The mesh size at the contact zone is 2.5 mm.
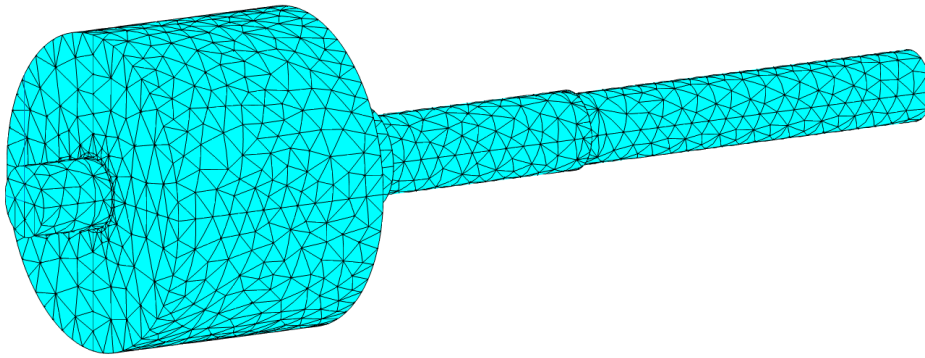


**Figure 3.18.**  FE mesh of test shaft assembly
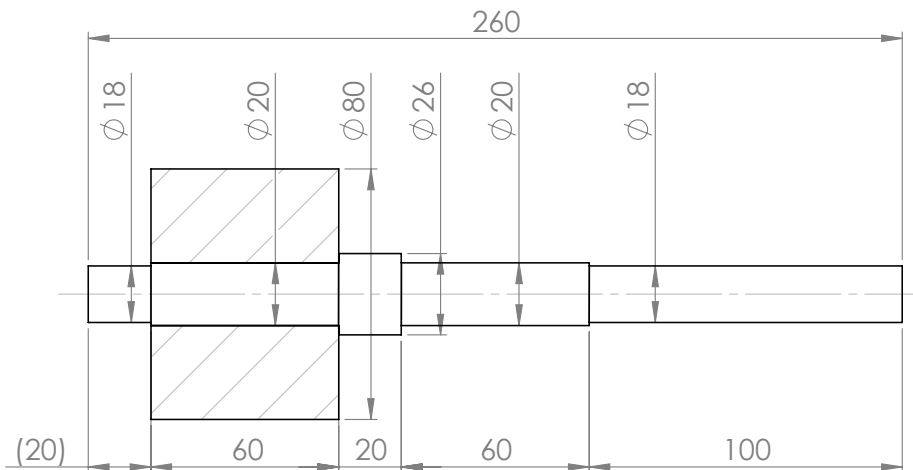


**Figure 3.19.**  Main dimensions of test shaft assembly

The numerical results are obtained using the proposed solution routine for solving
the eigenfrequencies for a rotor having contacts and using the developed custom
trial force constraint equation method. For comparison purposes, commercial

software Ansys Workbench 18 is used to model and solve the same rotor model. The contact detection used in the Matlab environment is based on the method introduced in Section 2.2.5. Only frictionless contact treatment is used in the Matlab environment. The stress-stiffening effect is explored by studying the system with and without its influence. Thermal effects are not included in any of the presented studies in this subsection.

A comparison of free-free natural BM frequencies is shown in Table 3.8. An instance of 3 μm interference is studied. In the case of the proposed solution method, results with and without the initial stress stiffening, due to shrink fit interference, are given. Results obtained using both the proposed method and Ansys with frictional contact are compared against the averaged results of the measured test shaft assemblies. The proposed method referred to here is a combination of direct node-to-node contact detection using the developed trial force constraint equation method for frictionless contact. Averaging of the measured results is justified, because the effect of radial interference in the shrink fit joint does not significantly affect the natural free-free bending frequencies of the measured test shaft assemblies. The proposed method yields fairly accurate results; though Ansys reference results yield greater error compared to the measured results. Since the material properties used are the same with both modeling approaches, logically the contact modeling is the main reason for differing results. The material properties used in both numerical modeling environments are provided in Table 3.7.

Additionally, test shaft assembly cases two and three according to Table 3.6 are studied. The results of the free-free bending frequency are calculated with the proposed method and Ansys. Between the different radial interferences, the numerical results are the same when the stress-stiffening effect was excluded. When the stress-stiffening effect was included with the proposed method, the bending frequencies increased only by 0.02%, due to increased joint interference.

**Table 3.8.** Comparison of free-free bending frequencies of test shaft assembly

|  | 1. BM (Hz) / error (%) | 2. BM (Hz) / error (%) |
|---|---|---|
| Measured (averaged) | 1107.6 / - | 3092.7 / - |
| Proposed method w/o stress stiffening | 1113.4 / +0.52 | 3147.0 / +1.76 |
| Proposed method with stress stiffening | 1113.3 / +0.51 | 3147.0 / +1.76 |
| Ansys | 1138.3 / +2.77 | 3300.8 / +6.73 |

### 3.3.3 Discussion of verification of shrink fit joint modeling

Two sets of experimental modal analyses were made; the first measurements were made for an individual part in order to identify the used material properties. The

second measurements were made for assembled shrink fitted test shaft assemblies to identify the effect of the various radial interferences used. Based on the measurement results, low radial interferences do not significantly contribute to the lowest natural bending frequencies of the structures studied. A minor increase in the first bending mode frequencies was observed, according to Table 3.6. Since the change in the first bending frequencies was, relatively, fractions of only one percent, and the frequency increase in second bending modes is inconsistent, these changes can be related to environment factors or the accuracy of the used measurement device. Averaged values of the frequencies of the two lowest bending mode are thus used for comparison with the numerical results.

All three radial interferences of the test shaft assemblies were numerically studied. When the stress-stiffening effect was excluded, no shifting was observed in the lowest bending mode frequencies. On the other hand, when pre-stress was included in the eigenvalue analysis, the greatest relative change in the bending frequencies was only 0.02%. A pre-stress condition can cause an increase in the natural frequencies of a structure. However, with these studied test shaft assemblies, the radial interference level is so low that no visible pre-stressed impact is visible.

### 3.3.4   Accuracy of contact modeling

In this section, the constraint error at the contact region achieved using the proposed contact modeling method with the trial force constraint method is presented. The constraint error magnitude is relevant in order to achieve converged results. Also, the results of the constraint error at the contact region calculated with Ansys are presented for comparison purposes. Figure 3.20 introduces the cylindrical constraints that are used as boundary conditions for the contact treatment with the proposed method. The displacements of the assembly according to Figure 3.20 are constrained as follows: radial deformation is allowed while tangential deformation is restricted. Axial rigid body movement is constrained, but axial deformations are allowed. In Ansys, a corresponding boundary constraint set is modeled using the native Cylindrical constraint tools.

For a reference solution for the constraint error analysis, the test shaft assembly is selected. Rotational speed is set to be zero in order to ensure that no external loads are present and that the contact region remains fully closed. The error of constraint equations at the shrink fitted joint contact region is presented in Figure 3.21. Cylindrical constraints, a set of constraints between the shaft body and ground, are used to prevent rigid body motion during the solution of the contact problem. The cylindrical constraint error is presented in Figure 3.22.

For comparison purposes, the multipoint constraint method, also known as the master-slave constraint method, is utilized [102]. This particular constraint method is very effective because it uses the master-slave relation and while removing the slave DOF the solution turn out to be exact. The mean constraint error with the MPC method at contact region is $-7.0304 \times 10^{-20}$ m and the cylindrical constraint mean error is $-1.1979 \times 10^{-22}$ m.

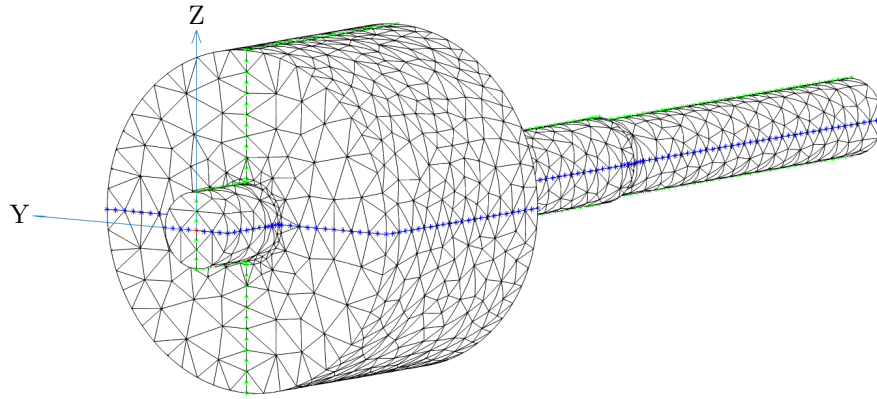**Figure 3.20.** Cylindrical constraints applied to the test shaft assembly model: red dot TX = 0 (in the origo), green dots TY = 0, blue dots TZ = 0

For further comparison, two sets of constraint errors at the contact region are calculated using Ansys. In the first case, the contact formulation used is augmented Lagrangian [103, 104]. The constraint error of this case is presented in Figure 3.23.
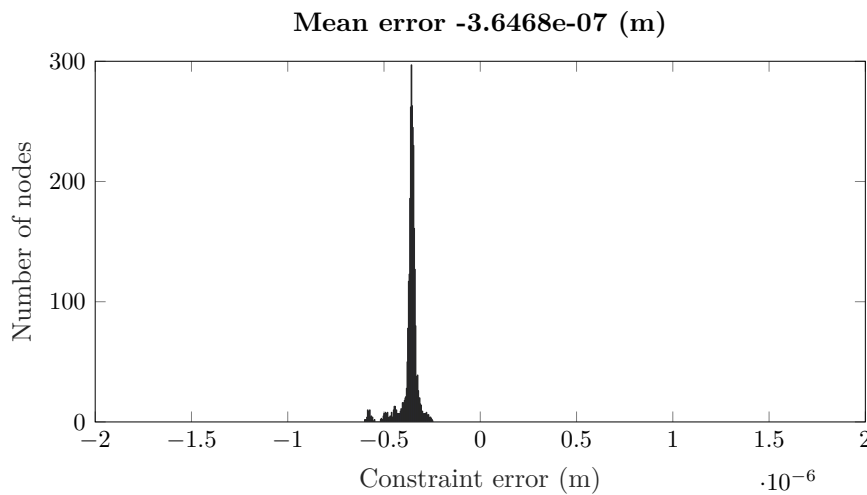


**Figure 3.23.** Constraint error at the contact region using the augmented Lagrangian method with Ansys

The other Ansys result set is presented in Figure 3.24. The contact formulation used is normal Lagrangian, which is the traditional Lagrangian method.

**Mean error -1.793e-07 (m)**
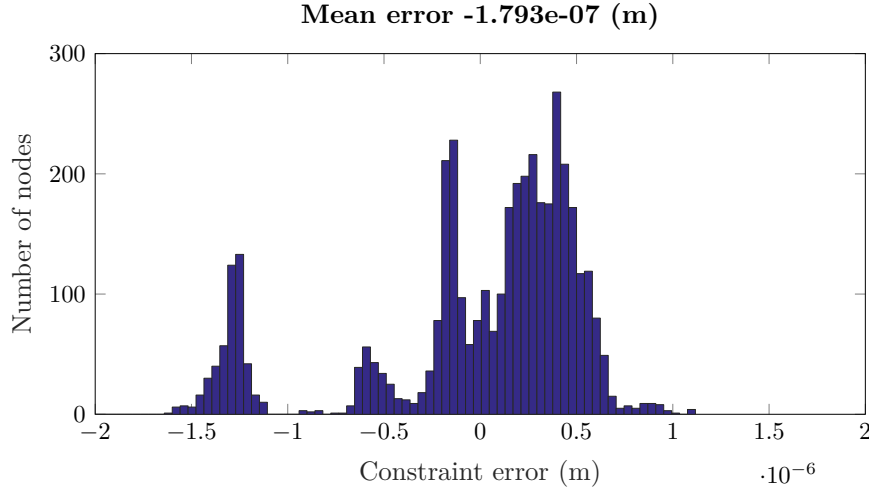


**Figure 3.21.** Constraint error at contact region using the method proposed

**Mean error -6.2776e-09 (m)**
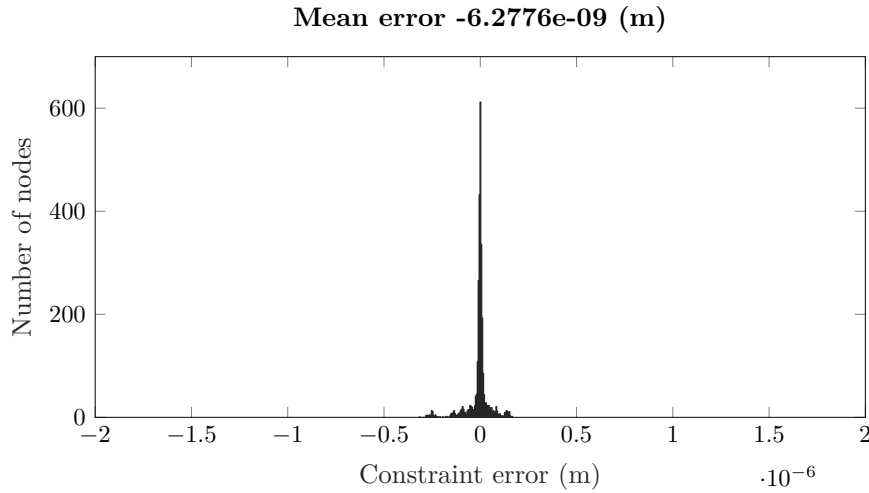


**Figure 3.24.** Constraint error at the contact region using the normal Lagrangian method with Ansys

### 3.3.5  Discussion of use of constraint equations

The proposed constraint equation method is based on the use of the contact stiffness coefficient. Therefore, it resembles the functionality of penalty function constraint equation method [102]. With this method, it is typical that the solution is not exact because of the penalty weight used, which is essentially a spring coefficient. The histogram plot of the constraint error is showing moderate scattering, though mean error seems to be relatively small. The solution required two iterations. The cylindrical constraint uses stiff springs that are connected
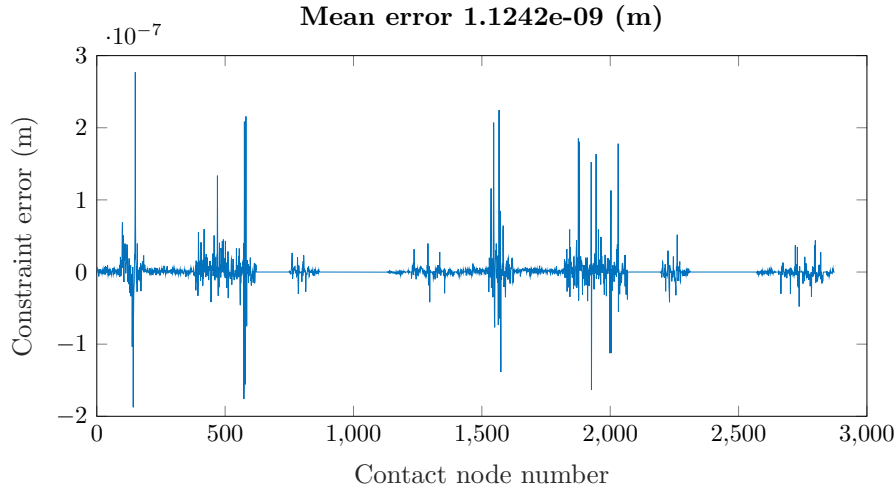
**Figure 3.22.** Cylindrical constraint error at boundary region using the method proposed

from a body to the ground. For this reason, the cylindrical constraint will also show minor constraint error.

The constraint error with the MPC method at contact region and cylindrical constraint error are both neglectablem but non-zero due to limited numerical accuracy. As mentioned before, the MPC method will yield an exact solution. The solution required only one iteration. Simultaneously, the cylindrical constraint error is negligible, since the contact forces at contact region are in balance. The slippage in the contact area in the axial direction is considered to be negligible, and is consequently not studied, using neither trial force nor MPC method.

The constraint error of the augmented Lagrangian method is presented in Figure 3.23. As noted, the augmented Lagrangian method is relatively focused, though it is not very accurate. The solution required four iterations. While using the Lagrangian method, Figure 3.24, the solution is focused and accurate. The solution required 124 iterations. When considering the computational time for obtaining the solution, Matlab can be significantly slower than Ansys. An exact value for relative speed is hard to determine, since Ansys can have constraint equation method and mesh density dependent built-in routines for sub-stepping the solution; thus, a varying number of iterations is introduced. In addition, the solver type used has its own effect on the number of iterations and computational time. Although the Lagrangian method is an exact method, the mean constraint error is significantly greater than in the case of MPC method. This is due to the fact that the Lagrangian method does not allow penetration; thus, the contact status may oscillate between closed or open status. The presence of this oscillation causes a higher number of iterations, as witnessed in this case.

The results presented regarded with to the constraint error will provide some good general understanding on how various constraint equation methods work and how accurate they are. The simplest and most accurate method, without requiring to

increase the number of DOFs is the MPC method. Although this method requires a separate transformation matrix to be formulated, it can still be considered to be one of the best constraint methods. In addition, the MPC method yields accurate results with only one iteration. The Lagrangian method, with and without the augmented part also requires an additional bordered stiffness matrix. The MPC method is also available in Ansys, though it can be used only with contacts that do remain closed, bonded and no separation; thus, it cannot be used for frictional contact. The most accurate contact option Ansys offers with the least options for tuning for frictional contact is normal Lagrangian; nevertheless, it requires a large number of iterations to yield accurate results.

### 3.3.6   Conical impeller assembly

An assembly of a conical impeller shrink-fitted on a shaft is studied. The FE mesh of the conical impeller assembly is presented in Figure 3.25. The mesh consists of 24,766 ten-node quadratic tetrahedron elements. The main dimensions of the conical impeller assembly are presented in Figure 3.26. The mesh size at the contact zone is 5.0 mm. The conical impeller of the radial kinetic compressor wheel is simplified and modeled without the blades. Thus, only the hub of the impeller is included in the FE mesh. By doing so, the FE-problem size can be reduced and the lower number of the lowest eigenmodes utilized by neglecting the low frequency local bending modes of the impeller blades. The material properties used in this study are presented in Table 3.9.
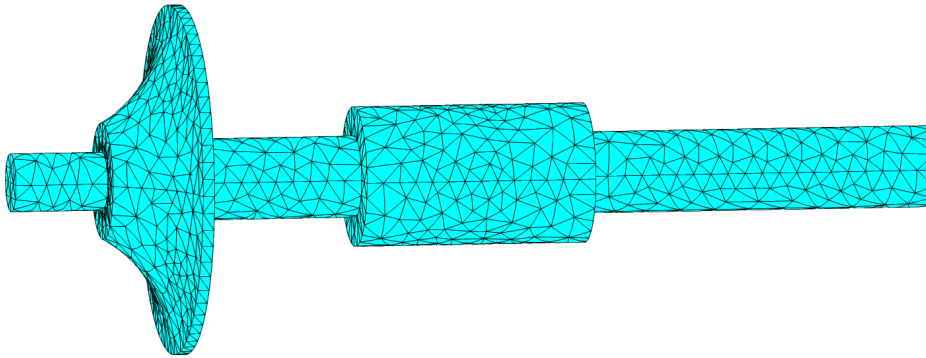


**Figure 3.25.** FE mesh of conical impeller assembly

Two simple identical bearings, essentially spring-damper elements, are located at both ends of the shaft of the conical impeller assembly and connected to the surfaces of the end planes of the shaft. The stiffness and damping parameters used are presented in Table 3.10. The studied speed range is from zero to 30,000 rpm, with an increment of 1000 rpm. The radial interference in the conical impeller-shaft shrink fit is 50 μm.
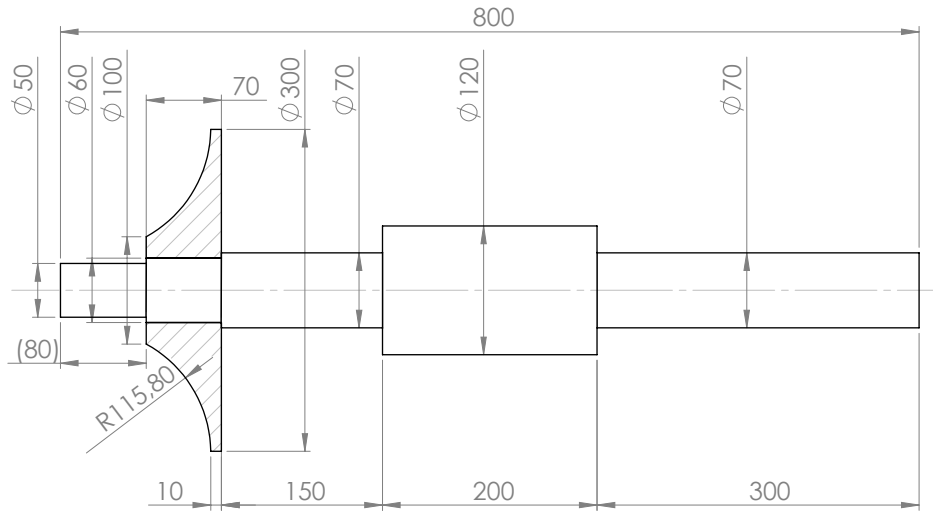
**Figure 3.26.** Main dimensions of conical impeller assembly

**Table 3.9.** Material parameters used in numerical studies of the conical impeller assembly

| Part / Material | Density $(kg/m^3)$ | Elastic modulus (GPa) | Poisson's ratio (-) |
|---|---|---|---|
| Shaft / Steel | 7850 | 200 | 0.3 |
| Impeller / Aluminum | 2810 | 71.7 | 0.33 |

**Table 3.10.** Bearing properties used in the conical impeller assembly

| Bearing | Stiffness | | Damping | |
|---|---|---|---|---|
| | (N/m) | (N/m) | (Ns/m) | (Ns/m) |
| 1 | $1 \times 10^8$ | $1 \times 10^8$ | $1 \times 10^3$ | $1 \times 10^3$ |
| 2 | $1 \times 10^8$ | $1 \times 10^8$ | $1 \times 10^3$ | $1 \times 10^3$ |

This particular simplified conical impeller-shaft construction is selected because the impeller-shaft shrink-fitted joint will partially open as the centrifugal forces increase due to the increased spin speed. Partially opened contact region is illustrated in Figure 3.27, the deformations are amplified for visualization purposes. The contact area will decrease, while operating rotational speed increases. This will cause a reduction of bending stiffness in this particular assembly.
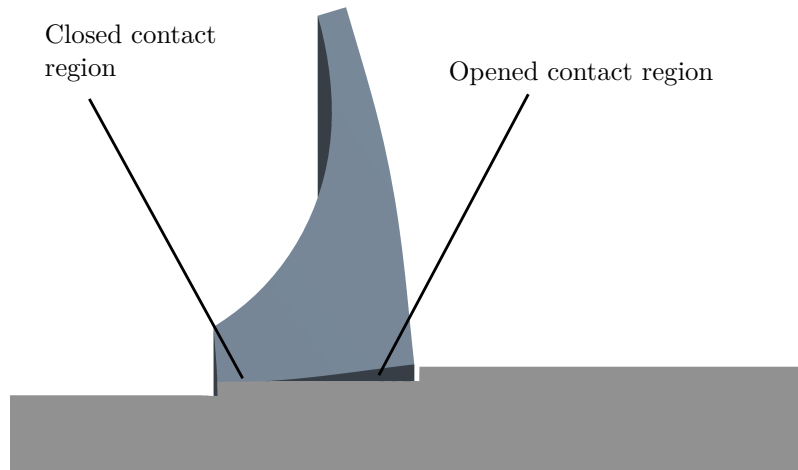
**Figure 3.27.** Visualization of contact region partial opening between the conical impeller and shaft

**Table 3.11.** First whirling mode frequencies at 30,000 rpm of the conical impeller assembly

|  | At 30,000 rpm | |
| --- | --- | --- |
|  | 1. BW (Hz) | 1. FW (Hz) |
| Proposed method w/o stress stiffening | 161.1 | 171.1 |
| Proposed method with stress stiffening | 168.6 | 176.8 |
| Proposed method with fixed contact | 165.5 | 173.3 |
| Ansys | 166.4 | 173.9 |

Campbell diagram of the conical impeller assembly without the stress-stiffening effect is presented in Figure 3.28, and the critical speeds of forward whirl (FW) and backward whirl (BW) modes are given. The effect of partially opened contact is present in the Campbell diagram, as the overall bending stiffness of the assembly starts to decline at 15,000 rpm. A Campbell diagram of the conical impeller assembly with stress-stiffening effect is presented in Figure 3.29. The stress-stiffening effect will not yield a significant stiffening effect on the bending modes.

For comparison purposes, the Campbell diagram of the conical impeller assembly with fixed contact is presented in Figure 3.30. The initial interference in the shrink fit joint is not present, and the stress-stiffening effect is neglected. Since the contact is fixed, the effect of bending stiffness reduction due to the reduced
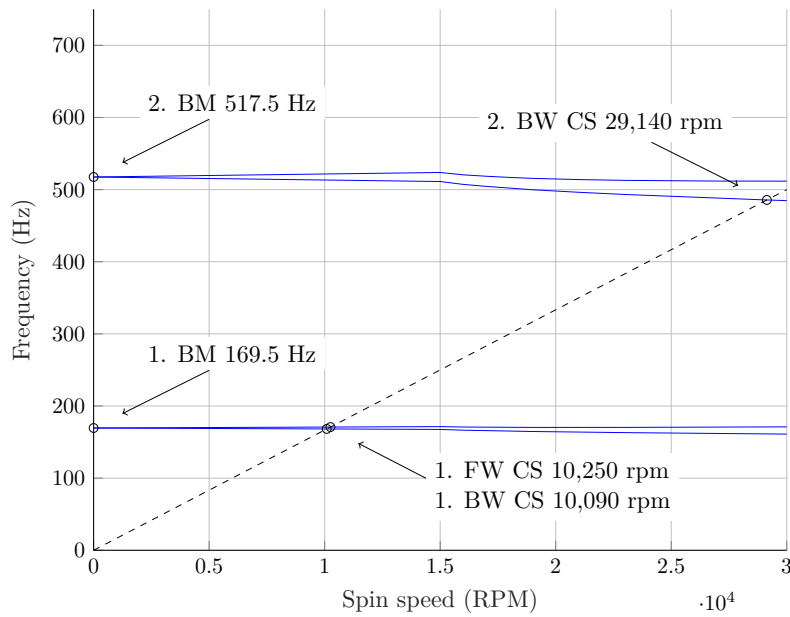
**Figure 3.28.** Proposed method: the Campbell diagram without stress stiffening of the conical impeller assembly

contact area, this resulting from the partially opened contact, is not present in the Campbell diagram. The Campbell diagram generated in Ansys is presented in Figure 3.31. Both the fixed joint results in Figure 3.29 and the Ansys results behave very similarly without having any indication of reduced bending stiffness due to partially opened contact between the impeller and shaft.

**Table 3.12.** Second whirling mode frequencies at 30,000 rpm of the conical impeller assembly

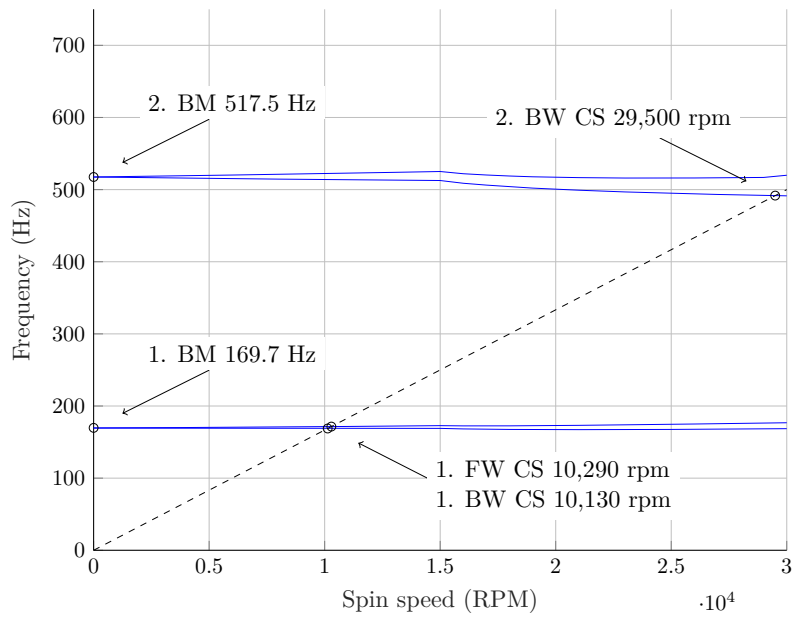|  | At 30,000 rpm | |
|  | 2. BW (Hz) | 2. FW (Hz) |
| --- | --- | --- |
| Proposed method w/o stress stiffening | 484.7 | 511.7 |
| Proposed method with stress stiffening | 491.4 | 519.9 |
| Proposed method with fixed contact | 505.0 | 530.0 |
| Ansys | 508.0 | 533.4 |

**Figure 3.29.** Proposed method: the Campbell diagram with stress stiffening of the conical impeller assembly
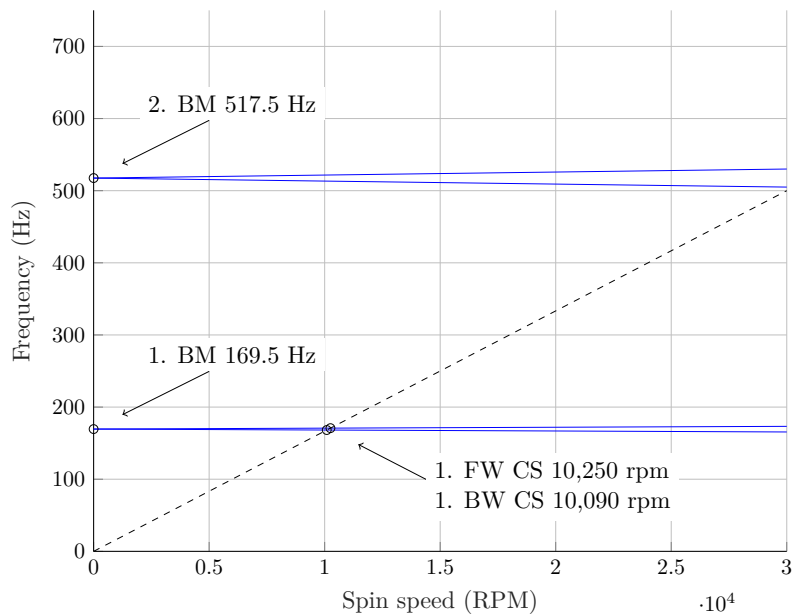


**Figure 3.30.** Proposed method: the Campbell diagram of the conical impeller assembly using fixed contact
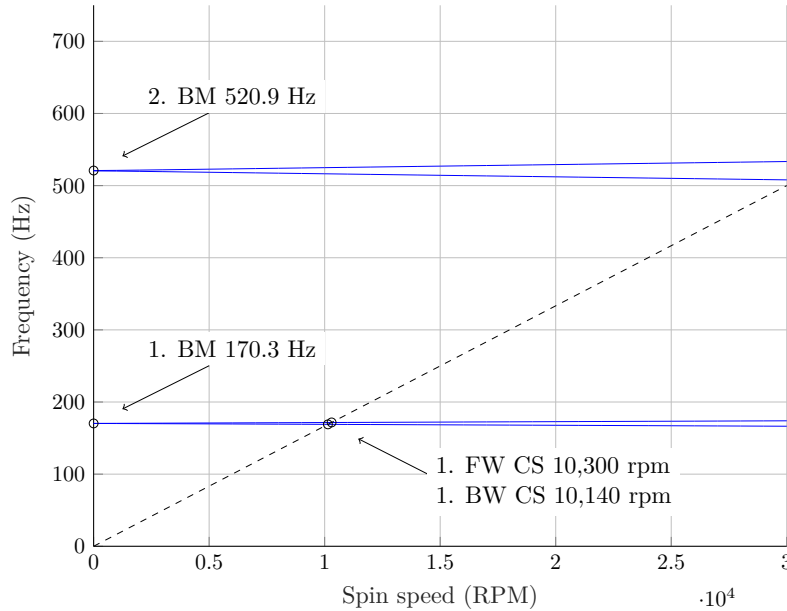
**Figure 3.31.** Ansys Campbell diagram of the conical impeller assembly using frictional contact

### 3.3.7 Effect of geometric nonlinearities to the critical speeds

With the conical impeller assembly, the first two bending modes are visible in the Campbell diagrams (Figures 3.28–3.31). The first BW and FW critical speed of Ansys is consistently 50 rpm greater than the ones with the method being proposed. In addition, the results obtained using the proposed method with the stress-stiffening effect are actually the same as the Ansys model frequencies. Since the contact treatment is applied on every speed step while using the proposed method, the contact opening is taken into account. The use of any particular constraint equation method does not contribute to the contact opening: only the external forces – in this particular case, the centrifugal force – will contribute to the opening of contact. Constraint equations are utilized after the contact status is solved, and used for the remaining contact area where the contact remains closed. Due to reduction in the contact surface area owing to high-speed operation, a dip in the mode lines in the Campbell diagrams (Figures 3.28–3.29) is present. Only the models with frictionless contact using the proposed solution routine experience the second BW mode in the speed range studied. The stress-stiffening effect increases the second BW critical speed by 360 rpm.

The reason for a rather large reduction in whirl mode frequencies of the second bending mode using frictionless contact is explicable due to the BM shapes of the supported structure. The two lowest zero speed bending modes of the supported conical impeller assembly are illustrated in Figure 3.32 using Paraview visualization software. The node points of the first bending mode are at bearing
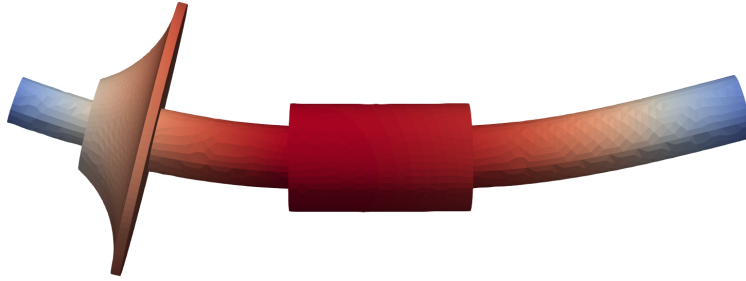
(a) First BM of the supported conical impeller assembly at zero speed
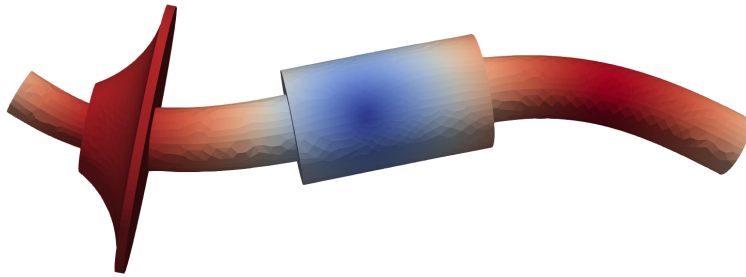


(b) Second BM of the supported conical impeller assembly at zero speed

**Figure 3.32.** Lowest BMs of the supported conical impeller assembly at zero speed

locations. In the case of the second bending mode, the third node appears roughly at the center of the structure. Because the impeller-shaft joint is located roughly one quarter of the assembly length away from the other end, the joint is roughly located at the position of highest amplitude of the second bending mode. In addition, the bending deformation of the shaft is at the highest in the location of the impeller, and the decreasing bending stiffness exerts a significant effect in this particular mode.

The frequencies of zero speed-supported conical impeller assembly are all very consistent. In Tables 3.11 and 3.12, the whirling mode frequencies at 30,000 rpm are compiled. At 30,000 rpm, the first whirling mode frequencies are roughly the same, while the proposed contact method with stress-stiffening yields the highest frequencies. The second whirling modes solved using frictionless contact method with the proposed solution routine are no longer comparable to the Ansys results, due to partially opened contact; therefore, we find reduced overall bending stiffness in the conical impeller assembly. An interesting observation is that the Ansys model with frictional contact behaves very similarly to the model using the proposed solution routine with fixed contact.

The partially opened contact between the conical impeller and shaft can reduce the whirling mode frequencies. When comparing the second bending mode frequencies the backward mode will decline 18.5 Hz on average, and the forward mode by 15.9 Hz on average. The stress-stiffening effect will increase the stiffness of shaft and conical impeller in proximity of the contact region. Regardless, the total

stiffness of this structure is dominated by the robustness of the conical impeller-shaft joint. Since the contact is partially opened at 30,000 rpm, the total stiffness of the structure is reduced even when the stress-stiffening effect is included. By comparing the forward and backward mode frequency difference at full speed, the gyroscopic effect will also increase due to contact opening by an average of 10.1%.

## 3.4 Thermal stress studies

A traction motor application is under investigation in this section. Thermal and mechanical stress history respective to the rotor of the traction motor is calculated using finite element software (Ansys). These results are based on [92]. The general solution routine for coupled thermal mechanical analysis used is introduced in Section 2.3.2. The transient thermal study done in Ansys is based on the heat transfer theory introduced in Section 2.1.4. The solved temperature distribution is utilized as an initial thermal expansion force vector in the structural analysis. The thermal expansion force vector theory 3D solid element approach is formulated in Section 2.1.2. Finally, the solved thermal mechanical stress history is used to calculate the fatigue life of the rotating structure studied, based on the theory suggested in Section 2.3.3.

### 3.4.1 Thermal stress analysis of traction motor

The thermomechanical solution routine is applied to a three-phase sixteen-pole double-deck embedded permanent magnet traction motor. This traction motor is originally designed for a full electric sports car Electric RaceAbout, the details of which are found in [75]. The main dimensions of the electric machine are provided in Table 3.13.

**Table 3.13.** Main parameters of the analyzed PMSM

| Parameter | Value |
| --- | --- |
| Stator tooth width | 11.6 mm |
| Stator slot height | 32.5 mm |
| Stator outer diameter | 380 mm |
| Stator bore diameter | 287 mm |
| Active stator stack length | 65 mm |
| Active rotor stack length | 68 mm |
| Rotor outer diameter | 284.2 mm |
| d-axis air gap length (min) | 1.4 mm |
| q-axis air gap length (max) | 5.5 mm |
| Width of the upper magnet | 47.9 mm |
| Width of the lower magnet | 43.9 mm |
| Thickness of the upper magnet (max value) | 8.5 mm |
| Thickness of the lower magnet | 6 mm |

The structure of a single pole of the analyzed PMSM is depicted in Figure 3.33. As presented in [75], the majority of the electric machine losses occur in the stator windings. In order to obtain proper cooling for the stator, the cooling of the PMSMs is carried out by combining force air cooling in the air gap region and liquid cooling in the stator frame. Most of the Joule and stator iron losses are removed by liquid cooling, and the rotor surface is cooled by forced air cooling. Because of this, the machine can be regarded as the open type.
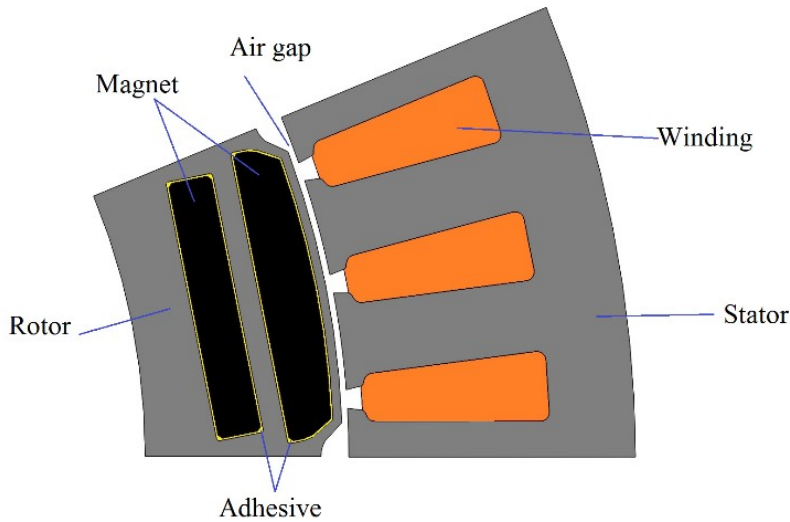


**Figure 3.33.** Structure of one pole of the analyzed PMSM

The input for the thermomechanical analysis consists of the torque and rotational speed from the machine drive cycle and the corresponding thermal loads. All the input variables are entered as a function of time. In the studied case, the measured data from the Nürburgring Nordschleife race track according to [75] is used as a drive cycle. The measured rotational speed, torque, voltage and current on the rear left electric motor during one race track lap are presented in Figure 3.34.

The thermal loads within the drive cycle – that is, the iron losses in the rotor laminations and the eddy current losses in the permanent magnets – were calculated by 2D FEM. The eddy current losses in the permanent magnets were calculated by treating them as short-circuited solid conductors in the transient FEA. Rotor iron loss calculation was performed using a loss-surface model, which was implemented in the Flux2D software package by Cedrat. The loss calculation was performed at 1000 rpm by applying transient FEM for a whole useful torque region, from zero to break-down torque. Temperature effects on the electromagnetic performance were not taken into account. Because eddy current losses are proportional to frequency squared, the losses at any measured rotational speed and torque point can be calculated as based on the previous loss calculation performed at 1000 rpm, using the following relation:
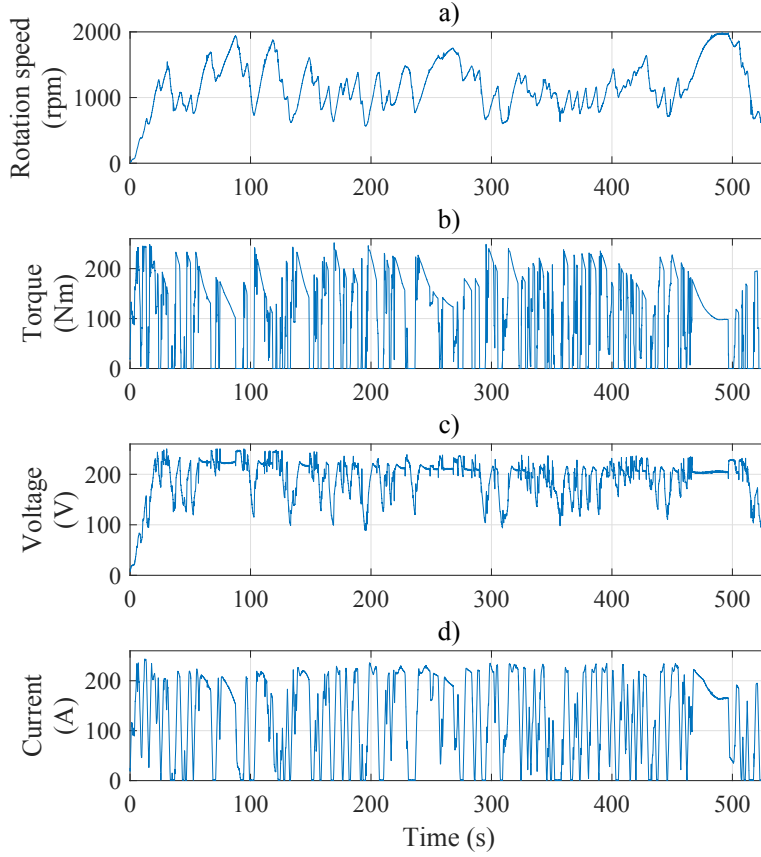
**Figure 3.34.** Measured track data: a) rotational speed (rpm), b) torque (Nm), c) voltage (V), and d) current (A) [75]

$$P\left(n_{\mathrm{rpm}}, \tau\right) = \left(\frac{n_{\mathrm{rpm}}}{1000rpm}\right)^2 P\left(1000rpm, \tau\right) \tag{3.1}$$

where $P\left(n_{\mathrm{rpm}}, \tau\right)$ is the eddy current loss at a rotational speed of $n_{\mathrm{rpm}}$ rpm and a torque of $\tau$, and $P\left(1000rpm, \tau\right)$ is the calculated eddy current loss at 1000 rpm with $\tau$. The rotor iron losses remain at a very low level in the studied rotational speed range because of the synchronous operation. At the nominal point, at a speed of 1000 rpm and torque 240 Nm, the rotor iron losses are 5.3 W and the permanent magnet eddy current losses are 84.4 W, respectively. At 2000 rpm and 240 Nm, the rotor iron losses 7.3 W and the permanent magnet eddy current losses are 337.6 W. The major share of permanent magnet eddy current losses occur in the upper magnet.

The coupled thermomechanical analysis was performed using 3D FEM in Ansys

software. The 3D model is limited exclusively to the rotor structure because of the computational effort required for a coupled transient thermal and mechanical study of this size. This is justified for the following reasons. The stator losses are removed effectively by combined forced air and liquid cooling, and thus the effect of the stator losses to the thermal state of the rotor can be neglected. The rotor losses are removed by convection to the air flow in the rotor-stator air gap, which is modeled using convection boundary constraint set to the outer surfaces and the ends of the rotor structure. Because of the relatively low rotor losses and the short active rotor stack length, the cooling air heating in the air gap can be neglected in order to simplify the analysis. Therefore, the ambient temperature of the cooling air applied to simulation is constant. The model can be further reduced by taking advantage of the axial and circular symmetry. There is a periodicity at the edges of the rotor poles due to of the equal power loss density and identical cooling conditions. Therefore, only one rotor pole needs to be modeled. In the axial direction of the rotor structure, the thermal loads and cooling conditions are identical, making it possible to simplify the model also in the axial direction. Based on the symmetry used, the 3D model shown in Figure 3.35 comprises 1/32 of the full rotor stack.
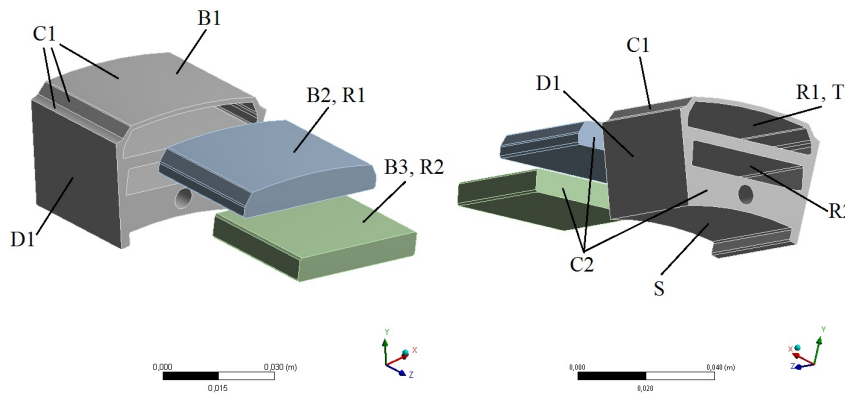


**Figure 3.35.** A 3D model of the rotor of a traction motor used in thermomechanical analysis, including utilized loads and boundary conditions

The loads and boundary conditions applied to the model are illustrated in Figure 3.35. In the transient thermal model, the electrical losses as thermal loads are inserted into volumes B1, B2, and B3, as volumetric heat generation as a function of time. The convective heat transfer boundary condition from the outer surface of the rotor to the air gap flow is inserted to surfaces marked as C1. The convection film coefficient is dependent on the medium velocity; it is thus dependent on the rotational speed. Similarly, the boundary condition describing axial convection heat transfer set to surfaces marked as C2 is rotational speed dependent. The air temperature of the air gap cooling air is set to correspond to the ambient temperature of 22°C, and it is assumed to be constant throughout the drive cycle. In the thermal model, magnets and rotor iron are modeled using their thermal conductivity, specific heat, and density. Adhesive layers typically applied

between the magnet and lamination are ignored in the model geometry, but the effect of the adhesive layer is included in a form of thermal contact resistance between contact surfaces R1 and R2. The result from the transient thermal study is the nodal temperature distribution within the rotor structure, which is utilized as an initial thermal strain in static structural analysis in Ansys.

In the mechanical analysis the centrifugal force due to the rotational speed is applied to all solid bodies (B1, B2 and B3) using the measured rotational speed of the race track. The axis of rotation in the model is located at the center point of surface S. The contact between the permanent magnet and rotor iron is modeled as mechanical body-to-body contacts, set to surfaces R1 and R2. In Ansys, the no separation contact model was applied, because it allows a minor slip but, at the same time, will ensure that the contact between magnet and the rotor iron remains closed. This particular contact type was considered because it is known that the contact must remain closed all the time: thus, solving the contact status can be faster than with the frictional contact model. Circular symmetry constraints are applied to the surfaces marked as D1 in order to prevent tangential displacement, but at the same time it allows radial and axial displacement. Axial displacement constraint for the axial symmetry condition is applied to axial boundary surfaces C2.

Alongside the geometrical symmetry used, the finite element mesh is optimized in order to minimize the computational time. In the thermal model, a coarser mesh was acknowledged as yielding essentially the same converged results as the denser mesh. Because of the transient nature of the study, the coarse mesh was utilized. In the mechanical study, denser mesh is a standard requirement. Therefore, denser mesh was utilized in the mechanical model. Additional mesh biasing was implemented in the highest stress locations shown in Figure 3.37.

Because the biased FE mesh and circular symmetry constraints are used, the effect of torque is modeled as a tangential force set to surface T. The axis of axial direction in the cylindrical coordinate system used is aligned in accordance with the same axis of rotation as in the case of centrifugal force. The material properties used in the thermomechanical analysis are shown in Table 3.14. The data is obtained from supplier online material.

### 3.4.2   Thermal stress results

Figure 3.36 shows the calculated highest temperature in the rotor model located in the upper magnet and the measured temperature from the stator windings. The scales of the temperatures are clearly different, because the temperature rises up to 145°C in the windings and the rotor temperature to only 47°C.

The relative temperature increase is compared against the measurements shown in Figure 3.36. Overview of the maximum stress areas found in the stress analysis are located in the magnet pocket upper fillet, as seen in Figure 3.37. Besides the combined thermal mechanical stresses, the stresses induced by individual loads are studied. In Table 3.15, the maximum stress during the drive cycle history of

**Table 3.14.** Material parameters of the rotor components

| Material property | Magnets (Neorem753A) | Steel (M270-50A) | Adhesive |
|---|---|---|---|
| Density $(kg/m^3)$ | 7600 | 7650 | 1207 |
| Young's modulus (MPa) | 150,000 | 200,000 | - |
| Poisson's ratio | 0.24 | 0.3 | - |
| Yield strength (MPa) | 75 | 470 | - |
| Ultimate strength (MPa) | 290 | 585 | - |
| Specific heat (J/(kg C)) | 450 | 460 | 1173 |
| Thermal expansion (1/K) | 6e−6 | 1.2e−5 | - |
| Thermal conductivity (W/(m K)) | 8.5 | 39 | 0.3 |
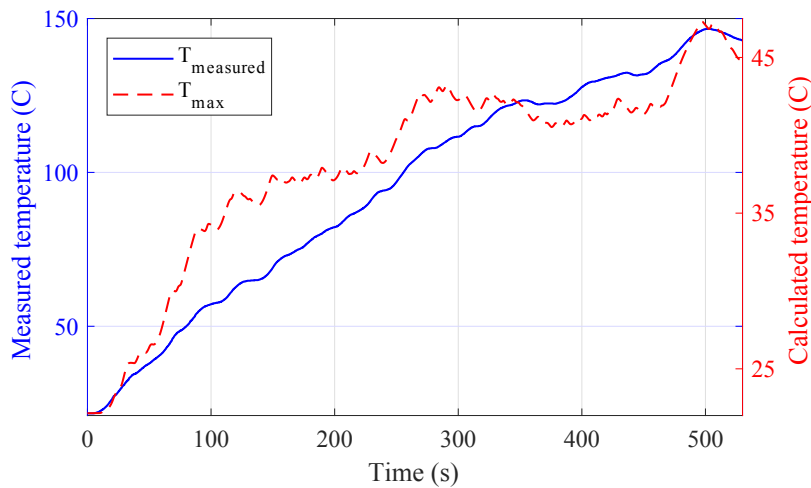


**Figure 3.36.** Measured stator winding temperature vs. calculated rotor temperature

each loading case studied is presented, along with the corresponding design safety factor. The safety factors are calculated against the lamination material yield strength shown in Table 3.14.

The maximum von Mises stress caused by mechanical, thermal, and combined loads during the studied load cycle are presented in Figure 3.38. The curves are sketched with a black dotted line, red dashed line and blue solid line, respectively. The mechanical stress consistently follows the rotational speed of the rotor. The tangential forces caused by the torque play a minor role, whereas the centrifugal force is the main contributor to the mechanical stress. During the drive cycle, the maximum mechanical stress does not exceed 43 MPa. The maximum temperature difference over the simulated time is presented in Figure 3.39.

For better visualization, the stress and temperature distributions in the FE model during the load cycle are presented in Figures 3.40–3.42 at time steps 100 s, 280 s
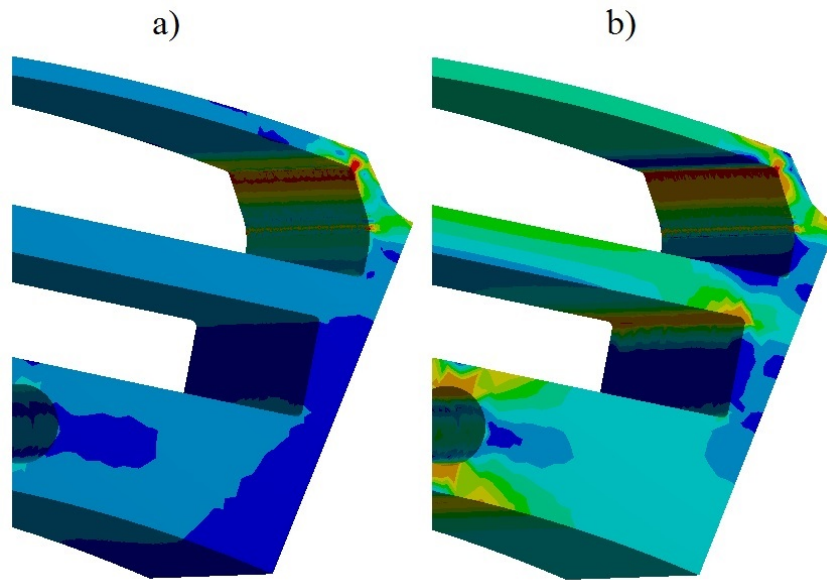
**Figure 3.37.** Rotor von Mises stress distribution: a) thermal stress only and b) centrifugal stress only

**Table 3.15.** Maximum stress and safety factor in cases A–F having different load conditions: A – centrifugal forces, B – thermal loads, C – electromagnetic torque, D – electromagnetic radial force, E – angular acceleration, F – all loads combined

| Load type | A | B | C | D | E | F |
|---|---|---|---|---|---|---|
| Max stress (MPa) | 43 | 56 | 4.2 | 2.8 | 0.013 | 80 |
| Safety factor | 11 | 8.5 | 110 | 170 | 36,000 | 5.9 |

and 500 s. The contour limits for both temperature and the von Mises stress figures are selected in a way that makes the comparison of results easy. As time increases, the temperature growth is clearly visible; though the growth in stress is not that visible due to the local peak stress located in the upper magnet pocket fillet and the generally low stress level.

When considering the behavior of separate mechanical and the thermal stresses, it can be seen that the loading condition of the motors increases the level of both stress types. However, this is not the whole truth if the stresses are observed separately and the total stress level is considered by adding these stress components together using the superposition principle. In general, as shown in Figure 3.38, the thermal stresses increase the base level of the combined stresses. The stress variation in the combined stress curve is caused by the mechanical stresses. When comparing the fluctuation of the mechanical stress and combined stress curves, it is shown that, during the drive cycle, the mechanical stresses experience more drastic changes. The residual thermal stresses clearly elevate the combined stress
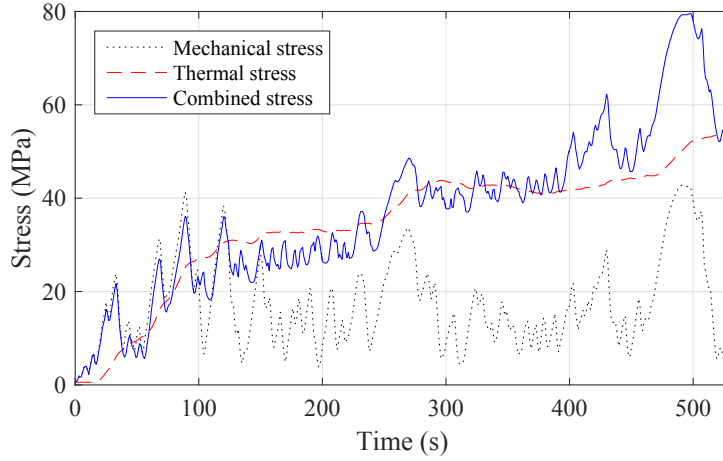
**Figure 3.38.** Von Mises stress history in magnet pocket upper fillet with different loading conditions: pure mechanical load, pure thermal load and combined load

peaks. Thermal and mechanical stresses have different dominating multiaxial stress components. For this reason, within a certain period over the stress history, these stresses combined are actually less than the thermal stresses alone.

According to Figure 3.37, the critical area where the maximum stress occurs is the uppermost corner. Using Equations (2.123) and (2.124) the equivalent stress $\Delta\sigma_{\mathrm{eq}}$ and the number of cycles $N_f$ are calculated and shown in Table 3.16. A comparison between the equivalent stresses $\sigma_{\mathrm{eq}}$ calculated for the fatigue study and maximum von Mises stresses in the drive cycle $\sigma_{\mathrm{max}}$ caused by mechanical, thermal and combined loads is illustrated in Figure 3.43. Based on the published fatigue test results for a similar rotor laminate material in [31], the following fatigue strength coefficient, fatigue strength exponent and S-N curve slope for the machine cut edges are adopted in this study: $\sigma'_f = 673.25$ MPa, $b_e = -0.09559$ and $\beta = 3$.

**Table 3.16.** Fatigue analysis results of three different load conditions

| Stress type | Mechanical | Thermal | Combined |
|---|---|---|---|
| $\Delta\sigma_{\mathrm{eq}}$ (MPa) | 100 | 76.4 | 256 |
| $N_f$ ($1 \times 10^6$ cycles) | $3.2 \times 10^5$ | $5.5 \times 10^6$ | 17 |

### 3.4.3   Discussion

The calculated highest temperature point in the rotor model located in the upper magnet as well as the measured temperature from the stator windings are shown in Figure 3.36. The trends of the curves can be compared with each other, even though the temperatures are obtained from different locations. The calculated
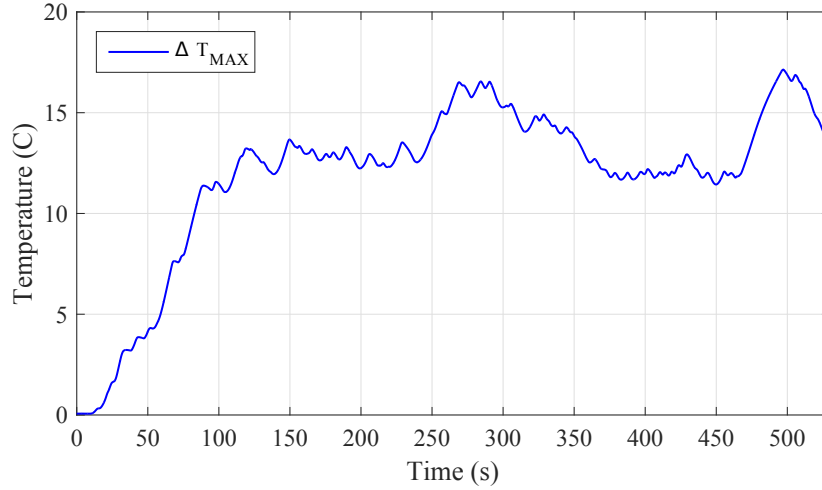
**Figure 3.39.** The maximum temperature difference of the FE model during the simulation



**(a)** Temperature distribution at 100 s    **(b)** Stress distribution at 100 s
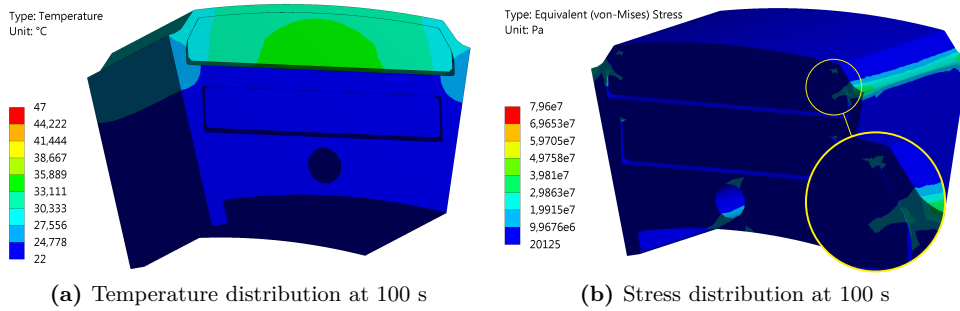
**Figure 3.40.** Rotor temperature and stress distribution at 100 s

temperature increases rapidly between 70 and 100 s. The temperature in the rotor model increases more slowly than in the windings after 100 s. After the time point of 240 s, the rotor temperature starts to increase faster than the temperature in the windings. At the time point 280 s, the rate of temperature increase becomes slower again, until the final rapid increase directly before the end of the cycle.

The relative temperature increase is compared against the measured temperature data in Figure 3.36. Based on the comparison, the faster temperature increase in the rotor is related to driving at full throttle, which can be obtained from the rotational speed curve in Figure 3.34. Based on this finding, the temperature increase in the rotor lamination is highly dependent on the loading of the motor. The windings are indirectly cooled by liquid cooling. Because of this, the temperature change in the windings is steadier along the drive cycle than in the rotor. Based on the general trend of constantly increasing temperature from beginning till the end of the drive cycle, it appears that the motor has not
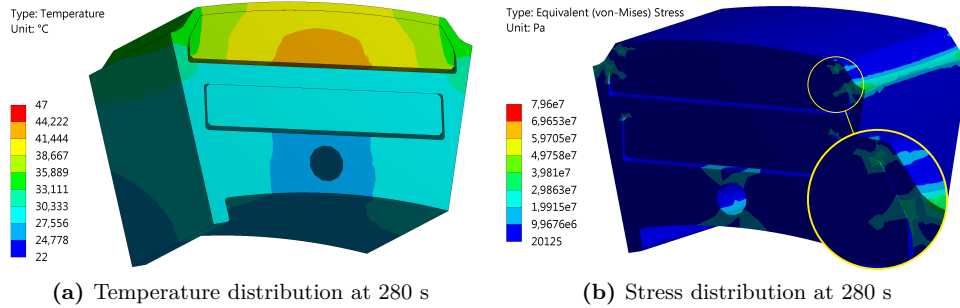
**(a)** Temperature distribution at 280 s



**(b)** Stress distribution at 280 s

**Figure 3.41.** Rotor temperature and stress distribution at 280 s



**(a)** Temperature distribution at 500 s



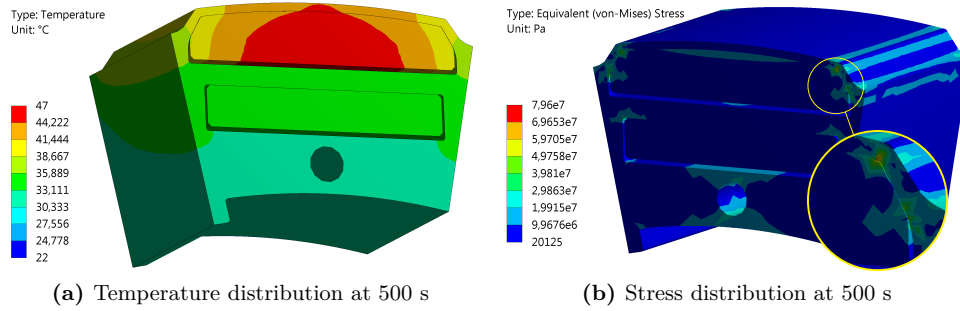**(b)** Stress distribution at 500 s

**Figure 3.42.** Rotor temperature and stress distribution at 500 s

yet achieved the steady state condition. Due to the short single drive cycle, multiple repeated drive cycles may be required in order to achieve roughly the thermal steady state condition; though performing a single drive cycle with full performance of the vehicle consumes most of the energy storage capacity and thus performing multiple drive cycles repeatedly is not possible. For this reason, the temperature curves start from the ambient temperature, and this single drive cycle data is justified for use in fatigue analysis.

A general overview of the maximum stress areas found in the stress analysis is presented in Figure 3.37. The highest stress concentration is found in the magnet pocket upper fillet. Furthermore, the magnetic flux is denser around the air barriers in the magnet housing of the lamination bod; thus, more eddy currents are induced in regions where the high levels of stress are found in the structure [67]. This stress parallax emphasizes the importance of including the thermal effects in structural analysis. The equivalent stress is calculated in order to observe the stress fluctuation.

In Table 3.15, the stress proportions of the different load types are compiled. The stress results are calculated using the full drive cycle data as the basis and applying one particular load component at a time. The dominating force components are mechanical and thermal forces, as expected. In this traction
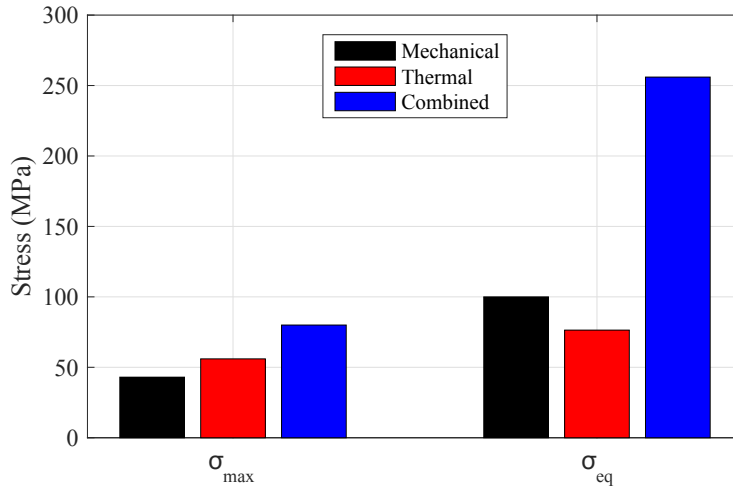
**Figure 3.43.** Comparison of the stress levels caused by different load conditions

motor case, the mechanical design is very conservative and the highest stress caused by centrifugal force is unexpectedly low for a traction motor application – only 43 MPa. When evaluating the magnitudes of different force types, the electromagnetic forces clearly have a minor role. In addition, the stress caused by angular acceleration is remarkably low, and in comparison to other loads, it is negligible. In Table 3.15, the safety factors against the lamination material yield strength of 470 MPa are calculated, which is shown in Table 3.14. The safety factor of angular acceleration becomes excessive because of the extremely low level stress caused by this particular load. The combined thermomechanical stress is obviously greatest. Because of the appearance of different multiaxial stress components – mainly due to mechanical and thermal loads – the evaluated von Mises stress is lower than the sum of the individual stress components.

In general, the thermal stresses presented in Figure 3.36 follow the temperature curve. Because of the temperature gradient along the structure, thermal stresses appear. Losses of magnets increase when the load of the motors is increased, which causes a higher temperature gradient. The thermal stresses increase faster during the time spans when the structure experiences a faster temperature increase (70–100, 240–280 and 475–500 s). Temperature increase becomes steadier at higher temperatures. This is because the structure heats up more uniformly, which results in a lower temperature gradient and minor increase in the thermal stress levels.

The maximum temperature difference over the simulated time is pretested as showns in Figure 3.39. The maximum temperature increases fast during these previously discussed time spans 70–100, 240–280 and 475–500 s. During these time spans the maximum temperature difference is also increasing rapidly, and the heat generation inside the structure is fast; though the heat conduction to

the outer surface of the structure occurs more slowly. Therefore, when losses are increased quickly, the temperature difference rises.

Both the thermal stress alone and the combined stress are basically constantly increasing, according to Figure 3.38. Even so, Figure 3.39 shows that the temperature difference at time step 450 s is actually as low as it was at 100 s. This can be explained by slow distribution of the heat in solid bodies due to transient heat conduction. The heat energy is constantly flowing to the structure due to electrical losses. After some time, the difference between the minimum and maximum temperature of the structure will decline, due to heat conduction. In addition, the forced air cooling in the rotor airgap becomes more efficient when the surface temperature is increased.

The equivalent stresses $\sigma_{eq}$ and maximum stresses in the drive cycle $\sigma_{max}$ caused by mechanical, thermal, and combined loads calculated for the fatigue study are illustrated in Figure 3.43 for comparison purposes. The mechanical stresses were calculated using the centrifugal force and electromagnetic torque as loads in the FE model, whereas the thermal stresses were calculated using only the initial thermal strain condition as the input load. The combined stresses were calculated using all the aforementioned loads in the same model. When the maximum stress peaks are observed according to Figure 3.43, the thermal stresses are higher than the mechanical stresses. The thermal stress levels are lower than the equivalent stress levels of the mechanical stresses because the fluctuation of mechanical stresses is much more aggressive, due to the rapidly and constantly changing rotational speed. The results show a considerably high equivalent stress level, when the rapidly changing mechanical stresses and relatively high though slowly changing thermal stresses are combined. Based on these results, it is important to take both the mechanical and thermal loads into account. In addition, the lifetime calculation becomes important, when the loads are highly cyclic and loading conditions are constantly changing.

# Conclusions

Comprehensive theory of both 3D solid element based structural and heat transfer finite element modeling is given, with a number of solution routines for various analyses of rotating structures. This work contains an extensive set of results of rotating structures made using both the beam and 3D solid element-based finite element methods. The beam element approach is utilized to study the rotor and bearing stress history during the rotor dropdown event. The 3D solid element approach is used for studying rotors having multiple parts, thus having contacts, and the contact-based nonlinear behavior under centrifugal load. In addition, thermal mechanical stress history of a rotor in the traction motor and the fatigue life results are presented and discussed in detail. Custom programmed 3D solid finite elements and solution routines, including a proposed contact detection and constraint equation methods in the 3D domain, are utilized in order to generate the presented results. In addition, commercial finite element software Ansys is used for coupled thermal mechanical stress study. Experimental results are used as basis for all the numerical studies of rotating structures presented.

## 4.1 Summary of solution methods

Multiple solution methods developed for studying various rotating machinery aspect are presented and utilized. A discussion of benefits and limitations of different constraint equation methods is presented. The custom, application specific, developed trial force constraint method is presented and tested extensively. In addition, the constraint error aspects are studied and discussed using this custom develop trial force method against the augmented Lagrangian method commonly used in commercial FE software. For proof, an exact method, multipoint constraint method, is applied and benefits and limitations of using this particular method are discussed.

Aspects of obtaining the solution are also discussed. Constraint equation methods that do not require the cross coupling description in the stiffness matrix can be distributed and solved separately. This becomes handy if the problem size

exceeds the computational memory limitations. When utilizing the 3D solid finite element approach, the use of DOF reduction methods may become necessary. Thus, the 3D solid element based models can be reduced by applying, for example, the modal reduction method, which is commonly used also with beam elements. This method is relatively easy to use and very practical for transient and modal problems. Although, this method can typically yield error, if it is applied for solving contact problems, or in general static structural problems. For static problems, a static condensation, also known as Guyan reduction, can be applied.

## 4.2   Rotor dropdown studies

The sudden contact of active magnetic bearings supported rotor during dropdown event was studied. The study introduces the rotor stress behavior during dropdown and the effect of backup bearing misalignment to the rotor dropdown behavior. The backup bearing alignment is a relevant issue for designing the rotor-bearing system. The rotor transient response was studied using the finite element method and the problem was simplified by using modal reduction method for computational reasons. The first moments after the beginning of the dropdown event is typically the most chaotic, thus it was considered that simulation time of 0.5 seconds is long enough to reveal the dynamic performance of the rotor. The measurement results of the experimental modal analysis performed to physical rotor were used for fine-tuning the rotor FE model. Three different horizontal alignment cases were studied. The results observed were the orbits of during rotor-bearing contact and the bending and shear stresses of the rotor during the dropdown event.

Based on the rotor orbit and stress results the backup bearing misalignment has a great effect on the dynamic behavior of the rotor. When no misalignment was introduced, the rotor orbits are smooth and the rotor settles in a short period on the bottom of the bearing inner ring. Rotor oscillation increases as introduced bearing misalignment increases. Even when the maximum bearing misalignment was introduced the rotor did not get into the whirling motion.

The introduced bearing misalignment has an impact the rotor bending stress results. When additional misalignment is introduced, the rotor stresses are increasing in the gravitational direction. The misalignment of backup bearings in horizontal direction yields also proportionally increased bending stress in corresponding direction. In general, the increase of shear stress in direction normal to gravitational force is nominal, although the impact is more observable in horizontal direction (in perpendicular direction to gravitational force).

This study shows that the backup bearing misalignment has a great effect on the dynamic behavior and the rotor motions after a dropdown. The rotor orbits indicate that critical whirling of the rotor could occur if the contacting surfaces are contaminated or otherwise are having some roughness that can induce a greater contact friction, or the damping properties designed properly. The direction of misalignment with respect to the direction of misalignment could be studied in the future. In addition, the behavior of physical rotor during dropdown event should be measured using the position sensors.

## 4.3   Bearing stress studies

The stresses in a backup bearing during dropdown of an AMB-supported rotor were modeled using a numerical simulation. In this study, the system investigated compromised of a flexible rotor, two AMBs and backup bearings. The deep groove ball bearing were modeled as backup bearings using a simplified ball bearing model. The flexible rotor was modeled using Timoshenko finite beam elements. The Hertzian contact stresses in the backup bearing were evaluated in this study. The contact stresses in the backup bearing are influenced by the material properties used in backup bearing as well as the dynamic behavior of rotor. The stress history of the backup bearing based on the transient force equilibrium was calculated. The results showed that the normal contact forces inside the bearing are not evenly distributed among all the balls of the backup bearing. During the first contact, the balls that are initially located in the loaded zone of the backup bearing experience higher stress. The stress experienced by individual ball in the loaded zone is dependent on the ball position, which will change during the rotor dropdown by means of the friction forces induced by rotor-bearing contact.

## 4.4   Summary of internal contact studies

A custom internal contact model is developed and utilized for studying contact behavior at high-speed operation. The results are presented and compared to the results generated by using commercial software (Ansys). In addition, the inclusion of the stress-stiffening effect is also studied extensively. Two example cases are studied; an experimentally verified test shaft assembly with shrink fit interference joint and a conical impeller assembly. With the test shaft assembly, a number of different radial interferences were studied and compared to the measured data. Based on the results, it was noticed that the amount of radial interference in the shrink-fitted joint will not in fact change the free-free natural bending frequencies of the assembly noticeably when the initial stress state is relatively low.

The partial contact opening with the conical impeller assembly was studied and detected using a custom frictionless contact model. The same conditions were studied also using Ansys software for comparison purposes. The custom developed contact model will update the contact status on every speed step. The results generated using this custom contact detection model differ moderately from the ones solved using Ansys. It seems the contact status is not updated in Ansys by default during the regular solution of damped eigenvalue problem, when the rotational speed is used as a variable for a step solution for generating Campbell diagram. Based on the presented results, the stress-stiffening effect should be included into eigenvalue calculation particularly in cases, where relatively heavy bodies attached on the shaft using interference fittings are rotating at high-speeds.

In addition, the contact region constraint error was studied in detail. Two comparison cases with both custom code and Ansys were studied. The MPC method with frictionless contact was determined to be more accurate than the

developed trial force method that is based on used stiffness coefficients having similarities to penalty function method. On Ansys side, normal Lagrangian method was determined to be more accurate than the augmented Lagrangian method in this particular test case. Ansys seems to use a significantly higher number of iterations when solving contact problems, compared to the custom code method.

## 4.5   Thermal stress studies

A solution method for calculating the combined thermal mechanical stress using loading history and fatigue life analysis of a traction motor is presented. A finite element method was utilized to solve coupled field thermal and mechanical problem using commercial FE software. Based on the results, a significant change between mechanical and combined thermomechanical stress levels was observed. In addition, the predicted fatigue life is highly dependent on whether the thermal loads are taken into account or not. The total stress levels of the studied traction motor were acceptable due to the conservative approach adopted in the design process, even when the thermal effects were included. By sacrificing the electromagnetic performance, the mechanical durability of the rotor can be increased. Based on the results presented, a comprehensive thermomechanical stress analysis is essential for optimal design. The results were obtained by utilizing the thermomechanical coupled field solution routine presented in this work. This solution routine could be extended for a electro–thermomechanical coupled problem of interior PMSMs.

## 4.6   Future work

Writing this dissertation has raised multiple interesting future research topics. Starting from beam element modeling, the modeling of the AMB levitation and the rotor translational inertial state due to this levitation while the rotor dropdown is initiated should be studied, and the effect of this initial condition – the AMB levitation – should be investigated.

The inclusion of the flexible frame structure of the electric motor and the stiffness and damping of the foundation to eigenvalue analysis could yield more realistic results. In the rotor-frame system, the mass of the frame contributes to the rotor eigenfrequencies and vice versa. Transient simulation should be implemented for including possible contact-induced nonlinearities, such as directional dependent stiffness and damping in bolt-jointed frame leg-foundation connections, for example.

The proposed direct node-to-node contact modeling method developed for eigenvalue problems of 3D solid element modeled rotors would need to be updated to include the frictional contact forces and contact slippage detection for transient simulation needs. In addition, the thermal expansion-induced geometric changes would require an extension from node-to-node contact detection to node-to-node group detection, in order to properly include geometric changes and contact

slippage. The thermal expansion forces could be included in an analysis of high-speed gas turbine components using proposed node-to-node group contact detection. In addition, the fatigue life of the components of high-speed gas turbine could be studied. Inclusion of thermal effects with the proposed solution routine for the Campbell diagram for a rotor having multiple parts would require a model update during the process. As temperature changes, thermally non-linear material properties such as the thermal expansion coefficient, elastic modulus, thermal conductivity and specific heat coefficient should be updated. Because of this, a model update routine should be developed.

Investigation of various DOF reduction methods could be useful for 3D solid element based rotor dynamics simulations. For transient or eigenvalue problems, the use of dynamically condensed superelements could be useful, since this method can be applied for rotors having contacts, the contact treatment can be done efficiently, and there is no need for coordinate mapping – unlike using modal reduction, since the master DOFs selected are described using physical coordinates. In addition, superelements can be utilized for transient beam element based rotor-bearing contact problems.

[1] Abawi, A. T. The Bending of Bonded Layers Due to Thermal Stress. *Hughes Research Laboratories* (2004), 1–11.

[2] Adeeb, S. *Introduction to Solid Mechanics and Finite Element Analysis using Mathematica.* Kendall Hunt, 2011.

[3] Adhikari, S. Damping Modelling using Generalized Proportional Damping. *Journal of Sound and Vibration 293* (2006), 156–170.

[4] ANSYS, Inc. *ANSYS Mechanical APDL Theory Reference.* ANSYS, Inc., 2013.

[5] Boldea, I., Tutelea, L. N., Parsa, L., and Dorrell, D. Automotive Electric Propulsion Systems with Reduced or no Permanent Magnets: An overview. *IEEE Transactions on Industrial Electronics 61*, 10 (2014), 5696–5711.

[6] Bracikowski, N., Hecquet, M., Brochet, P., and Shirinskii, S. V. Multiphysics Modeling of a Permanent Magnet Synchronous Machine by using Lumped Models. *IEEE Transactions on Industrial Electronics 59*, 6 (2012), 2426–2437.

[7] Çallioğlu, H., Sayer, M., and Demir, E. Stress Analysis of Functionally Graded Discs under Mechanical and Thermal Loads. *Indian Journal of Engineering and Materials Sciences 18*, 2 (2011), 111–118.

[8] Campbell, F. C. *Elements of Metallurgy and Engineering Alloys.* ASM International, 2008.

[9] Cao, J., Allaire, P., Dimond, T., van Rensburg, J. J. J., and Klatt, C. Rotor Drop Analyses and Auxiliary Bearing System Optimization for AMB Supported Rotor/Experimental Validation – Part I: Analysis Method. *The 15th International Symposium on Magnetic Bearings* (2016).

[10] Cao, J., Allaire, P., Dimond, T., van Rensburg, J. J. J., and Klatt, C. Rotor Drop Analyses and Auxiliary Bearing System Optimization for AMB Supported Rotor/Experimental Validation – Part II: Experiment and Optimization. *The 15th International Symposium on Magnetic Bearings* (2016).

[11] CELEBI, K., YARIMPABUC, D., AND KELES, I. A Novel Approach to Thermal and Mechanical Stresses in a FGM Cylinder with Exponentially-Varying Properties. *Journal of Theoretical and Applied Mechanics 55*, 1 (2017), 343–351.

[12] CHAI, F., LI, Y., LIANG, P., AND PEI, Y. Calculation of the maximum mechanical stress on the rotor of interior permanent-magnet synchronous motors. *IEEE Transactions on Industrial Electronics 63*, 6 (2016), 3420–3432.

[13] CHEN, S.-Y. An Equivalent Direct Modeling of a Rotary Shaft with Hot-Fit Components using Contact Element Modal Analysis Results. *Computers and Mathematics with Applications 64*, 5 (2012), 1093–1099.

[14] CHEN, S.-Y., KUNG, C., AND HSU, J.-C. Dynamic Analysis of a Rotary Hollow Shaft with Hot-Fit Part using Contact Elements with Friction. *Transactions of the Canadian Society for Mechanical Engineering 35*, 3 (2011), 461–474.

[15] CHEN, S.-Y., KUNG, C., LIAO, T.-T., AND CHEN, Y.-H. Dynamic Effects of the Interference Fit of Motor Rotor on the Stiffness of a High Speed Rotating Shaft. *Transactions of the Canadian Society for Mechanical Engineering 34*, 2 (2010), 243–261.

[16] CHEN, W. J., AND GUNTER, E. J. *Introduction to Dynamics of Rotor-Bearing Systems.* Trafford Publishing, 2005.

[17] CHEN, W. T., AND NELSON, C. W. Thermal Stress in Bonded Joints. *IBM Journal of Research and Development 23*, 2 (1979), 179–188.

[18] CLIMENTE-ALARCON, V., ANTONINO-DAVIU, J. A., STRANGAS, E. G., AND RIERA-GUASP, M. Rotor–Bar Breakage Mechanism and Prognosis in an Induction Motor. *IEEE Transactions on Industrial Electronics 62*, 3 (2015), 1814–1825.

[19] COLE, M. O. T., KEOGH, P. S., AND BURROWS, C. R. The Dynamic Behavior of a Rolling Element Auxiliary Bearing Following Rotor Impact. *Journal of Tribology 124*, 2 (2002), 406–413.

[20] COOK, R. D. *Concept and Application of Finite Element Analysis.* John Wiley & Sons, 1988.

[21] DAJAKU, G., HOFMANN, H., HETEMI, F., DAJAKU, X., XIE, W., AND GERLING, D. Comparison of Two Different IPM Traction Machines with Concentrated Winding. *IEEE Transactions on Industrial Electronics 63*, 7 (2016), 4137–4149.

[22] DE SANTIAGO, J., BERNHOFF, H., EKERGÅRD, B., ERIKSSON, S., FERHATOVIC, S., WATERS, R., AND LEIJON, M. Electrical Motor Drivelines in Commercial All-Electric Vehicles: A review. *IEEE Transactions on Vehicular Technology 61*, 2 (2012), 475–484.

[23] DONADON, M. V., BRINGHENTI, C., AND MENEZES, J. C. The Stress Stiffening Effects on the Natural Frequecies of Gas Turbine Blades. *VI National Congress of Mechanical Engineering* (2010).

[24] DUDA, P. Finite Element Method Formulation in Polar Coordinates for Transient Heat Conduction Problems. *Journal of Thermal Science 25*, 2 (2016), 188–194.

[25] EL-REFAIE, A. M. Motors/Generators for Traction/Propulsion Applications: A review. *IEEE Vehicular Technology Magazine 8*, 1 (2013), 90–99.

[26] FATEMI, A., DEMERDASH, N. A. O., NEHL, T. W., AND IONEL, D. M. Large-Scale Design Optimization of PM Machines over a Target Operating Cycle. *IEEE Transactions on Industry Applications 52*, 5 (2016), 3772–3782.

[27] FATEMI, A., AND YANG, L. Cumulative Fatigue Damage and Life Prediction Theories: A Survey of the State of the Art for Homogeneous Materials. *International Journal of Fatigue 20*, 1 (1998), 9–34.

[28] FELIPPA, C. A. *Introduction to Aerospace Structures (ASEN 3112)*. University of Colorado at Boulder, 2016.

[29] FELIPPA, C. A. *Introduction to Finite Element Methods (ASEN 5007)*. University of Colorado at Boulder, 2017.

[30] GABRIELSON, T. B. Mechanical-Thermal Noise in Micromachined Acoustic and Vibration Sensors. *IEEE Transactions on Electron Devices 40*, 5 (1993), 903–909.

[31] GAO, Y., LONG, R., PANG, Y., AND LINDENMO, M. Fatigue Properties of an Electrical Steel and Design of EV/HEV IPM Motor Rotors for Durability and Efficiency. *SAE 2010 World Congress & Exhibition* (2010).

[32] GENTA, G., FENG, C., AND TONOLI, A. Dynamics Behavior of Rotating Bladed Discs: A Finite Element Formulation for the Study of Second and Higher Order Harmonics. *Journal of Sound and Vibration 329*, 25 (2010), 5289–5306.

[33] GENTA, G., AND SILVAGNI, M. Three-dimensional FEM rotordynamics and the so-called centrifugal softening of rotors. *Memorie Della Accademia Delle Scienze Di Torino 36* (2012), 3–25.

[34] GENTA, G., AND SILVAGNI, M. On Centrifugal Softening in Finite Element Method Rotordynamics. *Journal of Applied Mechanics 81*, 1 (2013), 011001.

[35] GERADIN, M., AND KILL, N. A New Approach to Finite Element Modelling of Flexible Rotors. *Engineering Computations 1* (1984), 52–64.

[36] Halminen, O., Kärkkäinen, A., Sopanen, J., and Mikkola, A. Active Magnetic Bearing-Supported Rotor with Misaligned Cageless Backup Bearings: A Dropdown Event Simulation Model. *Mechanical Systems and Signal Processing 50–51* (2015), 692–705.

[37] Hobbacher, A. *Recommendations for Fatigue Design of Welded Joints and Components*. Springer, 2009.

[38] Inman, D. J. *Engineering Vibration*. Pearson, 2014.

[39] International Organization for Standardization. ISO1940-1 – Mechanical Vibration – Balance Quality Requirements for Rotors in a Constant (Rigid) State – Part 1: Specification and Verification of Balance Tolerances.

[40] Ishii, T., and Kirk, R. G. Transient Response Technique Applied to Active Magnetic Bearing Machinery During Rotor Drop. *Journal of Vibration and Acoustics-Transactions of the Asme 118*, 4 (1999), 154–163.

[41] Jafri, S. M. M. *Shrink Fit Effects on Rotordynamic Stability: Experimental and Theoretical Study*. Ph.D. thesis. Texas A&M University, 2007.

[42] Jalali, M. H., Ghayour, M., Ziaei-Rad, S., and Shahriari, B. Dynamic Analysis of a High Speed Rotor-Bearing System. *Measurement 53* (2014), 1–9.

[43] Jammi, S. R. Rotor Dynamics in Design of a High Speed Cryogenic Pump for Geo Stationary Launch Vehicles. *ASME 2014 International Design Engineering Technical Conferences and Computers and Information in Engineering Conference 8* (2014), V008T11A065.

[44] Jia, Z., Peng, X., Guan, Z., Wang, L., and Yue, B. Evaluation of the Degradation of Generator Stator Ground Wall Insulation under Multistresses Aging. *IEEE Transactions on Energy Conversion 23*, 2 (2008), 474–483.

[45] Jiang, T., Ryu, S.-K., Zhao, Q., Im, J., Huang, R., and Ho, P. S. Measurement and Analysis of Thermal Stresses in 3D Integrated Structures Containing Through-Silicon-Vias. *Microelectronics Reliability 53*, 1 (2013), 53–62.

[46] Kattan, P. I. *MATLAB Guide to Finite Elements*. Springer, 2008.

[47] Kim, J., Yoon, J.-C., and Kang, B.-S. Finite Element Analysis and Modeling of Structure with Bolted Joints. *Applied Mathematical Modelling 31*, 5 (2007), 895–911.

[48] Kirchgässner, B. Finite Elements in Rotordynamics. *Procedia Engineering 144* (2016), 736–750.

[49] Knetsch, D., Funk, M., Kennerknecht, T., and Eberl, C. Load Data Calculation in Electric Axle Drives and Fatigue Assessment for the Electric Motor Subsystem. *Materials Testing 56*, 7–8 (2014), 535–541.

[50] Kärkkäinen, A. *Dynamic Simulations of Rotors During Drop on Retainer Bearings.* Ph.D. thesis. Lappeenranta University of Technology, 2007.

[51] Kärkkäinen, A., Sopanen, J., and Mikkola, A. Dynamic Simulation of a Flexible Rotor During Drop on Retainer Bearings. *Journal of Sound and Vibration 306*, 3–6 (2007), 601–617.

[52] Kulkarni, A., Ranjha, S. A., and Kapoor, A. Fatigue Analysis of a Suspension for an In-Wheel Electric Vehicle. *Engineering Failure Analysis 68* (2016), 150–158.

[53] Kumar, S., Rao, R., and Rajeevalochanam, B. A. Current Practices in Structural Analysis and Testing of Aero-Engine Main Shafts. *Procedia Engineering 55* (2007), 499–509.

[54] Kupnik, M., Wygant, I. O., and Khuri-Yakub, B. T. Finite Element Analysis of Stress Stiffening Effects in CMUTs. *2008 IEEE International Ultrasonics Symposium Proceedings* (2008).

[55] Lee, J. G., and Palazzolo, A. Catcher Bearing Life Prediction using a Rainflow Counting Approach. *Journal of Tribology 134*, 3 (2012), 031101.

[56] Lee, Y. L. *Fatigue Testing and Analysis: Theory and Practice.* Butterworth–Heinemann, 2005.

[57] Lin, Z.-C., and Lee, B.-Y. An investigation of the residual stress of a machined workpiece considering tool flank wear. *Journal of Materials Processing Technology 51*, 1–4 (1995), 1–24.

[58] Lindh, P., Gerami Tehrani, M., Lindh, T., Montonen, J. H., Pyrhönen, J., Sopanen, J. T., Niemelä, M., Alexandrova, Y., Immonen, P., Aarniovuori, L., and Polikarpova, M. Multidisciplinary design of a permanent-magnet traction motor for a hybrid bus taking the load cycle into account. *IEEE Transactions on Industrial Electronics 63*, 6 (2016), 3397–3408.

[59] Lindh, P. M., Immonen, P., Alexandrova, Y., Gerami Tehrani, M., Pyrhönen, J. J., and Sopanen, J. T. The Design of Rotor Geometry in a Permanent Magnet Traction Motor for a Hybrid Bus. *2014 International Conference on Electrical Machines (ICEM)* (2014), 310–315.

[60] Liu, G. R., and Quek, S. S. *The Finite Element Method.* Butterworth–Heinemann, 2013.

[61] Logan, D. L. *A First Course in the Finite Element Method.* Cengage Learning, 2007.

[62] LOGIE, W. R., PYE, J. D., AND COVENTRY, J. Thermal Elastic Stress in Sodium Receiver Tubes. *Asia Pacific Solar Research Conference* (2016), 1–12.

[63] LONG, S. G., AND ZHOU, Y. C. Thermal Fatigue of Particle Reinforced Metal-Matrix Composite Induced by Laser Heating and Mechanical Load. *Composites Science and Technology 65*, 9 (2005), 1391–1400.

[64] LU, K. H., RYU, S.-K., ZHAO, Q., HUMMLER, K., IM, J., HUANG, R., AND HO, P. S. Temperature-dependent Thermal Stress Determination for Through-Silicon-Vias (TSVs) by Combining Bending Beam Technique with Finite Element Analysis. *2011 Electronic Components and Technology Conference* (2011), 1475–1480.

[65] LU, K. H., ZHANG, X., RYU, S., HUANG, R., AND HO, P. S. Thermal Stresses Analysis of 3-D Interconnect. *AIP Conference Proceedings 1143*, 224 (2009), 224–230.

[66] MA, L. S., AND WANG, T. J. Nonlinear Bending and Post-Buckling of a Functionally Graded Circular Plate under Mechanical and Thermal Loadings. *International Journal of Solids and Structures 40*, 13–14 (2003), 3311–3330.

[67] MCFARLAND, J. D., AND JAHNS, T. M. Investigation of the Rotor Demagnetization Characteristics of Interior PM Synchronous Machines During Fault Conditions. *IEEE Transactions on Industry Applications 50*, 4 (2014), 2768–2775.

[68] MIAO, H., ZANG, C., AND FRISWELL, M. Model Updating and Validation of a Dual-Rotor System. *ISMA2014 International Conference on Noise and Vibration Engineering* (2014), 2723–2737.

[69] NANDI, A., AND NEOGY, S. Modelling of Rotors with Three-Dimensional Solid Finite Elements. *Journal of Strain Analysis for Engineering Design 36*, 4 (2001), 359–371.

[70] NEISI, N., HEIKKINEN, J. E., SIKANEN, E., AND SOPANEN, J. Stress Analysis of a Touchdown Bearing Having an Artificial Crack. *ASME 2017 International Design Engineering Technical Conferences and Computers and Information in Engineering Conference 8* (2017), V008T12A034.

[71] NEISI, N., SIKANEN, E., HEIKKINEN, J. E., AND SOPANEN, J. Effect of Off-Sized Balls on Contact Stresses in a Touchdown Bearing. *Tribology International 120* (2018), 340–349.

[72] NEJATI, M., PALUSZNY, A., AND ZIMMERMAN, R. W. A Finite Element Framework for Modeling Internal Frictional Contact in Three-Dimensional Fractured Media using Unstructured Tetrahedral Meshes. *Computer Methods in Applied Mechanics and Engineering 306* (2010), 123–150.

[73] NELSON, H. D. A Finite Rotating Shaft Element using Timoshenko Beam Theory. *Journal of Mechanical Design 102*, 4 (1980), 793–803.

[74] NELSON, H. D., AND MCVAUGH, J. M. The Dynamics of Rotor-Bearing Systems using Finite Elements. *Journal of Engineering for Industry 98*, 2 (1976), 593–600.

[75] NERG, J., RILLA, M., RUUSKANEN, V., PYRHÖNEN, J., AND RUOTSALAINEN, S. Direct-Driven Interior Magnet Permanent-Magnet Synchronous Motors for a Full Electric Sports Car. *IEEE Transactions on Industrial Electronics 61*, 8 (2014), 4286–4294.

[76] NIKISHKOV, G. P. *Programming Finite Elements in Java.* Springer, 2010.

[77] PARAMONOV, V. V., AND GONIN, I. V. 3D Thermal Stress Analysis for the CDS Structures. *Proceedings of EPAC 2000* (2000), 1990–1992.

[78] PRAKASH, S., AND PURI, V. K. Foundations for Vibrating Machines. *Journal of Structural Engineering (Madras)* (2006), 1–39.

[79] QIN, Z.-Y., HAN, Q.-K., AND CHU, F.-L. Analytical Model of Bolted Disk–Drum Joints and its Application to Dynamic Analysis of Jointed Rotor. *Proceedings of the Institution of Mechanical Engineers, Part C: Journal of Mechanical Engineering Science 228*, 4 (2014), 646–663.

[80] RAO, J. S. Finite Element Methods for Rotor Dynamics. *History of Rotating Machinery Dynamics* (2011), 269–297.

[81] RAO, J. S. Transient Forward and Backward Whirl of Beam and Solid Rotors With Stiffening and Softening Effects. *ASME 2011 International Design Engineering Technical Conferences and Computers and Information in Engineering Conference 1* (2011), 911–920.

[82] RAO, J. S., AND SREENIVAS, R. Dynamics of Asymmetric Rotors using Solid Models. *Proceedings of the International Gas Turbine Congress 2003* (2003), 1–6.

[83] RASHID, A., AND STRÖMBERG, N. An Efficient Sequential Approach for Simulation of Thermal Stresses in Disc Brakes. *15th Nordic Symposium on Tribology, NORDTRIB 1* (2012).

[84] RICHARDSON, I.-J., AND HYDE, T.-M .AND TAYLOR, J.-W. A Three-Dimensional Finite Element Investigation of the Bolt Stresses in an Aero-Engine Curvic Coupling under a Blade Release Condition. *Proceedings of the Institution of Mechanical Engineers, Part G: Journal of Aerospace Engineering 214*, 4 (2000), 231–245.

[85] SAARI, J. *Thermal Analysis of High-Speed Induction Machines.* Ph.D. thesis. Helsinki University of Technology, 1998.

[86] Santos, H. L. V., Luersen, M. A., and Bavastri, C. A. Experimental Evaluation of Numerical Models to Represent the Stiffness of Laminated Rotor Cores in Electrical Machines. *Engineering Science and Technology, an International Journal 8*, 4 (2013), 457–471.

[87] Sasek, J. Eigenfrequency Sensitivity Analysis of Flexible Rotors. *Applied and Computational Mechanics 1*, 1 (2012), 289–298.

[88] Schmied, J., and Pradetto, J. C. Behavior of a One Ton Rotor Being Dropped into Auxiliary Bearings. *Proceedings of the 3rd International Symposium on Magnetic Bearings* (1992), 145–156.

[89] Shimazaki, H., and Shinomoto, S. A Method for Selecting the Bin Size of a Time Histogram. *Neural Computation 19*, 6 (2007), 1503–1527.

[90] Sikanen, E., Halminen, O., Heikkinen, J. E., Sopanen, J., Mikkola, A., and Matikainen, M. Stresses of an AMB-Supported Rotor Arising from the Sudden Contact with Backup Bearings. *Proceedings of the ASME 2015 International Mechanical Engineering Congress and Exposition IMECE2015* (2015), V04AT04A039.

[91] Sikanen, E., Heikkinen, J. E., and Sopanen, J. Shrink-Fitted Joint Behavior using Three-Dimensional Solid Finite Elements in Rotor Dynamics with Inclusion of Stress-Stiffening Effect. *Advances in Mechanical Engineering 10*, 6 (2018), 1–13.

[92] Sikanen, E., Nerg, J., Heikkinen, J. E., Gerami Tehrani, M., and Sopanen, J. Fatigue Life Calculation Procedure for the Rotor of an Embedded Magnet Traction Motor Taking into Account Thermomechanical Loads. *Mechanical Systems and Signal Processing 111* (2018), 36–46.

[93] Stimac, G., Braut, S., Bulic, N., and Zigulic, R. Modeling and Experimental Verification of a Flexible Rotor/AMB System. *COMPEL – The International Journal for Computation and Mathematics in Electrical and Electronic Engineering 32*, 4 (2013), 1244–1254.

[94] Sun, G. Auxiliary Bearing Life Prediction using Hertzian Contact Bearing Model. *Journal of Vibration and Acoustics 128*, 2 (2006), 203–209.

[95] Tannous, M., Cartraud, P., Dureisseix, D., and Torkhani, M. A Beam to 3D Model Switch for Rotor Dynamics Applications. *Engineering Structures 84* (2015), 54–66.

[96] Wagner, M. B., Younan, A., Allaire, P., and Cogill, R. Model Reduction Methods for Rotor Dynamic Analysis: A Survey and Review. *International Journal of Rotating Machinery 2010* (2010), 1–17.

[97] Zeng, S. Motion of AMB Rotor in Backup Bearings. *Journal of Vibration and Acoustics 124*, 3 (2002), 460–464.

[98] ZHANG, J., AND WANG, Q. A Finite Element Method for Solving 2D Contact Problems with Coulomb Friction and Bilateral Constraints. *Journal of Computational Physics (2014)* (2014).

[99] ZHAO, S., HILMAS, G. E., AND DHARANI, L. R. Behavior of a Composite Multidisk Clutch Subjected to Mechanical and Frictionally Excited Thermal Load. *Wear 264*, 11–12 (2008), 1059–1068.

[100] ZHOU, C. L., FRISWELL, M. I., AND LI, J. Y. Condition Monitoring of Cracked Shaft using Active Magnetic Bearings. *Challenges of Power Engineering and Environment 1* (2007), 494–504.

[101] ZHOU, S.-T., AND LI, H.-G. Three Dimensional Finite Element Simulation of Solid Rotor System Based on INTESIM and ARPACK Tools. *Journal of System Simulation 26*, 6 (2014), 1391–1399.

[102] ZIENKIEWICZ, O. C., AND TAYLOR, R. E. *The Finite Element Method.* McGraw-Hill, 1993.

[103] ZIENKIEWICZ, O. C., AND TAYLOR, R. L. *The Finite Element Method: Volume 1 The Basis.* Butterworth–Heinemann, 2010.

[104] ZIENKIEWICZ, O. C., AND TAYLOR, R. L. *The Finite Element Method: Volume 2 Solid Mechanics.* Butterworth–Heinemann, 2010.

[105] ÖZTÜRK, T., AND ÖZTÜRK, Z. Vibration Absorption and Isolation in Dynamically Loaded Foundations. *The 14th World Conference on Earthquake Engineering* (2008).

# Constructing element shape functions

In this appendix, a general description of forming isoparametric element shape functions, is given. The selection of monomials used for a particular element will determine the basic behavior of the element. A good selection of monomials will guarantee correct and chronologically increasing eigenmodes for the element. Monomials should be selected in chronological order. The number of monomials selected and the highest order of monomials will increase the number of eigenmodes of the element. Due to the fact the moment matrix $\mathbf{P}$ is a square matrix, the number of monomials is equal to the number of nodes in the element. Therefore, the greater the number of nodes is in the element, the greater the number of possible eigenmodes [60].

Even though the topic is on isoparametric element shape functions, for convenience, the physical coordinates are used to express individual monomials. The vector of monomials in three dimensional domain using physical coordinates can be written as follows:

$$\boldsymbol{p}^{\mathrm{T}}\left(\boldsymbol{x}\right) = \begin{bmatrix} 1 & x & y & z & xy & yz & zx & x^2 & y^2 & z^2 & \cdots & x^p & y^p & z^p \end{bmatrix} \quad \text{(A.1)}$$

Figures A.1 and A.2 visualize how to generate the monomials in two and three dimensional cases. The moment matrix is formed by placing node coordinates into the monomial vector of corresponding node as follows:

$$\mathbf{P} = \begin{bmatrix} \boldsymbol{p}^{\mathrm{T}}\left(\boldsymbol{x}_1\right) \\ \boldsymbol{p}^{\mathrm{T}}\left(\boldsymbol{x}_2\right) \\ \vdots \\ \boldsymbol{p}^{\mathrm{T}}\left(\boldsymbol{x}_n\right) \end{bmatrix} \quad \text{(A.2)}$$

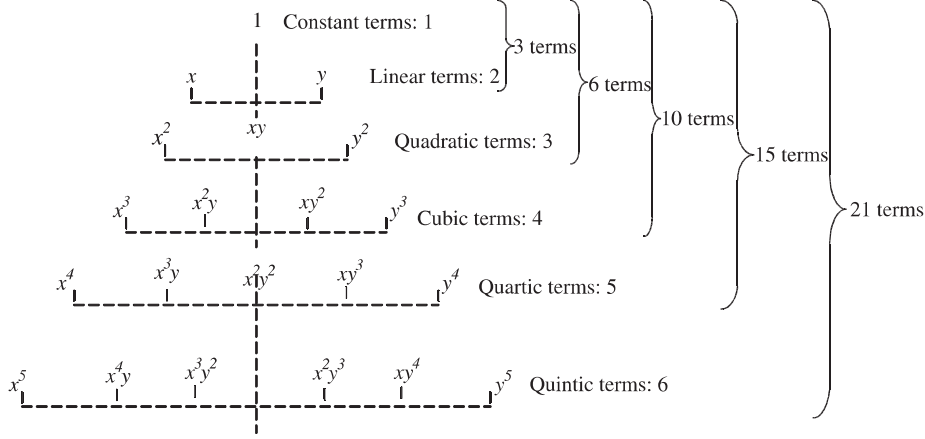By placing the node coordinates into moment matrix we get

**Figure A.1.** Pascal triangle for two-dimensional monomials [60]

$$
\mathbf{P} = \begin{bmatrix}
1 & x_1 & y_1 & z_1 & x_1 y_1 & y_1 z_1 & z_1 x_1 & x_1^2 & y_1^2 & z_1^2 & \cdots \\
1 & x_2 & y_2 & z_2 & x_2 y_2 & y_2 z_2 & z_2 x_2 & x_2^2 & y_2^2 & z_2^2 & \cdots \\
& & & & & \vdots & & & & & \\
1 & x_n & y_n & z_n & x_n y_n & y_n z_n & z_n x_n & x_n^2 & y_n^2 & z_n^2 & \cdots
\end{bmatrix} \tag{A.3}
$$

The vector of shape functions can be written as follows:

$$
\boldsymbol{N}\left(\boldsymbol{x}\right) = \boldsymbol{p}^{\mathrm{T}}\left(\boldsymbol{x}\right) \mathbf{P}^{-1} = \begin{bmatrix} N_1\left(\boldsymbol{x}\right) & N_2\left(\boldsymbol{x}\right) & \cdots & N_n\left(\boldsymbol{x}\right) \end{bmatrix} \tag{A.4}
$$

In Equation (A.4) it is assumed that the inverse of the moment matrix exists. The inverse of the moment matrix is dependent on the monomials used and nodal distribution of the element. The use of moment matrix and Equation (A.4) for constructing shape functions for isoparametric elements is very suitable since the element shape is ideal and natural coordinates have values only in range [-1, 1]. The shape functions will have to fulfill certain requirements: two main requirements are presented herein. If the constant monomial is included, the sum of shape functions must form unity as follows[60]:

$$
\sum_{i=1}^{n} N_i\left(\boldsymbol{x}\right) = 1 \tag{A.5}
$$

The delta function property verifies the functionality of individual shape functions as follows:

$$
\begin{aligned}
N_i\left(\boldsymbol{x}_j\right) &= 1, \quad \text{if} \quad i = j \\
N_i\left(\boldsymbol{x}_j\right) &= 0, \quad \text{if} \quad i \neq j
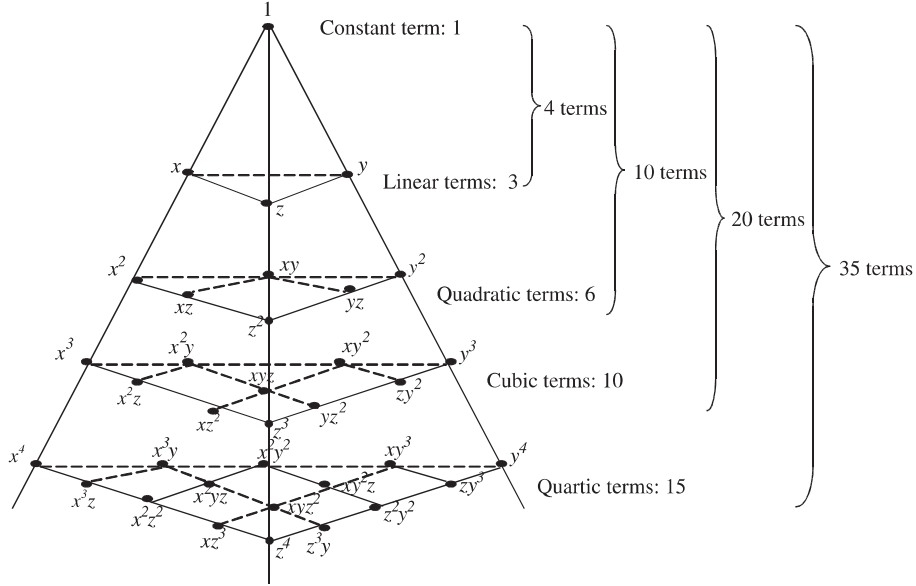\end{aligned} \tag{A.6}
$$

**Figure A.2.** Pascal pyramid for three-dimensional monomials [60]

The delta function property indicates that the shape function $N_i$ should be unity at home nodes $\boldsymbol{x}_i$ and zero at remote node $\boldsymbol{x}_j$. It is possible to construct the shape function using the delta function property. [60]

# Common isoparametric elements

Common isoparametric 2D and 3D elements are introduced in this appendix. The fundamentals of isoparametric elements are presented. The element monomials and corresponding shape functions are introduced with detailed illustrations of element shape and node order. In addition, element dependent integrals are given. Isoparametric elements are well suited for numerical integration. Other possible formulations are the use of physical coordinates for quadrilaterals and hexahedrons or use of area coordinates calculated from physical coordinates, for triangles and tetrahedrons.

**Isoparametric coordinate mapping**

With isoparametric elements, the physical coordinates, and thus the physical shape of the element, is mapped into natural coordinates, where the element shape is always ideal [60]. In figure B.1 are illustrated the shape of the same element in physical and natural coordinate systems.
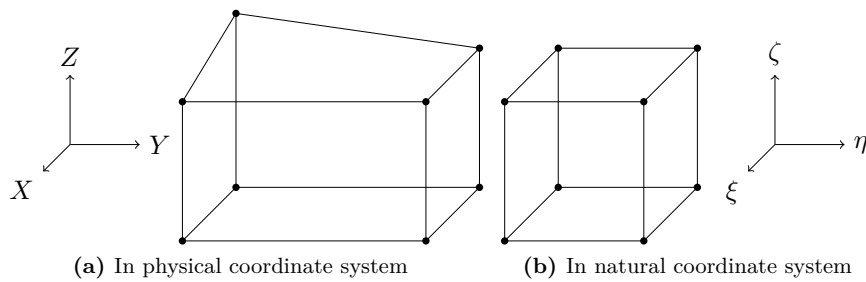


**(a)** In physical coordinate system    **(b)** In natural coordinate system

**Figure B.1.** Same linear hexahedron element described using two different coordinate systems

Displacement expressions can be written as follows:

$$x = \sum_{j=1}^{n} N_i \left(\xi, \eta, \zeta\right) x_j$$

$$y = \sum_{j=1}^{n} N_i \left(\xi, \eta, \zeta\right) y_j \tag{B.1}$$

$$z = \sum_{j=1}^{n} N_i \left(\xi, \eta, \zeta\right) z_j$$

where $x_j$, $y_j$ and $z_j$ are physical coordinates of node $j$, $n$ is the number of shape functions and $\xi$, $\eta$ and $\zeta$ are natural coordinates used for isoparametric expression [60].

Partial derivatives of physical coordinates, that are needed for generating the strain matrix **B**, for isoparametric element shape functions cannot be directly calculated. Therefore, the Jacobian matrix is used to express the physical coordinate derivatives, based on the partial derivatives of natural coordinates, as follows:

$$\mathbf{J} = \begin{bmatrix} \frac{\partial x}{\partial \xi} & \frac{\partial y}{\partial \xi} & \frac{\partial z}{\partial \xi} \\ \frac{\partial x}{\partial \eta} & \frac{\partial y}{\partial \eta} & \frac{\partial z}{\partial \eta} \\ \frac{\partial x}{\partial \zeta} & \frac{\partial y}{\partial \zeta} & \frac{\partial z}{\partial \zeta} \end{bmatrix} \tag{B.2}$$

$$\begin{bmatrix} \frac{\partial N_i}{\partial x} \\ \frac{\partial N_i}{\partial y} \\ \frac{\partial N_i}{\partial z} \end{bmatrix} = \mathbf{J}^{-1} \begin{bmatrix} \frac{\partial N_i}{\partial \xi} \\ \frac{\partial N_i}{\partial \eta} \\ \frac{\partial N_i}{\partial \zeta} \end{bmatrix} \tag{B.3}$$

The element volume can be calculated by integrating the Jacobian as follows [46]:

$$V = \int_{-1}^{1} \int_{-1}^{1} \int_{-1}^{1} J d\xi d\eta d\zeta \tag{B.4}$$

**Quadratic hexahedron**

Monomials used

$$1, \quad \xi, \quad \eta, \quad \zeta, \quad \xi\eta, \quad \eta\zeta, \quad \xi\zeta, \quad \xi^2, \quad \eta^2, \quad \zeta^2, \quad \xi\eta\zeta,$$
$$\xi\eta^2, \quad \xi\zeta^2, \quad \xi^2\eta, \quad \eta\zeta^2, \quad \xi^2\zeta, \quad \eta^2\zeta, \quad \xi^2\eta\zeta, \quad \xi\eta^2\zeta, \quad \xi\eta\zeta^2$$

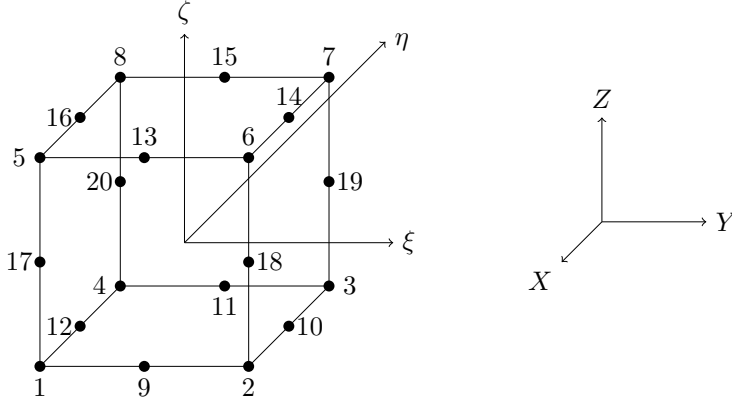Figure B.2 describes the 20-node hexahedron element node order. The shape

**Figure B.2.** 20-node hexahedron element described using natural coordinates

functions of an isoparametric 20-node quadratic hexahedron element are given in Equation (B.5) for corner nodes, and in Equation (B.6) for midside nodes.

$$N_l = \frac{1}{8}(1 + \xi_l\xi)(1 + \eta_l\eta)(1 + \zeta_l\zeta)(\xi_l\xi + \eta_l\eta + \zeta_l\zeta - 2), \quad l = 1, \cdots, 8 \qquad \text{(B.5)}$$

$$N_l = \frac{1}{4}(1 - \xi^2)(1 + \eta_l\eta)(1 + \zeta_l\zeta), \quad l = 9, 11, 13, 15$$

$$N_l = \frac{1}{4}(1 - \eta^2)(1 + \xi_l\xi)(1 + \zeta_l\zeta), \quad l = 10, 12, 14, 16 \qquad \text{(B.6)}$$

$$N_l = \frac{1}{4}(1 - \zeta^2)(1 + \xi_l\xi)(1 + \eta_l\eta), \quad l = 17, \cdots, 20$$

The integration scheme for the isoparametric hexahedron element family (linear, quadratic, cubic, quartic) can be written as follows:

$$I = \int_{-1}^{1} \int_{-1}^{1} \int_{-1}^{1} f(\xi, \eta, \zeta) \det \mathbf{J} d\xi d\eta d\zeta \qquad \text{(B.7)}$$

**Quadratic tetrahedron**

Monomials used

$$1, \quad \xi, \quad \eta, \quad \zeta, \quad \xi\eta, \quad \eta\zeta, \quad \xi\zeta, \quad \xi^2, \quad \eta^2, \quad \zeta^2$$

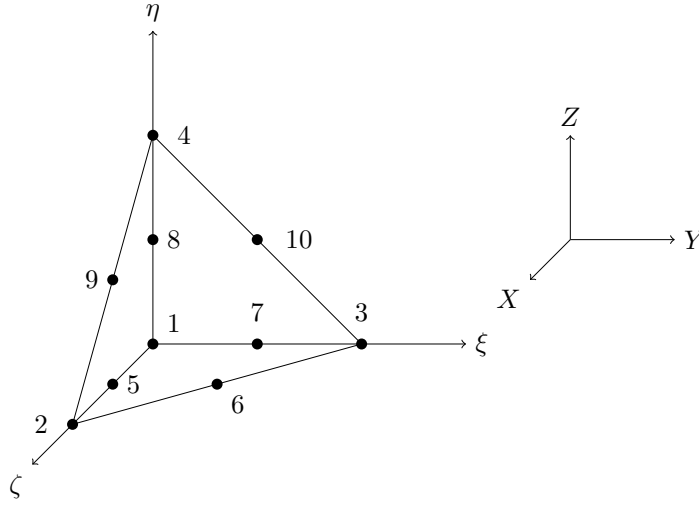10-node tetrahedron element shape functions are

**Figure B.3.** 10-node tetrahedron element described using the natural coordinates

$$
\begin{aligned}
N_1 &= (\xi + \eta + \zeta - 1)(2\xi + 2\eta + 2\zeta - 1) \\
N_2 &= \xi(2\xi - 1) \\
N_3 &= \eta(2\eta - 1) \\
N_4 &= \zeta(2\zeta - 1) \\
N_5 &= 4\xi(1 - \xi - \eta - \zeta) \\
N_6 &= 4\eta\xi \\
N_7 &= 4\eta(1 - \xi - \eta - \zeta) \\
N_8 &= 4\zeta(1 - \xi - \eta - \zeta) \\
N_9 &= 4\xi\zeta \\
N_{10} &= 4\eta\zeta
\end{aligned}
\tag{B.8}
$$

The integration scheme for the isoparametric tetrahedron element family, using natural coordinates, can be written as follows:

$$
I = \int_0^1 \int_0^1 \int_0^1 f(\xi, \eta, \zeta) \frac{1}{6} \det \mathbf{J} d\xi d\eta d\zeta
\tag{B.9}
$$

**Isoparametric 8-node plane quadrilateral element**

Monomials used

$$
1, \quad \xi, \quad \eta, \quad \xi\eta, \quad \xi^2, \quad \eta^2 \quad \xi^2\eta \quad \xi\eta^2
$$

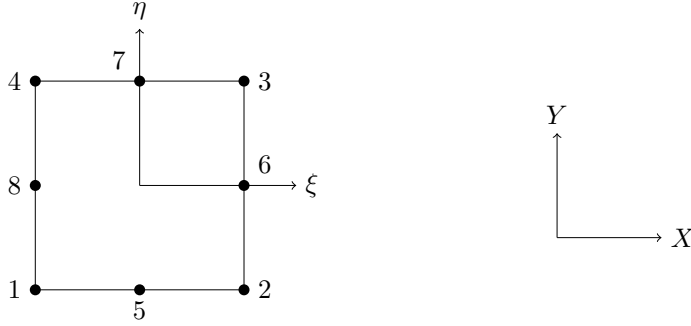Isoparametric 8-node quadrilateral element is introduced in Figure B.4.

**Figure B.4.** Quadratic quadrilateral element presented using natural coordinates

8-node quadrilateral element shape functions are

$$
\begin{aligned}
N_1 &= \frac{1}{4}(1-\xi)(1-\eta)(-\xi-\eta-1) \\
N_2 &= \frac{1}{4}(1+\xi)(1-\eta)(\xi-\eta-1) \\
N_3 &= \frac{1}{4}(1+\xi)(1+\eta)(\xi+\eta-1) \\
N_4 &= \frac{1}{4}(1-\xi)(1+\eta)(-\xi+\eta-1) \\
N_5 &= \frac{1}{2}(1-\xi^2)(1-\eta) \\
N_6 &= \frac{1}{2}(1+\xi)(1-\eta^2) \\
N_7 &= \frac{1}{2}(1-\xi^2)(1+\eta) \\
N_8 &= \frac{1}{2}(1-\xi)(1-\eta^2)
\end{aligned}
\tag{B.10}
$$

The integration scheme for the isoparametric quadrilateral element family can be written as follows:

$$
I = \int_{-1}^{1}\int_{-1}^{1} f(\xi,\eta)\det\mathbf{J}d\xi d\eta
\tag{B.11}
$$

**Isoparametric 6-node plane triangle element**

Monomials used

$$
1,\quad \xi,\quad \eta,\quad \xi\eta,\quad \xi^2,\quad \eta^2
$$

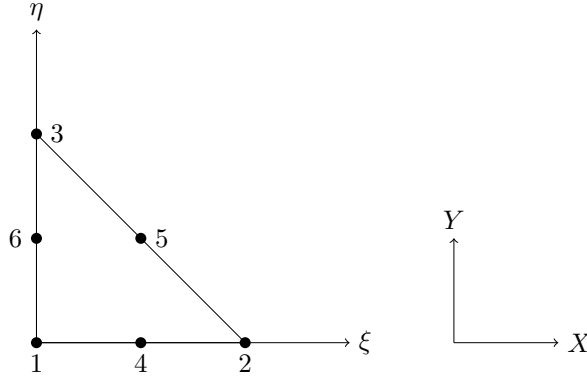The natural coordinates of isoparametric quadratic triangle element are illustrated in Figure B.5.



**Figure B.5.** Isoparametric quadratic triangle

6-node quadratic triangle element shape functions are

$$
\begin{aligned}
N_1 &= (\xi + \eta - 1)(2\xi + 2\eta - 1) \\
N_2 &= \xi(2\xi - 1) \\
N_3 &= \eta(2\eta - 1) \\
N_4 &= 4\xi(1 - \xi - \eta) \\
N_5 &= 4\eta\xi \\
N_6 &= 4\eta(1 - \xi - \eta)
\end{aligned}
\tag{B.12}
$$

The integration scheme for the isoparametric triangular element family, using natural coordinates, can be written as follows

$$
I = \int_0^1 \int_0^1 f(\xi, \eta) \frac{1}{2} \det \mathbf{J} d\xi d\eta
\tag{B.13}
$$

# Numerical integration

In this appendix, numerical integration schemes and integration points are given for four quadratic isoparametric elements; 3D solid hexahedron, 3D solid tetrahedron, 2D triangle and 2D quadrilateral. In the end, a table of numerical integration points of various rotor dynamics related element matrices and force vectors is compiled. Only full integration schemes are presented here. Various reduced integration schemes are given in [4], and a discussion of benefits and applications for reduced integration is provided in Cook [20].

### Gaussian quadrature

Gaussian quadrature is a commonly used numerical integration scheme for definite integrals. In order to use Gauss integration, the interval $[a, b]$ of the integral must be changed $[-1, 1]$ as follows:

$$\int_a^b f(x)\, dx = \frac{b - a}{2} \int_{-1}^1 f\left(\frac{b - a}{2} x + \frac{a + b}{2}\right) dx \tag{C.1}$$

The use of $n$ Gauss integral points provides an exact result for the polynomial integrand of order up to $2n - 1$ [60]. The first three Gauss integral points are presented in Table C.1.

**Table C.1.** The three first Gaussian quadrature integration points and coefficients [60]

| $n$ | $x_i$ | $W_i$ |
|-----|-------|-------|
| 1 | $0$ | $2$ |
| 2 | $\pm\sqrt{\frac{1}{3}}$ | $1$ |
| 3 | $0$ | $\frac{8}{9}$ |
|   | $\pm\sqrt{\frac{3}{5}}$ | $\frac{5}{9}$ |

When applying Gaussian quadrature to isoparametric finite element expression, the integration interval is $[-1, 1]$ by default, and when a sufficient number of Gauss points are used, Equation (C.1) can be written as follows:

$$\int_{-1}^{1} f(x)\, dx = \sum_{i=1}^{n} W_i f(x_i) \tag{C.2}$$

where $n$ is the number of used Gauss integration points, and $W_i$ and $x_i$ are the weight coefficient and the value of the $i$th Gauss integration point.

**Hexahedron elements**

Hexahedron elements can be numerically integrated using the Gaussian quadrature rule, as follows:

$$I = \sum_{k=1}^{n} \sum_{j=1}^{m} \sum_{i=1}^{l} W_k W_j W_i f(\xi_i, \eta_j, \zeta_k) \tag{C.3}$$

Other integration rules also exist such as the 14-point rule introduced in [4].

**Tetrahedron elements**

For 10-node quadratic tetrahedron elements, the 4-point tetrahedron integration rule can be written as follows:

$$I = \sum_{i=1}^{4} W_i f(\xi_i, \eta_i, \zeta_i) \tag{C.4}$$

The 4-point tetrahedron integration rule coefficients are presented in Table C.2. Other tetrahedron rules exists depending on the number of element nodes. According to [4], the quadrature rule is possible for use for triangle and tetrahedron elements when using a special integration point distribution.

**Table C.2.** Isoparametric tetrahedron element 4-point integration points and coefficients [4]

| $i$ | $\xi_i$ | $\eta_i$ | $\zeta_i$ | $W_i$ |
|---|---|---|---|---|
| 1 | 0.138196601125010 | 0.138196601125010 | 0.138196601125010 | 0.25 |
| 2 | 0.585410196624968 | 0.138196601125010 | 0.138196601125010 | 0.25 |
| 3 | 0.138196601125010 | 0.585410196624968 | 0.138196601125010 | 0.25 |
| 4 | 0.138196601125010 | 0.138196601125010 | 0.585410196624968 | 0.25 |

## Quadrilateral elements

Quadrilateral elements can be numerically integrated using the Gaussian quadrature rule, as follows:

$$I = \sum_{j=1}^{m} \sum_{i=1}^{l} W_j W_i f\left(\xi_i, \eta_j\right) \tag{C.5}$$

For visualization, the $3 \times 3$ two-dimensional Gaussian quadrature integration point locations are presented in Figure C.1.
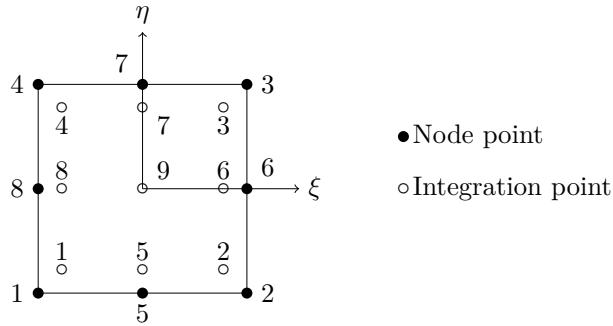


**Figure C.1.** The $3 \times 3$ Gaussian quadrature point locations

## Triangle elements

For the 6-node triangle element, the 3-point triangle integration rule can be written as follows:

$$\int_0^1 \int_0^1 f\left(\xi, \eta\right) = \sum_{i=1}^{3} W_i f\left(\xi_i, \eta_i\right) \tag{C.6}$$

The 3 point triangle integration rule coefficients are given in Table C.3, and the points are visualized in Figure C.2.

**Table C.3.** Isoparametric triangle element 3-point integration points and coefficients [2, 4]

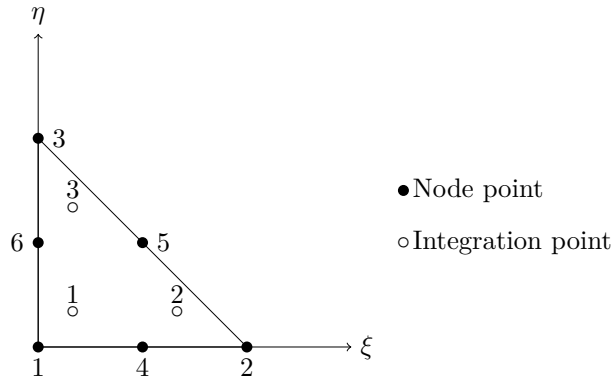| $i$ | 1 | 2 | 3 |
|---|---|---|---|
| $\xi_i$ | 1/6 | 2/3 | 1/6 |
| $\eta_i$ | 1/6 | 1/6 | 2/3 |
| $w_i$ | 1/3 | 1/3 | 1/3 |

**Figure C.2.** Isoparametric quadratic triangle integration points

**Integration points for various element matrices**

In Tables C.4 and C.5, the recommended integration points for 3D solid element matrices and corresponding force vectors are compiled. The matrices are grouped as based on the formulation; matrices using shape function matrix $\mathbf{N}$, such as mass matrix, require a greater number of integration points, whereas matrices using strain matrix $\mathbf{B}$ or its variant – such as the stiffness matrix – may a require lower number of integration points. Correspondingly, the force vectors are grouped as based on their formulation; vectors using shape function matrix $\mathbf{N}$, such as body force vector $\boldsymbol{F}_b^e$, vectors using strain matrix $\mathbf{B}$, or its variant – such as body force vector $\boldsymbol{F}_{\Delta T}^e$ and surface force vectors using shape function matrix $\mathbf{N}$, such as surface force vector $\boldsymbol{F}_s^e$.

**Table C.4.** Recommended integration points for various elements matrices [4]

| Matrix | 20-node hexahedron | 10-node tetrahedron |
|---|:---:|:---:|
| $\mathbf{M}^e$, $\mathbf{G}^e$ | $3 \times 3 \times 3$ | 4 |
| $\mathbf{K}_e^e$, $\mathbf{K}_G^e$ | $2 \times 2 \times 2$ | 4 |

**Table C.5.** Recommended integration points for various elements force vectors [4]

| Vector | 20-node hexahedron | 10-node tetrahedron |
|---|:---:|:---:|
| $\boldsymbol{F}_b^e$, $\boldsymbol{F}_\Omega^e$, $\boldsymbol{F}_g^e$ | $3 \times 3 \times 3$ | 4 |
| $\boldsymbol{F}_{\Delta T}^e$ | $2 \times 2 \times 2$ | 4 |
| $\boldsymbol{F}_s^e$, $\boldsymbol{F}_p^e$ | $3 \times 3$ | 6 |

**ACTA UNIVERSITATIS LAPPEENRANTAENSIS**

782. SIPILÄ, JENNI. The many faces of ambivalence in the decision-making process. 2017. Diss.

783. HAN, MEI. Hydrodynamics and mass transfer in airlift bioreactors; experimental and numerical simulation analysis. 2017. Diss.

784. ESCALANTE, JOHN BRUZZO. Dynamic simulation of cross-country skiing. 2017. Diss.

785. NOKKA, JARKKO. Energy efficiency analyses of hybrid non-road mobile machinery by real-time virtual prototyping. 2018. Diss.

786. VUORIO, ANNA. Opportunity-specific entrepreneurial intentions in sustainable entrepreneurship. 2018. Diss.

787. PULKKINEN, AKI. Towards a better understanding of activity and selectivity trends involving K and O adsorption on selected metal surfaces. 2017. Diss.

788. ZHAO, WENLONG. Reliability based research on design, analysis and control of the remote handling maintenance system for fusion reactor. 2018. Diss.

789. IAKOVLEVA, EVGENIA. Novel sorbents from low-cost materials for water treatment. 2018. Diss.

790. KEDZIORA, DAMIAN. Service offshoring industry: systems engineering approach to its transitional challenges. 2018. Diss.

791. WU, JING. Soft computing methods for performance improvement of EAMA robot in fusion reactor application. 2018. Diss.

792. VOSTATEK, PAVEL. Blood vessel segmentation in the analysis of retinal and diaphragm images. 2018. Diss.

793. AJO, PETRI. Hydroxyl radical behavior in water treatment with gas-phase pulsed corona discharge. 2018. Diss.

794. BANAEIANJAHROMI, NEGIN. On the role of enterprise architecture in enterprise integration. 2018. Diss.

795. HASHEELA-MUFETI, VICTORIA TULIVAYE. Empirical studies on the adoption and implementation of ERP in SMEs in developing countries. 2018. Diss.

796. JANHUNEN, SARI. Determinants of the local acceptability of wind power in Finland. 2018. Diss.

797. TEPLOV, ROMAN. A holistic approach to measuring open innovation: contribution to theory development. 2018. Diss.

798. ALBATS, EKATERINA. Facilitating university-industry collaboration with a multi-level stakeholder perspective. 2018. Diss.

799. TURA, NINA. Value creation for sustainability-oriented innovations: challenges and supporting methods. 2018. Diss.

800. TALIKKA, MARJA. Recognizing required changes to higher education engineering programs' information literacy education as a consequence of research problems becoming more complex. 2018. Diss.

**801.** MATTSSON, ALEKSI. Design of customer-end converter systems for low voltage DC distribution from a life cycle cost perspective. 2018. Diss.

**802.** JÄRVI, HENNA. Customer engagement, a friend or a foe? Investigating the relationship between customer engagement and value co-destruction. 2018. Diss.

**803.** DABROWSKA, JUSTYNA. Organizing for open innovation: adding the human element. 2018. Diss.

**804.** TIAINEN, JONNA. Losses in low-Reynolds-number centrifugal compressors. 2018. Diss.

**805.** GYASI, EMMANUEL AFRANE. On adaptive intelligent welding: Technique feasibility in weld quality assurance for advanced steels. 2018. Diss.

**806.** PROSKURINA, SVETLANA. International trade in biomass for energy production: The local and global context. 2018. Diss.

**807.** DABIRI, MOHAMMAD. The low-cycle fatigue of S960 MC direct-quenched high-strength steel. 2018. Diss.

**808.** KOSKELA, VIRPI. Tapping experiences of presence to connect people and organizational creativity. 2018. Diss.

**809.** HERALA, ANTTI. Benefits from Open Data: barriers to supply and demand of Open Data in private organizations. 2018. Diss.

**810.** KÄYHKÖ, JORMA. Erityisen tuen toimintaprosessien nykytila ja kehittäminen suomalaisessa oppisopimuskoulutuksessa. 2018. Diss.

**811.** HAJIKHANI, ARASH. Understanding and leveraging the social network services in innovation ecosystems. 2018. Diss.

**812.** SKRIKO, TUOMAS. Dependence of manufacturing parameters on the performance quality of welded joints made of direct quenched ultra-high-strength steel. 2018. Diss.

**813.** KARTTUNEN, ELINA. Management of technological resource dependencies in interorganizational networks. 2018. Diss.

**814.** CHILD, MICHAEL. Transition towards long-term sustainability of the Finnish energy system. 2018. Diss.

**815.** NUTAKOR, CHARLES. An experimental and theoretical investigation of power losses in planetary gearboxes. 2018. Diss.

**816.** KONSTI-LAAKSO, SUVI. Co-creation, brokering and innovation networks: A model for innovating with users. 2018. Diss.

**817.** HURSKAINEN, VESA-VILLE. Dynamic analysis of flexible multibody systems using finite elements based on the absolute nodal coordinate formulation. 2018. Diss.

**818.** VASILYEV, FEDOR. Model-based design and optimisation of hydrometallurgical liquid-liquid extraction processes. 2018. Diss.

**819.** DEMESA, ABAYNEH. Towards sustainable production of value-added chemicals and materials from lignocellulosic biomass: carboxylic acids and cellulose nanocrystals. 2018. Diss.

Acta Universitatis
Lappeenrantaensis
820